Technical Physics Letters, Vol. 30, No. 8, 2004, pp. 619–621. Translated from Pis'ma v Zhurnal Tekhnicheskoĭ Fiziki, Vol. 30, No. 15, 2004, pp. 1–7.

Mechanically Tuned Relativistic Backward Wave Oscillator

S. A. Kitsanov, S. D. Korovin, A. I. Klimov, V. V. Rostov, and E. M. Tot'meninov*

Institute of High-Current Electronics, Siberian Division, Russian Academy of Sciences, Tomsk, Russia

** e-mail: totm@lfe.hcei.tsc.ru*

Received January 26, 2004

Abstract—A high-power relativistic microwave oscillator with low magnetic field is created based on a backward wave oscillator (BWO) with resonance reflector. For fixed parameters of the slow-wave structure (SWS) and the electron beam, the oscillation frequency of this BWO can be mechanically tuned within a 12% band by moving the resonance reflector relative to the SWS. A maximum output pulse radiation power of 4 ± 1 GW at a working frequency of 3.6 GHz is achieved with a magnetic field of 4.6 kOe. *© 2004 MAIK "Nauka/Interperiodica".*

In recent years, much attention has been devoted to the creation and development of high-power relativistic microwave oscillators with the working frequency controlled within a broad range. One of the most effective coherent radiation sources of this type is the backward wave oscillator (BWO), which is characterized by a short transient time and good adaptation to variable electron beam parameters. Unfortunately, for electron beam energies in the relativistic range, the frequency of normal BWOs can be tuned within a rather narrow band of 3–4% [1] mostly by displacing a below-cutoff waveguide section relative to the slow-wave structure (SWS). The next step in this direction, which allowed the working frequency to be mechanically tuned within 15% on a half-maximum power level, was provided by changing the SWS period while simultaneously adjusting the below-cutoff waveguide section [2]. In these BWO variants, high output powers and efficiencies were achieved for magnetic fields above the cyclotron resonance level. The effect of magnetic field on the Cherenkov radiation synchronism was insignificant.

This study was devoted to an alternative approach, whereby mechanical tuning of the BWO frequency is achieved by using preliminary high-frequency modulation of the electron velocity with controlled high-frequency current phase relative to that of the synchronous wave at the SWS input (modulation phase) rather than by changing the SWS geometry. In this scheme, reflection of the backward wave from a broadband resonance reflector (a lumped inhomogeneity) is achieved through excitation of a closed symmetric mode with the radial index increased by unity. Previous analysis [3] of the starting conditions showed that the modulation phase, which can be controlled by reflector displacements, significantly influences the normalized starting length and synchronism detuning. It is important to note that dependence of the synchronism detuning on the modulation phase is generally retained in the nonlinear regime. An obvious result suggested by the boundary-value problem solution is that the range of variation of this detuning (and, hence, of the frequency) expands with increasing amplitude of the electron velocity modulation in the region of the resonance reflector. In order to avoid a decrease in the BWO efficiency, it is necessary to consistently modify the SWS parameters (i.e., reduce the system length).

Previously [4], it was demonstrated that the use of an electrodynamic system with increased transverse dimensions and the selective properties retained by means of preliminary modulation not only decreases the probability of high-frequency breakdown at a high power of the pulsed electromagnetic radiation but also creates prerequisites for retaining the regime of high-efficiency generation in magnetic fields below the cyclotron resonance level. In fact, the power consumed for the creation of magnetic field in a BWO operating in a periodic pulsed regime was decreased by a factor of more than 10 at an oscillator efficiency of about 20%. In these investigations, it is necessary to take into account and compensate for the effect of magnetic field on both the efficiency and frequency of the oscillator.

In this context, our study was aimed at evaluation of the possibility of mechanically tuning the frequency by more than 10% for a multigigawatt BWO operating in the 8-cm range by displacing the whole SWS relative to the resonance reflector.

The BWO geometry was optimized using the fully electromagnetic numerical PIC-code KARAT [5]. In this geometry (Fig. 1), the mean corrugation diameter is approximately 1.5 times the radiation wavelength for the working E_{01} mode. Optimum electron beam characteristics determined from these calculations corresponded to a cathode voltage of about 1.2 MV and a beam current of about 12.5 kA. Variation of the magnetic field showed that the interval of stable generation was rather narrow: from ≈2.5 to ≈4.5 kOe. The lower

1063-7850/04/3008-0619$26.00 © 2004 MAIK "Nauka/Interperiodica"

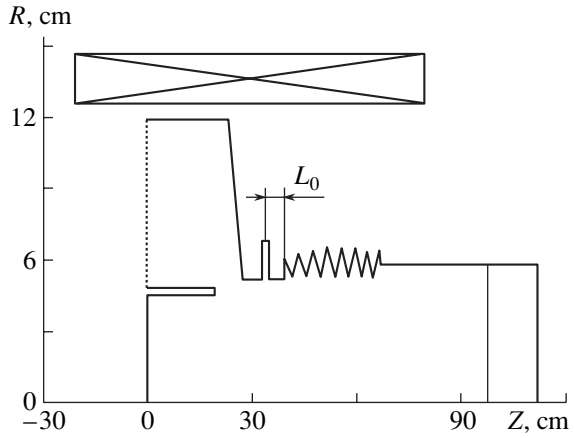

Fig. 1. Schematic diagram of a relativistic BWO with resonance reflector.

limit is related to the growth of transverse electron velocities in the beam formed in the diode, while the upper limit is determined by cyclotron absorption of the backward wave. The results of calculations performed for various positions of the resonance reflector relative to the SWS showed that displacement of the reflector (i.e., a change in L_0) is accompanied by a shift of the oscillation frequency within ≈100 MHz/cm (Fig. 2).

It should be noted that the maximum tuning bandwidth on a half-maximum power level, $F_{max}/F_{min} - 1 \approx 14\%$ (3.48–3.95 GHz), was obtained provided a certain correction of the BWO regime with respect to the magnetic field. This is probably related to a change in the conditions of cyclotron absorption of the backward wave depending on the oscillation frequency. The maximum calculated oscillation power (≈4.5 GW) corresponds to an efficiency of ≈32%. In the course of numerical modeling, it was found that the transient process duration increases on approaching regimes corresponding to the boundaries of the effective tuning band. This can be explained by growth of the oscillator start current at a fixed electron beam current.

The experiments were performed with a periodic pulsed nanosecond electron accelerator of the Sinus-7 type, which generated a single pulsed electron beam with a duration of 50 ns at a cathode voltage of ≈1.2 MV and diode current of about 16 kA. The amplitude of the electron beam current in the electrodynamic system of the oscillator increased with the magnetic field and stabilized at a level of ≈13 kA for $H \approx 4$ kOe. In this case, the beam did not touch internal surfaces of the left and right waveguides contacting with the resonant reflector. The significant difference (≈3 kA) between the aforementioned currents was probably related to leaks in the vacuum diode.

The output microwave radiation power was determined using a calibrated nondirectional waveguide-strip coupler, a short symmetric dipole antenna, and an aperture calorimeter. The radiation spectrum was measured using a heterodyne technique, whereby the intermediate-frequency signal was processed by a TDS-644 oscillograph equipped with a fast-Fourier-transform (FFT) converter. Figure 3 shows the typical signal measured at the output of the waveguide-strip coupler and the heterodyne frequency meter for a particular position

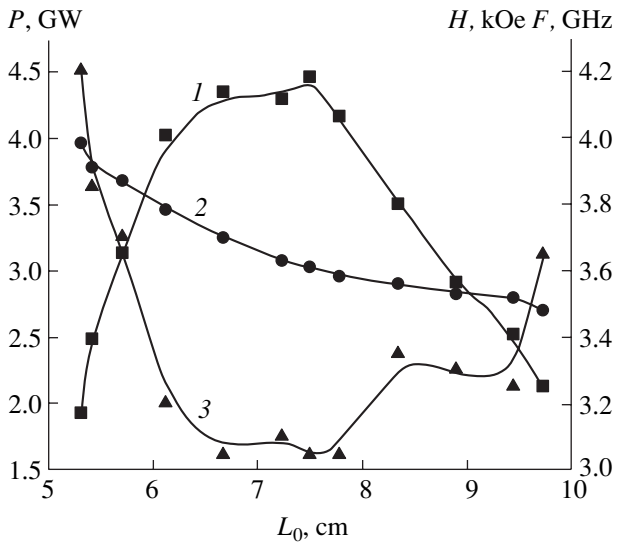

Fig. 2. Experimental plots of the (*1*) output radiation power *P* (*2*) oscillation frequency *F*, and (*3*) focusing magnetic field strength *H* versus drift length L_0.

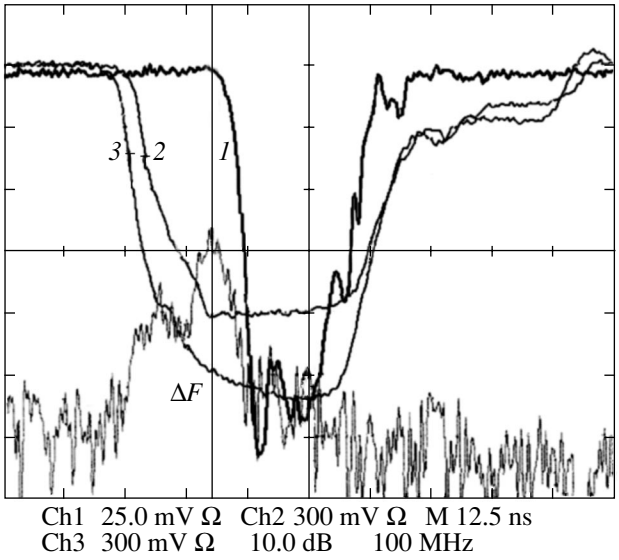

Fig. 3. Typical oscillograms of the (*1*) BWO output signal, (*2*) cathode voltage, and (*3*) diode current and (Δ*E*) FFT of the heterodyne signal. Oscillation frequency, $F_1 = F_2 - \Delta F$; heterodyne frequency, $F_2 = 3.9$ GHz; $\Delta F \approx 3.4$ GHz; diode current, ≈16 kA; cathode voltage, ≈1.2 MV; magnetic field, $H \approx 4.6$ kOe.

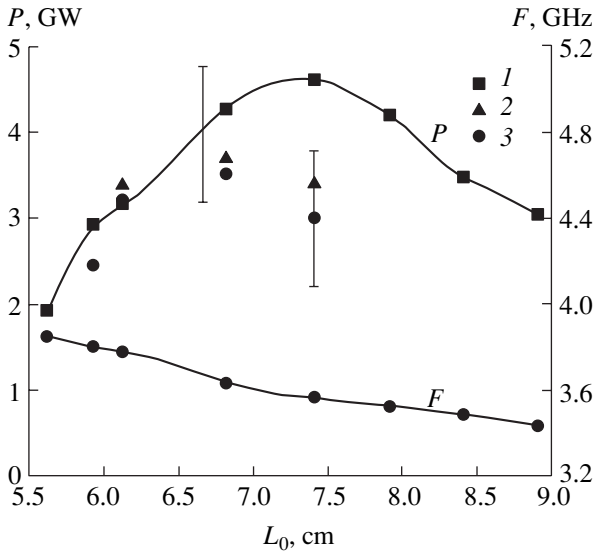

Fig. 4. Plots of the peak output radiation power P and oscillation frequency F versus resonance reflector position L_0. The peak power was measured using (*1*) a waveguide strip coupler, (*2*) an aperture calorimeter (not taking into account the reflected and scattered microwave power), and (*3*) a short symmetric dipole.

(L_0 = 7.4 cm) of the resonance reflector. A certain structure in the microwave signal is probably related to reflection of a part of the microwave power from the output window of the radiating horn. At each fixed position of the resonance reflector, the output radiation power and frequency depended on the magnetic field. For this reason, the optimum magnetic field was selected for each L_0. Based on the obtained experimental data, it is possible to realize a variant of the relativistic BWO frequency tuning depicted in Fig. 4. Within the indicated band, the magnetic field varied from 4.1 to 4.9 kOe.

It should be noted that there is certain instability in the microwave pulse amplitude, duration, and frequency near the boundaries of the tuning band. This instability can be related to a certain competition of parasitic oscillations (in our experiments, parasitic oscillations were generated at 3.2 and 4.5 GHz) and insufficient length of the accelerator voltage pulse.

Conclusions. We have realized mechanical tuning of the oscillation frequency of a relativistic BWO by means of displacement of a resonance reflector with respect to the SWS at fixed corrugation parameters and electron beam characteristics. In experiments with the optimum position of the resonance reflector, the peak output radiation power in the single mode regime was 4 ± 1 GW at an efficiency of ≈25%. The bandwidth of mechanical tuning on a half-maximum power level was 12% (3.44–3.85 GHz).

REFERENCES

1. S. D. Korovin, S. D. Polevin, A. M. Roĭtman, *et al.*, Izv. Vyssh. Uchebn. Zaved. Fiz. **39** (12), 49 (1996).
2. S. A. Kitsanov, A. I. Klimov, S. D. Korovin, *et al.*, Pis'ma Zh. Tekh. Fiz. **29** (6), 87 (2003) [Tech. Phys. Lett. **29**, 259 (2003)].
3. S. D. Korovin, I. K. Kurkan, V. V. Rostov, *et al.*, Izv. Vyssh. Uchebn. Zaved. Radiofiz. **42**, 1189 (1999).
4. I. K. Kurkan, V. V. Rostov, and E. M. Tot'meninov, Pis'ma Zh. Tekh. Fiz. **24** (10), 43 (1998) [Tech. Phys. Lett. **24**, 388 (1998)].
5. V. P. Tarakanov, *User's Manual for Code Karat* (Berkley, Springfield, 1992).

Translated by P. Pozdeev

Technical Physics Letters, Vol. 30, No. 8, 2004, pp. 622–625. Translated from Pis'ma v Zhurnal Tekhnicheskoĭ Fiziki, Vol. 30, No. 15, 2004, pp. 8–14.

Recognition of the Interference Spiral Image in a Fiber Optical Sensor Employing Optical Vortices

T. A. Fadeeva, A. V. Volyar, and A. N. Alekseev

Taurida National University, Simferopol, Ukraine

Received December 22, 2003

Abstract—Three methods of processing the image of an interference spiral formed in a fiber optical sensor employing optical vortices have been considered. It is established that a method based on recognition of the spiral image is most stable with respect to noises. Using this technique, it is possible to determine the angle of spiral rotation even when the visibility of the interference pattern decreases to 0.2. The passage from intensity measurements to determination of the geometric parameters of the image significantly increases the range of linearity of interferometric devices employing optical vortices. *© 2004 MAIK "Nauka/Interperiodica".*

Fiber optical interference sensors of most known types are characterized by nonlinear relations between the phase difference and the interference band intensity [1]. However, the linear region of the sensor characteristic can be significantly expanded [2] in a scheme employing the properties of optical vortices [3]. Such situations are encountered, for example, in fiber optical couplers selectively transmitting optical vortices and the fundamental HE_{11} mode via different channels [4]. When the two beams are added at the coupler output, a pattern of interference spiral is formed with the angle of rotation linearly depending on the phase difference between the two beams. Using this property of optical vortices, it is possible to provide linear measurements in the entire range of rotation angles. A key problem in these measurements is recognition of the spiral image on a noisy background.

This study was aimed at developing a method for determining the parameters of the interference spiral formed in fiber optical sensors employing optical vortices for the measurement of physical quantities.

The distribution of intensity in the interference pattern is described by the standard relation [5]

$$I = I_1 + I_2 + 2\sqrt{I_1 I_2}\cos(\Phi_1 - \Phi_2), \qquad (1)$$

where I_1 and I_2 are the intensities of the Gaussian beam and the optical vortex;

$$\Phi_1 = kz + \arctan\left(\frac{z}{z_{0g}}\right) + \frac{kr^2}{R_g(z)} + \phi_{0g},$$

$$\Phi_2 = kz + (l+1)\arctan\left(\frac{z}{z_{0v}}\right) + \frac{kr^2}{R_v(z)} + \phi_{0v} - l\varphi,$$

are the phases of these beams; r and φ are the polar coordinates in the screen plane; z is the distance to the screen; $R(z) = z[1 + (z_0^2/z^2)]$ is the curvature radius; $z_0 = \frac{k\rho^2}{2}$ is the Rayleigh length; ρ is the waist radius; ϕ_0 is the initial phase of the beam; and the subscripts "g" and "v" refer to the Gaussian beam and the optical vortex, respectively. In the case of coaxial propagation of the two beams, a pattern of interference spiral is formed on the screen, where the bright and dark bands correspond to the phase differences $\Phi_1 - \Phi_2 = 2m\pi$ and $(2m+1)\pi$ ($m = 1, 2, \ldots$), respectively. Let us express the phase difference in the screen plane z = const as

$$\Delta F = \Phi_1 - \Phi_2 = -ar^2 + b' + l\varphi, \qquad (2)$$

where

$$a = k\left(\frac{1}{R_v(z)} - \frac{1}{R_g(z)}\right),$$

$$b' = \arctan(z/z_{0g}) - (l+1)\arctan(z/z_{0v}) + \phi_0.$$

Then, the equation describing the interference spiral can be written as

$$\varphi = ar^2 + b_0, \qquad (3)$$

where $b_0 = \Delta\Phi - b'$ for a vortex with the topological charge $l = 1$.

The angle of rotation of the spiral pattern is characterized by the parameter b_0, which is directly related to the phase difference $\Delta\Phi$. However, it is impossible to determine b_0 in the interference pattern independently of the other parameters, including the coordinates of the center of this pattern and the spiral twist parameter a. Prior to analysis of the methods of measurement of the b_0 value, let us consider one method of determination of the center of the interference pattern.

1063-7850/04/3008-0622$26.00 © 2004 MAIK "Nauka/Interperiodica"

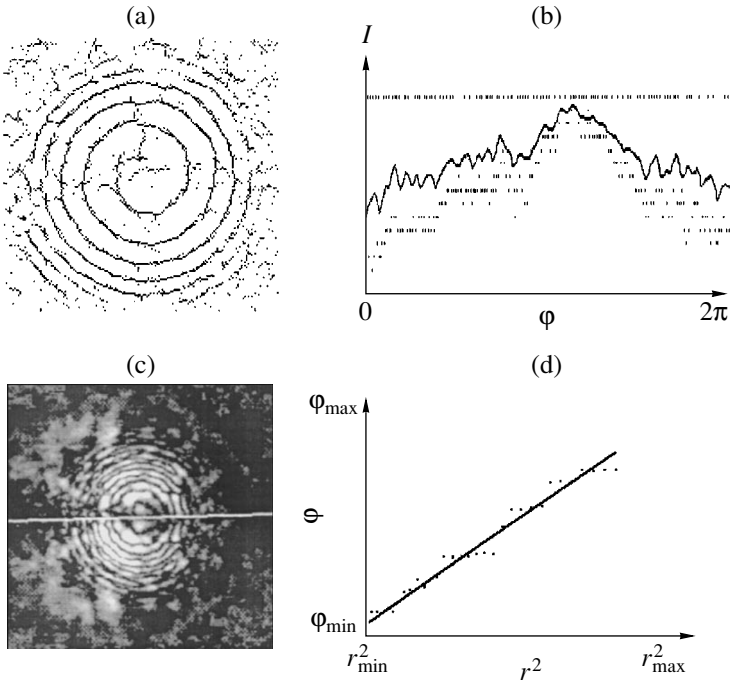

Fig. 1. Processing of the spiral interference image: (a) intensity distribution; (b) the intensity I versus azimuthal angle φ along a circle within the detection ring; (c) the pattern of moire fringes; (d) the azimuthal angle φ of the intensity minimum versus square radius of a circle within the detection ring.

It can be shown that the center of mass of a homogeneous spiral described by Eq. (3) is displaced relative to the origin. However, for two spirals corresponding to states of a singular beam with opposite phases, the center of mass of such a double spiral coincides with the center of the interference pattern. This simple principle underlies the method used for determining the origin of coordinates of the spiral image.

The positions of the intensity maxima and minima in the interference pattern were determined by scanning along the x and y coordinates. Using the ratio of the sum of like coordinates to the number of measurements, the position of the center of mass is determined as

$$X_c = \frac{\sum_{i=1}^{N} x_i}{N}, \quad Y_c = \frac{\sum_{i=1}^{N} y_i}{N}. \qquad (4)$$

However, this approach is difficult to use in experiment because a real pattern contains a large number of additional noisy maxima and minima not coinciding with the spiral (Fig. 1a). In order to eliminate the influence of this noise, we employed filtration of the image elements and smoothening of the image. Computer-aided filtration eliminates all points of the image occurring outside a certain average interval of intensities ($\bar{I}_{\min}$, $\bar{I}_{\max}$). Once the intensity measured at a given point is below a preset minimum, $I < \bar{I}_{\min}$, the intensity at this point on the image is set equal to zero ($I = 0$). If the intensity exceeds a preset maximum, $I > \bar{I}_{\max}$, the image intensity is set equal to this average maximum value ($I = \bar{I}_{\max}$). After this discrimination, the image is smoothened by averaging over neighboring points and the center of the spiral pattern is calculated by formulas (4) using the procedure described above.

We have developed two methods of determining the rotation parameter b_0 without determination of the twist parameter a. The first method is based on finding the minimum (or maximum) intensity on a circle occurring inside the detection ring and centered at the center of the spiral pattern (Fig. 1b). The inner and outer radii of the ring ($r_{\min}$, $r_{\max}$) are selected so as to provide that the average intensity within this ring would not be lower than one-third of the average maximum intensity of the image. The circle radius was kept constant during the measurement. However, this method leads to a rather large uncertainty because of intensity fluctuations and errors of determination of the image center.

The second method is based on the formation of moire fringes as a result of superposition of the initial and mirror images of the spiral with respect to the y axis (Fig. 1c). A theoretical value of the angle of rotation of this pattern is determined using the following considerations. For the mirror image of the initial pattern, only the angle φ is changed to the opposite (–φ) in expression (2). This corresponds to sign reversal of the topological charge of the optical vortex and to alteration of the spiral twist direction. The result of subtrac-

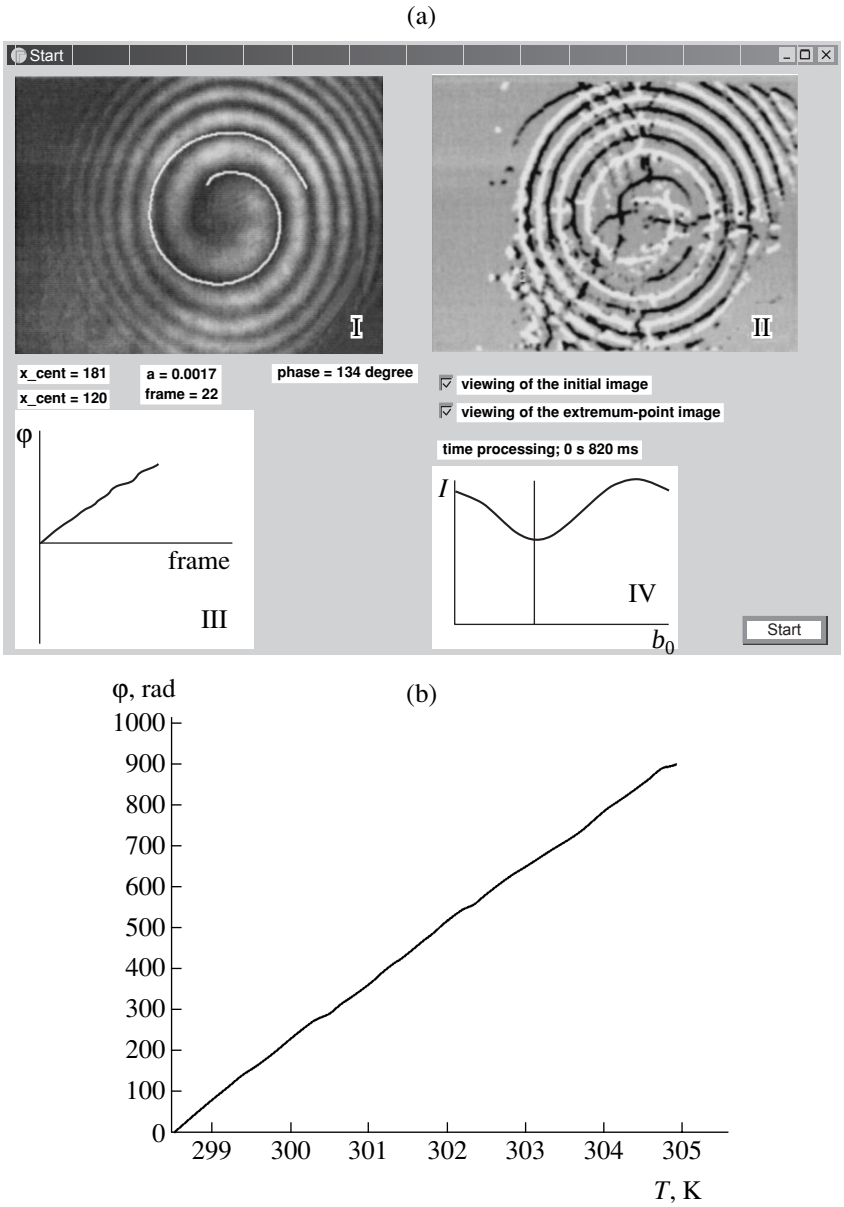

Fig. 2. (a) Processing of the spiral interference image: (I) recognition of the spiral interference pattern with indicated parameters; (II) distribution of minima (black points) and maxima (bright points) in the interference pattern; (III) spiral rotation angle φ versus frame number (proportional to the sample temperature); (IV) integral intensity versus parameter b_0. (b) Experimental dependence of the spiral rotation angle on the temperature for a fiber optical sensor employing optical vortices.

tion of the images of these spirals is analytically described by the relation

$$I = 4\sqrt{I_1 I_2}\sin\left\{\frac{ar^2 + b_0}{2}\right\}\sin\left\{\varphi - \frac{b_0}{2}\right\}. \qquad (5)$$

This formula shows that the angle of rotation of the edge dislocation axis (zero intensity line) is $b_0/2$. To determine the angle of rotation of the edge dislocation axis, we plotted the integral intensity versus azimuthal coordinate (the sum was taken along the line φ = const for r varying from $-r_{max}$ to r_{max}). After smoothening of this curve, its minimum coincided with the position of the edge dislocation. This method is highly sensitive to the error of determination of the image center. Even small displacement of the centers of subtracted images significantly changes the appearance of the edge dislocation.

Then, we developed the third method of determining the spiral rotation angle, which is referred to as recognition of the spiral image. This method, based on finding a minimum (or maximum) of the integral intensity (3) as a function of the parameter b_0, significantly decreases the noise level of the image [6]. To determine

the parameter a, we also set a circle inside the detection ring (like that used in the first method described above), but the radius r of this circle is varied within (r_{min}, r_{max}). This variation is accompanied by measurement of the angular coordinate φ as a function of r^2. The resulting curve is approximated by the straight line $\varphi(r^2)$, whose slope gives the a value (Fig. 1d). Using this approach, it is possible to recognize the image of the spiral and determine the necessary geometric parameters of this image.

In experiment, we measured the dependence of the spiral rotation angle on the temperature using a scheme of the Y-shaped fiber optical coupler [4] with the fundamental HE_{11} mode propagating in the sample arm and an optical vortex propagating in the reference arm. For a small change in the temperature (within a few tens of degrees), the temperature dependence of the phase of the HE_{11} mode can be approximated by a straight line [7]. The interference pattern was recorded using a CCD camera and the image was processed on a computer. Heating the sample arm in a water-filled thermostat led to rotation of the interference spiral. These data were processed by a special routine (written in Delphi language) using the third method of determination of the spiral rotation angle (Fig. 2a). The temperature increment on the passage from frame to frame was $\Delta T \sim 4 \times 10^{-4}$ K.

Figure 2b shows the temperature dependence of the rotation angle measured in the interval from 298.5 to 305 K. The average error of these measurements was 0.012 rad and the responsivity of such a temperature sensor with a coupler made of SMS 28 fiber (Korning Inc.) was 198 rad/(m K).

Thus, using optical vortex in one arm of an interference fiber optical sensor, it is possible to reduce the measurement of physical quantities to determination of the geometric parameters of the image of the spiral interference pattern, thus significantly expanding the range of linearity of the interferometric device.

Acknowledgments. The authors are grateful to M.S. Soskin for fruitful discussions.

This study was supported by the Ukrainian Scientific-Technological Center, project no. R-051.

REFERENCES

1. V. I. Busurin, A. S. Semenov, and N. P. Udalov, Kvantovaya Élektron. (Moscow) **12**, 901 (1985).
2. T. A. Fadeyeva, A. V. Volyar, S. A. Reshetnikoff, and A. N. Alexeyev, Proc. SPIE **4403**, 306 (2001).
3. M. S. Soskin and N. V. Vasnetsov, Prog. Opt. **42**, 219 (2001).
4. T. A. Fadeeva and A. V. Volyar, Pis'ma Zh. Tekh. Fiz. **29** (14), 50 (2003) [Tech. Phys. Lett. **29**, 594 (2003)].
5. M. Born and E. Wolf, *Principles of Optics* (Pergamon, Oxford, 1969; Nauka, Moscow, 1970).
6. T. Fadeyeva, D. Kurabtzev, A. Volyar, and M. Soskin, Proc. SPIE **4607**, 83 (2002).
7. J. D. C. Jones and D. A. Jackson, Anal. Proc. **22**, 207 (1985).

Translated by P. Pozdeev

Technical Physics Letters, Vol. 30, No. 8, 2004, pp. 626–627. Translated from Pis'ma v Zhurnal Tekhnicheskoĭ Fiziki, Vol. 30, No. 15, 2004, pp. 15–18.

Mass Spectrometry of Chlorine Monolayers on Solid Substrates

V. D. Frolov, L. A. Apresyan, D. V. Vlasov, G. A. Krikunov, and T. V. Vlasova

Natural Sciences Center, Prokhorov Institute of General Physics, Russian Academy of Sciences, Moscow, 117924 Russia

e-mail: lesa@nsc.gpi.ru

Received February 3, 2004

Abstract—A new method is proposed for determining chlorine traces in monolayer films adsorbed on solid substrates. The method is based on secondary-ion mass spectrometry (SIMS) with the formation of positive chlorine-containing molecular ions. In contrast to the traditional method making use of inert gases, the secondary ions are generated by bombarding the chlorine-containing substrate with a beam of methane molecules. This leads to the formation of CCl_2^+ ions with molecular masses of 82, 84, and 85 amu. These peaks are reliably observed in the form of a doublet not masked by the peaks of ions of the substrate material and the other background reaction products. *© 2004 MAIK "Nauka/Interperiodica".*

As is known, it is very difficult to use secondary-ion mass spectrometry (SIMS) for detecting trace amounts of halogens and other elements susceptible to accepting electrons with the formation of negative atomic and molecular ions [1–4]. This difficulty is also encountered when using SIMS for detecting organochlorine compounds on silicon substrates [5].

Below, we describe the results of experiments devoted to the mass-spectrometric detection of trace amounts of chlorine. The SIMS measurements were performed on a modified LKB 2091A mass spectrometer, in which the standard oil diffusion pump was replaced by a turbomolecular pump in order to provide for an oilless vacuum in the working chamber. In addition, the mass spectrometer was linked to a computer of the IBM PC type for data acquisition and processing.

In the conventional SIMS configuration (see, e.g., [1]), a solid target is probed by a beam of inert gas (mostly argon) ions. In the first stage of our investigation, we used a standard plasma ionization source (Ion Technology Inc.) for mass spectrometers, which ensured bombardment of a solid target (substrate) with a 10-keV ion beam with a 1-mm beam spot diameter on the target surface. The sensitivity of the mass spectrometer with respect to chlorine was evaluated by comparing the spectra obtained from commercial single crystal silicon (with a chlorine impurity content on the level of requirements adopted in the electronic technology) to the spectra of samples intentionally treated with hydrochloric acid. The surface of the latter samples contained microscopic impurities of metals and trace amounts of chlorine (typically, at a relative content below 1% in the form of chlorine-containing salts).

Figure 1 shows the mass spectrum of a sample treated with hydrochloric acid. The spectrum displays intense peaks due to silicon isotopes (%): ^{28}Si, 92.18; ^{29}Si, 4.71; and ^{30}Si, 3.12. The presence of trace impurities is reflected by a small peak observed in the region of 23 amu (Na). It should be noted that the spectra of some of the initial samples showed the presence of traces of other metals, in particular, calcium. However, no evidence of chlorine was observed upon the treatment with hydrochloric acid (see Fig. 1), although it was evident that chlorine in such samples was present with high probability.

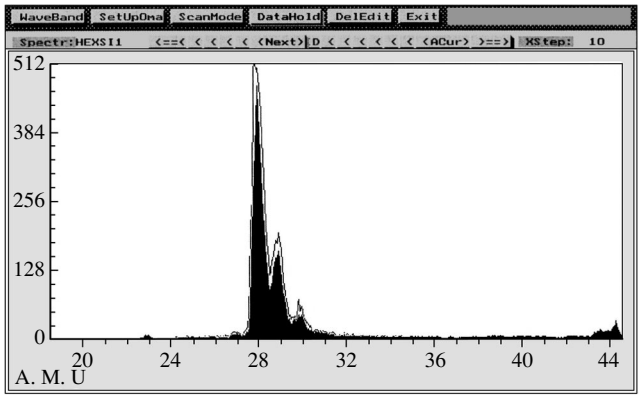

Fig. 1. Conventional SIMS spectrum of a silicon sample treated with hydrochloric acid, showing resolved peaks of silicon isotopes (three sequential records were performed in order to check for reproducibility).

1063-7850/04/3008-0626$26.00 © 2004 MAIK "Nauka/Interperiodica"

In order to reliably check for the possibility of detecting chlorine, we used a target in the form of a NaCl crystal plate, where chlorine accounts exactly for half of the total number of atoms. The chlorine-free reference sample was a high-purity silicon wafer. The spectrum of the NaCl target probed by an atomic beam of argon exhibited clear peaks of ^{23}Na and traces of molecular nitrogen (28 amu), but the signals of chlorine (35 and 37 amu) atoms or related molecules were completely absent. Irradiation with the beams of hydrogen, neon, argon, krypton, and xenon ions led to the appearance of only very weak (detected on a noise level) signals corresponding to the molecular ions of Cl_2^+ at 70 (2×35) and 72 (35 + 37) amu; the peak at 74 amu was virtually indistinguishable on the noise background.

Thus, attempts to directly detect chlorine using standard gases for the probing of samples with known contents of this element gave spectra with completely absent atomic peaks at 35 (75%) and 37 (25%) amu and the corresponding molecular peaks (70, 72, and 74 amu). Our experiments showed that the absence of chlorine ions and molecular radicals is related to the extremely low cross sections for the formation of positive ions from chlorine atoms and molecules. This behavior is in sharp contrast with that of silicon: the peaks corresponding to Si are clearly observed even with maximum attenuation and minimum slit widths (which corresponds to signal attenuation by a factor on the order of 10^8).

In order to reach a higher sensitivity with respect to chlorine and provide for a highly effective production of positive ions containing chlorine, we used for the first time methane as the probing gas. In contrast to the case of inert gases, the obtained mass spectrum exhibited two intense peaks corresponding to CCl^+ ions. The spectrum measured by SIMS using methane is presented in Fig. 2 and interpreted in the legend to this figure.

The results of our experiments show that the proposed new method using SIMS ensures the detection of trace amounts of chlorine with high sensitivity on the surface of solid substrates.

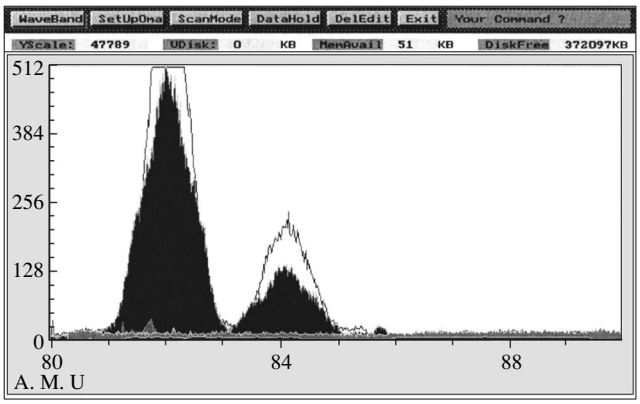

Fig. 2. Mass spectra of samples probed by methane atoms: shaded peaks correspond to a sample with trace amounts of chlorine on the surface of silicon treated with hydrochloric acid (intense peak at 82 amu); solid line shows the peaks of CCl_2^+ from a NaCl crystal; bright spectrum on the shaded background shows the conventional SIMS spectrum of NaCl probed by argon ions.

Acknowledgments. This study was supported by the Russian Foundation for Basic Research, project no. 02-02-16725.

REFERENCES

1. A. A. Sysoev, V. B. Artaev, and V. V. Kashcheev, *Isotope Mass Spectroscopy*, Ed. by A. A. Sysoev (Énergoatomizdat, Moscow, 1993).
2. S. Ferrari, G. Scarel, C. Wiemer, and M. Fanciulli, J. Appl. Phys. **92**, 7675 (2002).
3. A. Godon, J. Webster, G. Layne, *et al.*, Geophys. Res. Abstr. Eur. Geophys. Soc. **5**, 13080 (2003).
4. G. C. Allen, I. T. Brown, E. Ciliberto, *et al.*, Eur. J. Mass. Spectrom. **1**, 493 (1995).
5. V. D. Frolov, V. I. Konov, S. M. Pimenov, *et al.*, Appl. Phys. A **78**, 21 (2004).

Translated by P. Pozdeev

Technical Physics Letters, Vol. 30, No. 8, 2004, pp. 628–630. Translated from Pis'ma v Zhurnal Tekhnicheskoĭ Fiziki, Vol. 30, No. 15, 2004, pp. 19–24.

Electrochemical Synthesis of Thin CdS Films

G. A. Il'chuk*, V. O. Ukrainets, Yu. V. Rud', O. I. Kuntyi, N. A. Ukrainets, B. A. Lukiyanets, and R. Yu. Petrus

"Lvivska Politekhnika" National University, Lviv, Ukraine

Ioffe Physicotechnical Institute, Russian Academy of Sciences, St. Petersburg, 194021 Russia

** e-mail: gilchuk@polynet.lviv.ua*

Received January 15, 2004

Abstract—Thin cadmium sulfide (CdS) films have been electrochemically synthesized on metal substrates and the related photosensitive surface barrier structures have been obtained. The proposed method can be used in the technology of thin-film photoelectric converters with large areas. © *2004 MAIK "Nauka/Interperiodica".*

The synthesis of high-quality films of various semiconductor materials—in particular, cadmium sulfide (CdS) and telluride (CdTe)—and the technology of heterojunctions based on such films are among the main problems in semiconductor electronics and solar energetics [1, 2]. The research and development in this field employs various technological approaches based on vapor phase deposition, electrodeposition on nanoporous substrates, chemical synthesis, etc. [2–5].

We have studied the possibility of obtaining thin CdS films on metal substrates by the electrochemical method. Below, we present the first results and report on the properties of obtained films and related surface barrier structures.

The electrochemical synthesis of semiconductor films is most promising in solving the problem of obtaining large-area solar energy converters. Another advantage is that the synthesis is conducted at room temperature, which decreases deviations from stoichiometry. In addition, this method is economically profitable.

Surface barrier structures provide fast and convenient solution of the complex problem involving (i) obtaining physical information, (ii) identification of electrochemically synthesized semiconductor films, and (iii) verification of the possibility of obtaining effective photoelectric converters. For standardization of the conditions of synthesis, CdS films were electrochemically deposited onto the surface of cylindrical electrodes with a diameter of $d = 5$ mm made of metallic cadmium and flash pressed into fluoroplastic sleeves. Prior to the exposure in electrolyte, the edge surfaces of cylindrical cadmium electrodes were pretreated by two methods: (a) mechanical grinding with an abrasive powder of the ASM-0.7 grade (A-type samples) and (b) the same mechanical grinding followed by etching in a brominated methanol solution for removal of the damaged surface layer (B-type samples).

Sulfide films were deposited using a 1 M aqueous Na_2S solution as the electrolyte. The electrochemical process was conducted for ~30–60 min in a potentiostatic regime at a voltage of $\varphi = 1$ V and a temperature of $T = 303$–323 K. The experiments were performed using a PI-50-1.1 potentiostat and a standard temperature-controlled electrochemical cell with cadmium auxiliary electrode and silver chloride reference electrode. After electrolysis, the samples were rinsed sequentially with distilled water and ethanol and dried in air. The edge surface of preliminarily etched cadmium electrodes of the B-type surface exhibited visible block structure with homogeneous regions of various orientations having dimensions on the order of 4–6 mm. An analogous structure was observed upon deposition of a sulfide film.

As a result of the electrochemical process, cadmium electrodes were coated with a film of yellow color characteristic of CdS. In samples of the A type, the coating was visibly highly homogeneous over the area and had a uniform thickness. The samples of the B type exhibited a pronounced block structure, while the coating quality within each block was higher than that in samples of the A type.

The composition of the electrochemical deposit was determined by electrooptical method using surface barrier structures (Schottky barriers) obtained by covering the upper surface of a sulfide film with a thin (~0.1 mm thick) layer of silver or indium. The pure silver and indium layers were obtained by thermal deposition in vacuum ($\cong 10^{-4}$ Torr) onto the surface of as-deposited sulfide films without any pretreatment. The barrier contact area was approximately 2×2 mm^2.

The dark current–voltage characteristics (*I–V* curves) of Ag(In)/CdS/Cd structures of the A type showed the absence of rectification. The *I–V* curves of such structures were linear and their resistances at $T = 300$ K varied within broad limits ($R = 1$–1×10^3 Ω). In contrast,

Ag/CdS/Cd and In/CdS/Cd structures of the B type exhibited rectification (Fig. 1). The residual resistance of these samples determined for the linear portion of the *I–V* curves was significantly higher than the resistance of nonrectifying structures of the A type and varied within 10^4–10^5 Ω. The current passage direction always corresponds to positive voltage on the barrier (silver or indium) contact. The rectification coefficient determined as the ratio of the direct and reverse currents at $U = 0.4$ V in the B-type structures at $T = 300$ K reached 5–10. The absence of rectification in structures of the A type can be explained by defectness of the CdS layer resulting in the formation of conducting channels between the barrier metal contact and the cadmium substrate.

Barrier structures of the B type also exhibited a photovoltaic effect, which was most pronounced when the rectifying structures were illuminated from the side of barrier (silver or indium) contacts. The sign of the photo emf always corresponded to minus on the CdS layer, which agrees with the rectifying direction (assuming electron conductivity of the synthesized CdS films). In the best samples, the room-temperature photoresponse in the region of a linear dependence of the output voltage on the radiation intensity reached $\cong 10^2$ V/W.

Figure 2 shows the spectral dependence of the relative quantum efficiency $\eta(\hbar\omega)$ of the typical surface barrier structure based on a synthesized CdS film. As can be seen, the obtained structures exhibit photosensitivity in a broad range of photon energies $\hbar\omega \geq 1.7$ eV. The maximum quantum efficiency was observed at $\hbar\omega^{max} \approx 2.44$ eV ($T = 300$ K), which corresponds to the bandgap width of bulk CdS crystals [6, 7]. The short-wavelength decay of the photosensitivity in the region of $\hbar\omega \gtrsim 2.44$ eV can be related to insufficiently high quality of the Me(In,Ag)–CdS interface in the barrier structures obtained in this stage of research. On the other hand, this is a promising level that gives us hope that further development of CdS deposition technology will provide for a significant increase in the quantum efficiency of photoelectric converters. The long-wavelength limit of the photosensitivity of CdS-based Schottky barriers generally agrees with published data on the optical and photoinduced absorption in bulk CdS single crystals [7–9]. However, it should be noted that the energy position of this limit is displaced toward longer wavelengths as compared to the long-wavelength photosensitivity edge reported for the bulk CdS crystals in [3, 5], while the slope $S \cong 11$ eV^{-1} in the exponential region of the photosensitivity buildup in the interval of photon energies 1.9–2.2 eV is much lower than that in the bulk CdS crystals studied in [9]. This circumstance can be related to an increase in the density of charged centers in our thin CdS layers, which leads to smearing of the edges of empty bands by the electric fields of point defects of the crystal lattice.

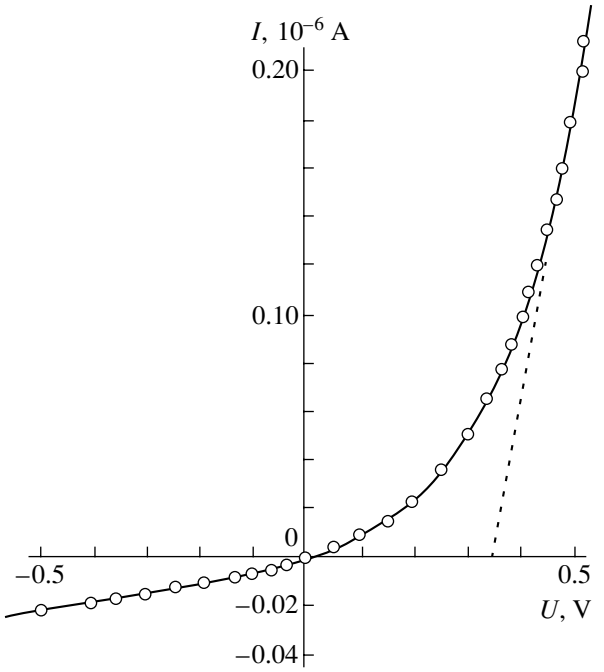

Fig. 1. Stationary dark current–voltage characteristic of an Ag/CdS/Cd surface barrier structure measured at $T = 300$ K (sample no. 2PT, current passage direction corresponds to positive bias voltage on the barrier layer).

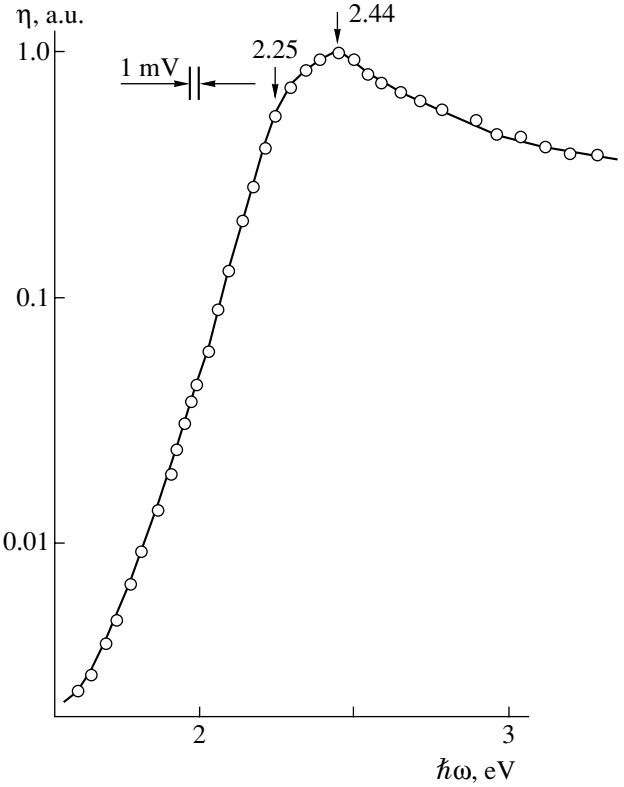

Fig. 2. Spectral dependence of the relative quantum efficiency η of photoconversion for the typical surface barrier structure Ag/CdS/Cd measured at $T = 300$ K (sample no. 2PT illuminated from the side of barrier layer). Arrows indicate the photon energies corresponding to spectral peculiarities.

In conclusion, we have developed a method for the electrochemical deposition of thin semiconducting CdS films from aqueous solutions onto metal substrates and showed the possibility of using this method in the economically profitable technology of highly effective thin-film photoelectric converters with large areas.

REFERENCES

1. *Proceedings of the ISES Solar World Congress on Solar Energy of a Sustainable Future, Göteborg, 2003.*
2. Tsuji Miwa, Aramoto Tetsuya, Ohyama Hideaki, *et al.*, Jpn. J. Appl. Phys., Part 1 **39**, 3902 (2000).
3. N. Kouklin, S. Bandyopadhyay, S. Tereshin, *et al.*, Appl. Phys. Lett. **76**, 460 (2000).
4. R. G. Dhere, M. M. Al-Jassim, Y. Yan, *et al.*, J. Vac. Sci. Technol. A **18**, 1604 (2000).
5. O. Vigil, O. Zelaja-Angel, and Y. Rodrigues, Semicond. Sci. Technol. **15**, 259 (2000).
6. *Physicochemical Properties of Semiconductors,* Ed. by A. V. Novoselova (Nauka, Moscow, 1978).
7. A. A. Abdurakhimov and Yu. V. Rud', Fiz. Tekh. Poluprovodn. (Leningrad) **16**, 959 (1982) [Sov. Phys. Semicond. **16**, 618 (1982)].
8. R. H. Bube, *Photoconductivity of Solids* (Wiley, New York, 1960; Inostrannaya Literatura, Moscow, 1962).
9. D. Du Hon, Phys. Rev. **112**, 758 (1958).

Translated by P. Pozdeev

Technical Physics Letters, Vol. 30, No. 8, 2004, pp. 631–632. Translated from Pis'ma v Zhurnal Tekhnicheskoĭ Fiziki, Vol. 30, No. 15, 2004, pp. 25–29.

Predetonation Conductivity of a TATB-Based Explosive

M. M. Gorshkov, K. F. Grebyonkin*, V. T. Zaikin, V. M. Slobodenyukov, and O. V. Tkachev

All-Russia Research Institute of Technical Physics, State Nuclear Research Center of the Russian Federation, Snezhinsk, Russia

** e-mail: k.f.grebyonkin@vniitf.ru*

Received February 17, 2004

Abstract—We have measured the electric conductivity of a low-sensitivity TATB-based explosive compressed by a shock wave. The results confirm the hypothesis that subthreshold shock waves induce the transition of crystalline explosives into a semiconductor state. © *2004 MAIK "Nauka/Interperiodica".*

In recent years, much attention has been devoted to the so-called predetonation conductivity observed in heavy metal azides, whereby the electric conductivity of such crystalline explosives exhibits a significant increase in the initial stage of explosion development, prior to the intense energy evolution and mechanical fracture of the material [1].

The aim of this study was to check for the possible development of predetonation conductivity in a low-sensitivity explosive based on triaminotrinitrobenzene (TATB) under the action of a shock wave with a pressure at the wave front close to the detonation initiation threshold. It should be recalled that TATB under normal conditions is a good insulator. The electric conductivity of this explosive under shock wave loading conditions was not measured previously.

The conductivity measurements were performed using the stick technique [2], whereby a thin rectangular plate of the material studied is oriented parallel to the shock wave front and placed in a medium retaining its insulating properties in the pressure range studied. In this study (as well as in [2]), the medium was a paraffin–corundum (30 : 70 w/w) mixture (gramiculit-2) selected so as to provide the coincidence of shock wave adiabates of the medium and the material studied [3]. Electrodes of the measuring circuit were connected to the sample stick ends. The electric field in the sample was parallel to the shock wave front. The sample had the dimensions $25 \times 4 \times 0.75$ mm and an initial density of 1.905 g/cm^3. The experimental arrangement is schematically depicted in Fig. 1. The sample in the assembly was loaded by a shock wave from a generator creating a rectangular pressure pulse. As a result, constant pressure was maintained in the sample for 1.5–2.0 μs until arrival of the unloading wave from an organic glass plate.

The electric conductivities of the auxiliary materials (gramiculit-2 and Vaseline filling the gaps) under the same shock loading conditions were studied in special experiments and have proved to be several orders of magnitude lower than the conductivity of the explosive under consideration.

We have measured the conductivity of a TATB-based explosive for pressures at the shock wave front in the range from 8.2 to 34.3 GPa. Shock-wave loading to a pressure of 8.2 and 11.14 GPa did not lead to an increase in the conductivity above the initial (background) level.

The measurements at 14.8 GPa and above revealed a significant increase in the conductivity between electrodes when the shock wave entered the sample. Figure 2 shows the plot of conductivity g versus time observed in the experiment with a pressure amplitude of 17.7 GPa. This curve exhibits two regions with significantly different rates of the conductivity buildup. Initially, for a certain period of time after the arrival of the shock wave, the conductivity grows at a relatively low rate, but then the growth rate sharply increases.

The sharp buildup of the conductivity in the second stage can be naturally related to the process of energy evolution accompanying reactive decomposition of the main body of explosive and to an increase in the volume

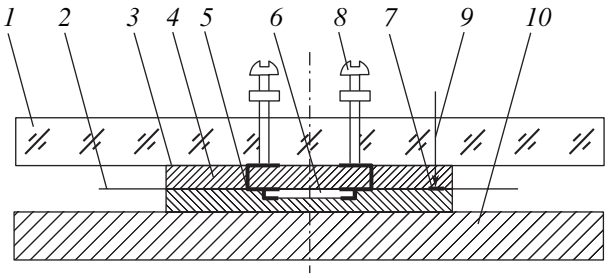

Fig. 1. Schematic diagram of the experimental arrangement: (*1*) organic glass plate; (*2*) Al foil, Δ = 0.01 mm; (*3*) gramiculit-2 disk, ∅60 × 5 mm; (*4*) gramiculit-2 disk, ∅60 × 3 mm; (*5*) Al foil, Δ = 0.050 mm; (*6*) sample (IS), $25 \times 4 \times 0.75$ mm; (*7*) Al foil, ∅5 × 0.05 mm; (*8*) contact screws; (*9*) reference pressure sensor; (*10*) charge screen.

1063-7850/04/3008-0631$26.00 © 2004 MAIK "Nauka/Interperiodica"

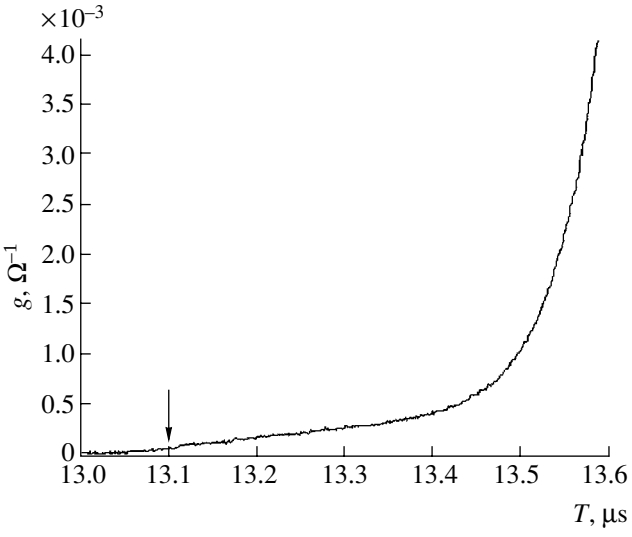

Fig. 2. Interelectrode conductivity kinetics measured for a shock wave front pressure of 17.7 GPa (arrow indicates the moment of shock wave escape from the sample).

fraction of products with high conductivity in the heterogeneous reaction medium. At a pressure of 23.9 GPa and above, the rapid conductivity growth stage terminates on reaching a level of $g \sim 100$ $(\Omega\ \mathrm{m})^{-1}$, which is typical of the decomposition products of condensed high explosives [4] and can be considered as evidence of the complete conversion of explosives into such products.

Thus, the results of our experiments indicate that a low-sensitivity TATB-based high explosive compressed by a shock wave front with a pressure of ≥15 GPa exhibits the phenomenon of predetonation conductivity. The duration of the first stage of the conductivity buildup strongly depends on the pressure at the shock wave front and is on the order of 1 μs at 14.8 GPa, 0.3–0.4 μs at 17.7 GPa, and about 0.1 μs at 23.9 GPa.

In experiments with a pressure of 14.8 and 17.7 GPa at the shock wave front, the specific conductivity of the explosive measured at the moment of the shock wave escape from the sample was on the order of 1 $(\Omega\ \mathrm{m})^{-1}$, which is close to the values for semiconductors such as germanium.

On the whole, the results obtained in this study agree with the hypothesis [5–7] according to which the action of subthreshold shock waves may lead to the injection of conduction electrons to a rather high density in TATB crystals, whereby the electron conductivity of this explosive increases to a level characteristic of semiconductors.

In conclusion, it should be noted that recently Chambers *et al.* [8] studied the electromagnetic properties of shock-wave-compressed crystalline RDX and also concluded that this action converts RDX into a semiconductor. Thus, the semiconductor detonation model proposed in [5, 6] probably has a universal character. The base assumption of this model, according to which the combustion wave originating from microscopic foci in detonating explosive propagates by means of electric conductivity, can be valid not only in TATB-based explosives but in RDX, HMX, TNT, and other explosives as well. In this context, it would be of interest to carry out analogous measurements of conductivity kinetics during the shock wave loading of high explosives of other types.

REFERENCES

1. Yu. A. Zakharov, E. D. Aluker, B. P. Aduev, *et al.*, *Predetonation Phenomena in Azides of Heavy Metals* (TsÉI Khimmash, Moscow, 2002).
2. Yu. N. Zhugin, K. K. Krupnikov, and N. A. Ovechkin, Khim. Fiz. **7**, 1447 (1987).
3. E. V. Shorokhov and B. V. Litvinov, Khim. Fiz. **12**, 722 (1993).
4. S. D. Gilev and A. M. Trubachev, Fiz. Goreniya Vzryva **38**, 104 (2002).
5. K. F. Grebenkin, Pis'ma Zh. Tekh. Fiz. **24** (20), 1 (1998) [Tech. Phys. Lett. **24**, 789 (1998)].
6. K. F. Grebenkin, in *Proceedings of the 5th International Conference at Zababakhin Scientific Readings, Snezhinsk, 1998* (VNIITF, Snezhinsk, 1999), pp. 189–194.
7. K. F. Grebenkin, A. L. Zherebtsov, A. L. Kutepov, and V. V. Popova, Zh. Tekh. Fiz. **72** (11), 114 (2002) [Tech. Phys. **47**, 1458 (2002)].
8. G. P. Chambers, R. G. Lee, T. J. Oxby, *et al.*, in *Shock Compression of Condensed Matter-2001*, Ed. by M. D. Furish, N. N. Thadhani, and Y. Horie (AIP, 2002), pp. 894–897.

Translated by P. Pozdeev

Technical Physics Letters, Vol. 30, No. 8, 2004, pp. 633–634. Translated from Pis'ma v Zhurnal Tekhnicheskoĭ Fiziki, Vol. 30, No. 15, 2004, pp. 30–34.

Controlled Chaos in an Oscillator with Additional Oscillatory Circuit

Er. V. Kal'yanov

Institute of Radio Engineering and Electronics (Fryazino Branch), Russian Academy of Sciences, Fryazino, Moscow oblast, Russia

e-mail: erast@ms.ire.rssi.ru

Received February 9, 2004

Abstract—A system comprising the classical van der Pol oscillator coupled with an additional oscillator circuit is considered in the presence of an algorithm ensuring chaotization of the self-sustained oscillations. A mathematical model of the system is described and the results of numerical analysis illustrating the new method of chaotizing coupling are presented. © *2004 MAIK "Nauka/Interperiodica".*

The classical van der Pol oscillator is a representative of self-sustained oscillators. A system of such an oscillator inductively coupled with an additional oscillatory circuit is well known and even considered in handbooks (see, e.g., [1]). However, such systems were mostly studied using approximate analytical methods. The van der Pol oscillator with additional oscillatory circuit exhibits only regular oscillations and offers a good example of a system with increased stability of oscillations [2–4]. In this context, the possibility of chaotization of the self-sustained oscillations in such a system may seem paradoxical. Nevertheless, it is possible to introduce chaos into this system by using a simple algorithm of a mutual chaotizing coupling between the master oscillator and the additional oscillatory circuit.

This paper is devoted to an analysis of processes in the van der Pol oscillator coupled with an additional oscillatory circuit under the conditions of chaotization of the self-sustained oscillations.

Equations describing the van der Pol oscillator coupled (inductively) with an additional oscillatory circuit can be written as follows [1]:

$$\begin{aligned} d^2x/dt^2 - \mu(1-x^2)dx/dt + x &= m_1 d^2y/dt^2, \\ d^2y/dt^2 + \varepsilon\mu dy/dt + \xi y &= m_2 d^2x/dt^2. \end{aligned} \tag{1}$$

Here, x and y are the dimensionless variables; ε, μ, and ξ are positive parameters; and $m_{1,2}$ are the coupling coefficients.

With certain values of parameters in Eqs. (1), the system has two basins of attraction (P_1 and P_2), corresponding to the lower and upper frequencies (slow- and fast-wave basins of attraction, respectively). However, even provided that the excitation conditions (phase and amplitude balance) for both frequencies are satisfied, prolonged realization of biharmonic oscillations is impossible. The oscillations are self-excited in one of the two basins of attraction, while oscillations in the other basin of attraction can be considered as possible (potential self-sustained oscillations). These oscillations are excited upon changing parameters of the system or the initial conditions, as well as upon additional excitation by an external force operating at a frequency close to that corresponding to potential self-sustained oscillations in the other basin of attraction.

It is possible to produce chaotization of the regime by changing the basins of attraction of the self-sustained oscillations by setting an algorithm ensuring variation of the detuning parameter ξ. This nonlinear condition can be formulated as follows:

$$\xi = \begin{cases} \xi_1, & \text{if} \quad x > y, \\ \xi_2, & \text{if} \quad x < y, \end{cases} \tag{2}$$

where ξ_1 and ξ_2 are the values of detuning for which oscillations are excited in one of the two basins of attraction. For certainty, let $\xi = \xi_1$ and ξ_2 correspond to the excitation of oscillations in the basins of attraction P_1 and P_2, respectively.

Equations (1) with conditions (2) define a mathematical model describing the controlled nonlinear chaotization of oscillations in the van der Pol oscillator with an additional oscillatory circuit. We performed numerical calculations for this system with the parameters $\mu = \varepsilon = 1$ using the fourth-order Runge–Kutta method with an integration time step of $t = 0.006$. The master oscillator was assumed to be symmetrically coupled with the additional circuit: $m_1 = m_2 = m$.

As was noted above, the presence of two basins of attraction in the system under consideration allows forced switching of the oscillations from one basin of attraction to the other. For the investigation of processes involved in this switching by means of a chaotizing coupling algorithm, it is expedient to select a regime in which a region of bistability exists within a certain interval of the detuning parameter. For example, such a region

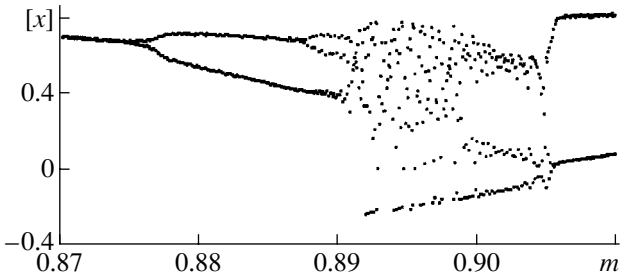

Fig. 1. A plot of the maximum value of variable $x(t)$ versus coupling parameter m (the initial condition was 0.1 for all variables).

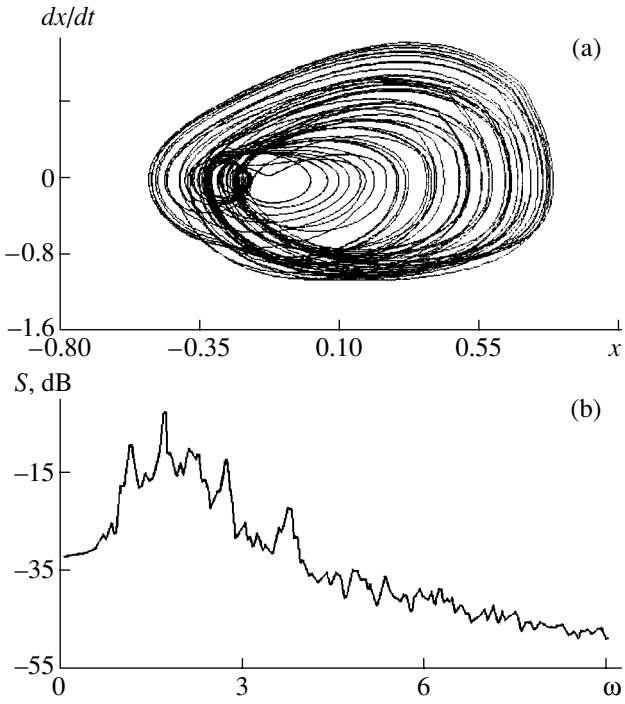

Fig. 2. (a) The phase portrait for $t \in [0, 180]$ and (b) the power spectrum calculated for the initial conditions corresponding to the values of variables for $m = 0.8950807$ in Fig. 1.

exists for Eqs. (1) with the coupling parameter $m = 0.9$. In this case, oscillations are switched in the vicinity of $\xi = \xi_0 \approx 1$. For $\xi = 0.98$, oscillations are self-excited at the upper frequency ($\omega = 1.96$), while for $\xi = 1.02$, the system is self-excited at the lower frequency ($\omega = 0.97$). A short (within $t \in [0, 40]$) action of the external harmonic drive signal with a frequency of $\Omega = 1$ and an amplitude of $A = 0.04$ induces self-sustained oscillations in the slow-wave basin of attraction P_1 with a frequency of $\omega = 0.96$. If the external drive signal is not switched off at $t > 40$, the system exhibits a regime of forced synchronization with the induced oscillations at $\omega = \Omega$.

Taking into account the above peculiarities in the behavior of the van der Pol oscillator with an additional oscillatory circuit, it was expedient to perform a numerical analysis of the proposed chaotization regime for the detuning parameters selected so that $\xi_1 > \xi_0$ and $\xi_2 < \xi_0$. Our calculations were conducted for $\xi_1 = 1.3$ and $\xi_2 = 0.5$.

Figure 1 presents a bifurcation diagram showing variation of the maximum value of the variable $x(t)$ (denoted by $[x]$) in the course of adiabatic increase in the coupling parameter m. As can be seen, for $m \in [0.89, 0.91]$, there is irregular scatter of points corresponding to the maximum values of $x(t)$, which is evidence of chaotization of the oscillatory process. The transition to chaos proceeds via period-doubling bifurcations (Feigenbaum scenario). In the chaotic regime, oscillations in the two basins of attraction exhibit competition and the system behaves as if it permanently occurs in the transient regime.

In the case of adiabatic decrease in the coupling parameter, the interval of m corresponding to chaos somewhat shifts toward lower values (i.e., exhibits a hysteresis). The system leaves the regime of chaotic oscillations by means of reverse (period-halving) bifurcations.

Figure 2 shows the characteristic phase portrait (attractor map) (a) and the power spectrum S (b) of this system calculated for a coupling coefficient corresponding to irregular scatter of points in Fig. 1. The phase portrait reflects a chaotic character of oscillations established in the system with regular dynamics under the action of the simplest chaotizing coupling algorithm determined by the detuning parameter. The structure of this phase portrait resembles that of the Rössler attractor. The oscillation power spectrum is continuous but exhibits resonance peaks in the spectral power density of oscillations. This spectrum is indicative of a good intermixing of the phase trajectories. The characteristic Lyapunov exponent in the regime corresponding to the calculated spectrum is $\lambda = 0.31$.

In conclusion, the results presented above show that self-sustained oscillations in the van der Pol oscillator with an additional oscillatory circuit confirm can be chaotized using a rather simple chaotizing coupling algorithm. It should be noted that the chaotization of oscillations in this system can also be provided by using a chaotization feedback algorithm considered in [3] in application to oscillators with inertia.

Acknowledgments. This study was supported by the Russian Foundation for Basic Research, project no. 04-02-16536.

REFERENCES

1. P. S. Landa, *Self-Oscillation in Systems with Finite Number of Degrees of Freedom* (Nauka, Moscow, 1980).
2. S. I. Bychkov, N. I. Burenin, and R. T. Safarov, *Stabilization of Frequency in Microwave Oscillators* (Sov. Radio, Moscow, 1962).
3. B. E. Zhelezovskiĭ and É. V. Kal'yanov, *Multifrequency Operating Modes in Microwave Devices* (Radio i Svyaz', Moscow, 1978).
4. É. V. Kal'yanov, Nonlinear World **1** (1–2), 45 (2003).

Translated by P. Pozdeev

Technical Physics Letters, Vol. 30, No. 8, 2004, pp. 635–637. Translated from Pis'ma v Zhurnal Tekhnicheskoĭ Fiziki, Vol. 30, No. 15, 2004, pp. 35–40.

Magnetic Field Control of a Supersonic Nitrogen Flow

S. V. Bobashev[a], N. P. Mende[a], V. A. Sakharov[a,*], and D. M. Van Wie[b]

[a] *Ioffe Physicotechnical Institute, Russian Academy of Sciences, St. Petersburg, 194021 Russia*

[b] *Johns Hopkins University, Laurel, Maryland, USA*

** e-mail: v.sakharov@mail.ioffe.ru*

Received February 25, 2004

Abstract—Magnetohydrodynamic impact on a cold supersonic nitrogen flow with external magnetic field was realized in an experimental complex based on the Big Shock Tube at the Ioffe Physicotechnical Institute. A pulsed supersonic flow with a Mach number of $M = 4$ and steady phase duration of about 1.5 ms was created by expansion of the shock-heated nitrogen flow from a supersonic nozzle. The gas was ionized by pulsed discharge between two electrodes mounted on the nozzle wall so that an electric current of up to ~500 A passed in the direction perpendicular to the gas flow at the dielectric wall. External magnetic field ~0.3 T was perpendicular to the gas flow and the current direction. It is established that the magnetic field significantly modifies the shock wave structure in the flow. © *2004 MAIK "Nauka/Interperiodica".*

In an experimental complex based on the Big Shock Tube (BST), hydrogen is the driving gas and nitrogen is the working gas filling a low-pressure channel. The channel edge is adjacent to a rectangular test chamber with a flat supersonic nozzle. The test chamber is separated from the channel by a thin plastic diaphragm, which allows a low pressure on the order of 1 Pa to be maintained in the chamber.

The test chamber walls and the nozzle parts are made of a dielectric material. The lateral vertical walls of the chamber are provided with glass windows for optical diagnostics of the gas flow structure by means of a coaxial schlieren device viewing the nozzle region. The distance between windows (equal to the nozzle width) is 75 mm. Electromagnetic coils situated above and below the chamber are arranged so that their common axis crosses the axis of windows. These coils generate pulsed magnetic field with a duration of 4.5 ms and magnetic induction of up to 1.5 T. The experimental setup is described in more detail elsewhere [1].

Nitrogen filling the low-pressure channel is heated by the shock wave reflected from the channel edge on which the inlet of the supersonic nozzle occurs. The temperature of nitrogen behind the reflected shock wave front reaches ~1700 K. The gasdynamic parameters of the flow in front of the nozzle inlet remain constant for approximately 1.5 ms. Passing through the wedge-shaped nozzle, nitrogen is accelerated to a supersonic velocity corresponding to the Mach number M = 4. At the nozzle outlet, the gas has a pressure of ~5 kPa, a temperature of ~400 K, and a velocity of ~1600 m/s.

Figure 1 schematically shows the test chamber design and the main elements of the electric circuit. In the outlet cross section of the nozzle (which has a height of 95 mm), two electrodes are flash-mounted in one of the nozzle walls (lower wall in Fig. 1) in the region near the windows. The electrodes have the dimensions 6×4 mm in plane, with the longer side oriented in the flow direction. Electric current passed through the working gas with the aid of these electrodes

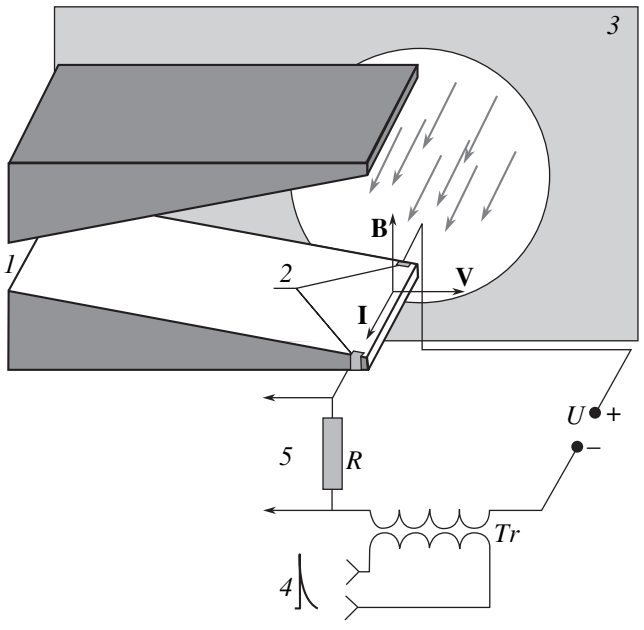

Fig. 1. Schematic diagram of the test chamber design and electric circuit: (*1*) nozzle; (*2*) electrodes; (*3*) test chamber wall with window; (*4*) initiating voltage pulse; (*5*) to oscillograph (*B*, *I*, and *V* are vectors of the magnetic induction, electric current, and working gas flow, respectively).

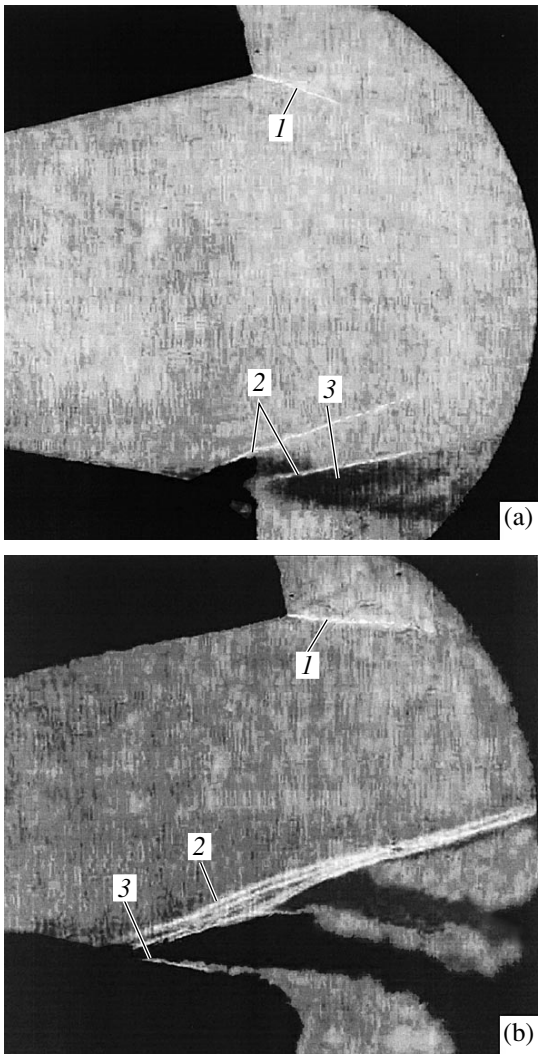

Fig. 2. Schlieren patterns of the flow structure at the nozzle outlet observed for (a) $I = 400$ A, $B = 0$ and (b) $I = 500$ A, $B = 0.3$ T.

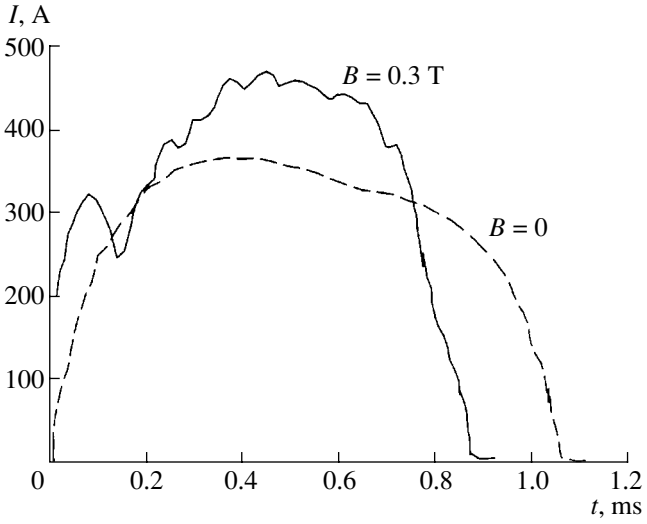

Fig. 3. Oscillograms of the electric current passing through the ionized nitrogen flow without (dashed line) and with (solid line) applied magnetic field.

provides for the magnetohydrodynamic (MHD) impact on the gas flow.

Since the supersonic nitrogen flow is not ionized, the main problem is to provide for conductivity in the gas during its steady flow in the nozzle. The simplest method is based on initiation of a working current by means of a single high-voltage discharge between electrodes. For this purpose, electrodes (Fig. 1) are connected to an electric circuit comprising serially connected source of pulsed voltage *U*, high-voltage pulse transformer *Tr*, and load resistor *R*. The voltage *U* was generated by a distributed line consisting of 14 like *LC* cells with a characteristic discharge time of 800 μs, which was charged to a preset voltage prior to experiment. Transformer *Tr* forms a high-voltage pulse initiating the discharge between electrodes.

The operation of all devices is synchronized by a signal from a pressure sensor situated in the shock tube channel at a certain distance from the test chamber. The sequence of operation of the magnetic system and the circuit initiating discharge in the nitrogen flow is adjusted so as to provide for the working current passage through the steady flow in the nozzle at the moment of maximum magnetic induction. After establishment of a steady flow in the nozzle (~300 μs past the nozzle start), a high-voltage pulse (with a length of several microseconds) is applied to the primary winding of the transformer. The resulting breakdown initiates discharge of the source of pulsed voltage *U*. The current passes through the supersonic gas flow for ~1 ms and reaches several hundred amperes.

In the first stage, the experiments were performed without magnetic field application, the working current through the plasma was measured, and the pattern of flow at the nozzle outlet was observed. Figure 2a presents the schlieren pattern of the flow obtained in the steady state at the moment of current passage with an amplitude of $I = 400$ A. Since the gas flow in the nozzle is symmetric with respect to the central plane, the effect of electric discharge on the flow can be evaluated by comparing the flow structure at the upper edge (free of electrodes) and the lower edge (with electrodes). The top part of the pattern displays a characteristic weak discontinuity *1* accompanying the supersonic gas expansion at the sharp edge. The bottom part of the pattern reveals weak shock waves *2* (formed as a result of plasma heating by the current) and a turbulent shear layer *3* downstream from the shock.

Switching on the magnetic field with the Lorentz force directed opposite to the flow velocity vector significantly changes the flow structure. Figure 2b shows a schlieren pattern observed with the MHD drag effect at the same moment of time past the nozzle start as the pattern in Fig. 1. The magnetic induction amplitude was $B = 0.3$ T and the current amplitude was $I = 500$ A. Similar to Fig. 2a, the top part of the pattern shows only a weak discontinuity *1*. A characteristic feature of the flow structure in this case is the sharply pronounced

strong shock wave *2* originating from a point situated ~30 mm upstream from the nozzle edge. Interaction of the shock wave with a boundary layer at the nozzle wall leads to the flow separation *3* immediately downstream from the shock.

Figure 3 shows oscillograms of the current pulses corresponding to the two cases presented in Fig. 2. As can be seen, the presence of magnetic field (solid curve) significantly changes the character of establishment of the working current in the supersonic nitrogen flow. In this case, the current pulse has two maxima: the first corresponds to the stage of flow formation, and the second, to the steady expansion stage. Estimates show that the ratio of the power of electric heating of the gas to the power of supersonic flow does not exceed 0.5. The ratio of pressures behind and in front of the shock wave front (calculated using the wave front slope relative to the nozzle surface and the local Mach number) amounts to approximately 5.

In conclusion, it should be noted that this study continues a series of investigations devoted to the MHD control of supersonic flows. In contrast to the previous experiments using weakly ionized xenon as the working gas, we have succeeded in realizing for the fist time the effective MHD impact on a cold supersonic flow of nitrogen.

Acknowledgments. This study was supported by EOARD (ISTC project no. 2009).

REFERENCES

1. S. V. Bobashev, N. P. Mende, V. A. Sakharov, and D. M. Van Wie, AIAA Pap., No. 2003-169 (2003).

Translated by P. Pozdeev

Technical Physics Letters, Vol. 30, No. 8, 2004, pp. 638–640. Translated from Pis'ma v Zhurnal Tekhnicheskoĭ Fiziki, Vol. 30, No. 15, 2004, pp. 41–47.

Photoelectron Spectra of Yb–Si(100) Heterointerfaces Formed at Room Temperature

D. V. Vyalikh[a], M. V. Kuzmin[a], M. A. Mittsev[a,*], and S. L. Molodtsov[b,]**

[a] *Ioffe Physicotechnical Institute, Russian Academy of Sciences, St. Petersburg, 194021 Russia*

[b] *Institute of Physics, Dresden Technical University, Dresden, Germany*

*e-mail: * m.mittsev@mail.ioffe.ru; ** molodtsov@physik.phy.tu-dresden.de*

Received February 12, 2004

Abstract—The laws of formation of the heterointerfaces formed upon ytterbium (Yb) deposition at room temperature (T = 300 K) onto a (2 × 1)-reconstructed Si(100) surface were studied by methods of photoelectron spectroscopy (PES) with excitation by synchrotron radiation and low-energy electron diffraction (LEED). In the range of submonolayer surface coverages θ, the adsorption of Yb atoms leads to destruction of the surface dimers. This is accompanied by the formation of an amorphous film consisting of mixed Yb and Si atoms. For θ > 1.5, a partly ordered metallic ytterbium film containing dissolved Si atoms is formed on the substrate surface. In all stages of deposition, there is charge transfer from Yb to Si atoms, which is manifested by a shift of the Si 2*p* core level. This shift is especially pronounced (reaching 1.5 eV) for silicon atoms dissolved in the metallic film. © *2004 MAIK "Nauka/Interperiodica".*

Photoelectron spectroscopy (PES), including the variant with excitation by synchrotron radiation, is a powerful tool for studying solid surfaces. This is related primarily to the fact that the electronic state of atoms occurring on the surface or in a subsurface layer is highly sensitive to both chemical environment and the structure of the uppermost and subsurface layers. For this reason, information concerning both the mechanism of formation of interfaces and their physicochemical properties can be extracted from photoelectron spectra.

This paper briefly describes the results of PES investigation of a thin-film structure formed upon deposition of ytterbium onto a (2 × 1)-reconstructed Si(100) surface. The Yb–Si(100) interface is essentially a model system for some rare earth elements (including ytterbium) whose valence during the interaction with silicon frequently increases from 2+ to a certain fractional value 2 + x (x < 1). To our knowledge, no such experiments have been reported so far.

Thin-film structures were obtained by room-temperature deposition of ytterbium on the surface of single crystal silicon. The experiments were performed using a photoelectron spectrometer and a synchrotron radiation channel of the Russian–German Laboratory at the BESSY II storage ring (Berlin, Germany). The overall energy resolution of the electron energy analyzer and monochromator was 150 meV. The photoelectron spectra were obtained using synchrotron radiation with a primary photon energy of $h\nu$ = 130 eV, which corresponded to photoelectron spectra of the Si 2*p* core levels, and $h\nu$ = 108 eV, which allowed us to study the valence band of silicon and the Yb 4*f* level. The state of the sample surface and the structure of surface films formed in the course of ytterbium deposition were monitored by low-electron energy diffraction (LEED).

The samples were prepared using *n*-type single crystal silicon wafers with a resistivity of about 1 Ω cm. Prior to experiments, the wafers were heated in a vacuum chamber of the photoelectron spectrometer, first for 2 h at 900 K and then for a short time at 1450 K. This treatment ensured obtaining of an atomically clean Si(100)2 × 1 reconstructed surface. Ytterbium atoms were deposited onto the substrate surface by evaporation from tantalum Knudsen cells. The residual pressure in the spectrometer chamber during evaporator operation did not exceed 8×10^{-10} mbar. The rate of deposition was 0.01–0.08 monolayer per second (one monolayer coverage of Yb atoms corresponds to their surface density of 6.78×10^{14} cm^{-2}, which equals the density of silicon atoms on the Si(100) surface). The PES measurements were performed at room temperature in a vacuum of 1×10^{-10} mbar.

Figure 1 shows the Si 2*p* photoelectron spectra observed for the Yb–Si(100) system studied. Each spectrum is normalized to the maximum peak height. As can be seen from Fig. 1a, deposition of even a very small amount of ytterbium (see the spectrum for a surface coverage of θ = 0.15) leads to a decrease in the manifestation of features related to the valence band and to the appearance of two well-resolved peaks due to divalent Yb atoms [1]. In the interval 0.15 < θ ≤ 1.5, an increase in the metal coverage is accompanied by complete disappearance of the valence-band signals and by broadening of the ytterbium peaks. This broadening is probably related to the fact that Yb atoms

occupy various positions in the surface structures formed, which can take place in the case of formation of disordered structures. In the range of coverages $\theta > 1.5$, the spectra become more complicated, displaying additional resolvable components. Eventually, at $\theta > 3$, the spectra are identical with the spectra of thick films of metallic ytterbium deposited on a tantalum substrate [1]. This result indicates that exposure to a sufficiently large dose of Yb atoms leads to the formation of a metallic ytterbium film on the Si(100) substrate.

The above conclusions are confirmed by the spectra of Si 2*p* core levels (Fig. 1b). Here, spectrum *1* corresponds to the initial clean surface of silicon. This spectrum, as was demonstrated in a number of papers (see, e.g., [2, 3]), comprises a superposition of signals from Si atoms occurring on the crystal surface, in the subsurface layers, and in the bulk. According to recent data [3], the spectrum of the Si 2*p* level involves six components. Two of these are due to the surface dimers. As is known, such dimers are formed as a result of the 2×1 reconstruction of the Si(100) crystal face. Resulting from superposition of all six components, the spectrum has two main peaks at binding energies of 99.2 and 99.8 eV and a shoulder (S_U in Fig. 1b) at lower binding energies. The latter feature is attributed to dimers [4, 5]; its shape depends on the degree of perfection of the crystal surface and on the energy resolution of a particular spectrometer.

As can be seen from Fig. 1b, deposition of even a very small amount of ytterbium (see the spectrum for a surface coverage of $\theta = 0.15$) significantly attenuates the S_U signal. This implies that the metal atoms destruct dimers. As the degree of coverage increases, the region of S_U transforms first (at $\theta \approx 0.3$) into a long tail extending toward lower binding energies and then into a very broad peak eventually (at $\theta = 1$) beginning to dominate in the spectrum. As the metal coverage increases further, the latter peak shifts toward lower binding energies and, at $\theta \geq 1.5$, transforms into two quite well-resolved peaks. The spacing of these peaks on the energy scale is the same as that for the clean silicon surface, but both peaks are significantly (1.5 eV) shifted toward lower binding energies.

The above, rather complicated pattern of evolution of the photoelectron spectra of Si 2*p* core level of silicon can be convincingly interpreted assuming that the formation of an Yb–Si(100) heterointerface involves the following processes:

(a) intermixing of Si and Yb atoms at the interface;

(b) dissolution of Si atoms in the metallic ytterbium film;

(c) charge transfer from electropositive Yb atoms to electronegative Si atoms, which decreases the binding energy of electrons populating the Si 2*p* level.

Indeed, evolution of the Si 2*p* spectrum observed in the region of $\theta < 1.5$ consists in the formation of a very broad peak to the right of the signals of pure silicon.

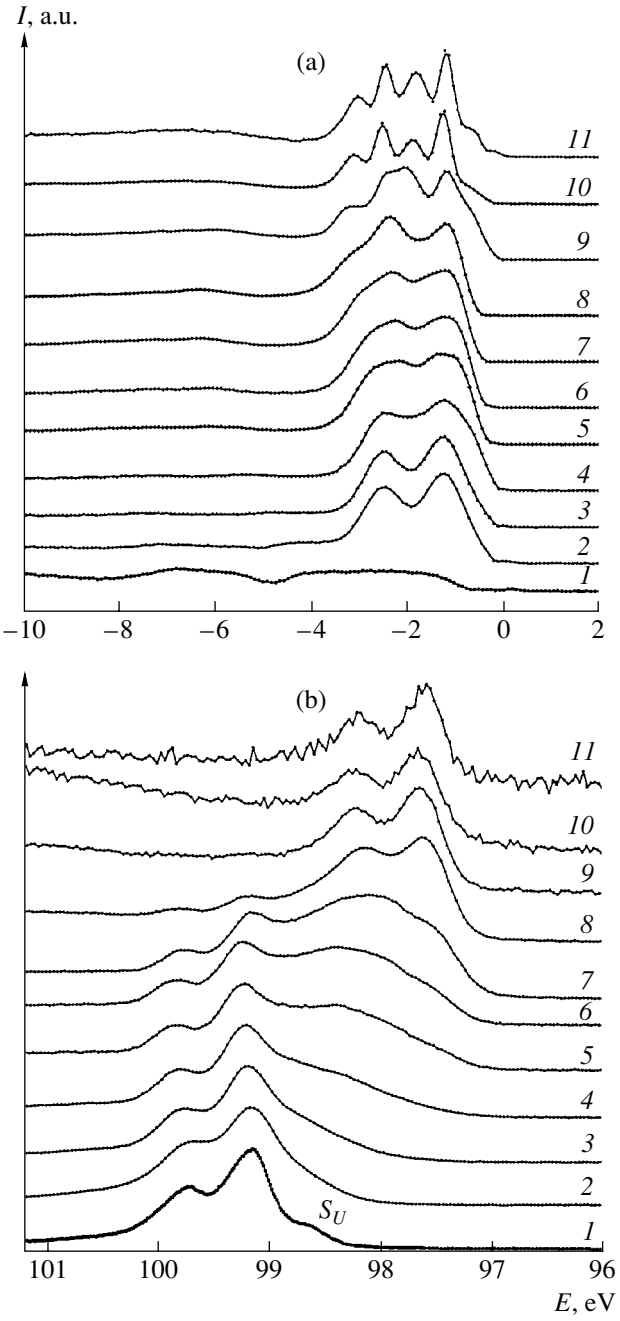

Fig. 1. Normalized photoelectron spectra of (a) the valence band of silicon and the Yb 4*f* level and (b) the Si 2*p* level in the Yb–Si(100) system for the degree of ytterbium coverage $\theta = 0$ (*1*), 0.15 (*2*), 0.3 (*3*), 0.5 (*4*), 0.7 (*5*), 0.85 (*6*), 1.0 (*7*), 1.5 (*8*), 3 (*9*), 8 (*10*), and 20 (*11*). The spectra were excited using photon energies $h\nu = 108$ (a) and 130 eV (b).

This result is indicative of the charge transfer from deposited Yb atoms to Si atoms. The very large width of the observed peak is related to the fact that Si atoms accounting for this signal occur on the surface in various states and, accordingly, possess different charges. This situation may arise if Si and Yb atoms form a disordered or amorphous two-component film. Obviously, the binding energy of electrons populating Si 2*p* levels

will vary, depending on the state in which the given atom occurs. If this variation exceeds the magnitude of the spin–orbit splitting for the Si 2*p* level (0.608 eV), the experimental spectra display a single broad signal instead of two peaks.

For $\theta > 0.15$, the broad signal splits into two narrow peaks. This implies that the number of possible states in which Si atoms can occur in the growing ytterbium film has significantly decreased. This is most likely related to the onset of formation of a quite ordered metallic ytterbium film containing dissolved Si atoms.

The above notions are partly confirmed by the Yb 4*f* spectra (Fig. 1a) and by the results of our structural investigations. Indeed, an increase in the amount of deposited ytterbium in the interval of coverages $0.15 < \theta \leq 1.5$ is accompanied by the broadening of peaks in the spectra of the Yb 4*f* level. This broadening indicates that Yb atoms occupy qualitatively different positions in the growing film. Apparently, a certain fraction of dissolved Si atoms can segregate at the film surface. However, the content of such atoms is likely to be small. This conclusion follows from the results of measurements of the work function [6]. According to these data, the change in the work function upon deposition of Yb atoms on Si(100) is very large, exceeding 2 eV for $\theta > 1$. Evidently, if the density of electronegative Si atoms on the surface of ytterbium film were large, the change in the work function would be much less pronounced.

For $\theta > 3$, the Yb 4*f* spectra are identical to the spectra of bulk ytterbium. This is evidence of the formation of a metallic ytterbium film featuring at least a short-range order.

According to the results of our structural investigation, the diffraction reflections of the clean (2×1)-reconstructed Si(100) surface disappear at $\theta \approx 0.5$, while the 1×1 pattern due to the bulk lattice of Si atoms practically vanishes at $\theta \approx 1$. These results can be considered as evidence that the deposition of Yb atoms up to a coverage of $\theta \leq 1$ is accompanied by the formation of a two-dimensional amorphous film comprising a mixture of Yb and Si atoms.

For the coverages $\theta \geq 3$, corresponding to the formation of a metallic ytterbium film (see Fig. 1a), the LEED pattern displayed only a diffuse background. However, this result does not contradict the conclusion, based on the spectra presented in Fig. 1b, according to which this coverage corresponds to a more or less ordered film. Indeed, this ordering may have a limited character, for example, in the case of a film consisting of misoriented crystallites. Obviously, such a film will not give a regular LEED pattern.

Thus, experimental results obtained in this study indicate that the deposition of ytterbium onto reconstructed Si(100)2×1 surface at 300 K in the range of submonolayer surface coverages θ leads to destruction of the surface dimers. This is accompanied by the formation of an amorphous film consisting of mixed Yb and Si atoms. For $\theta > 1.5$, a partly ordered metallic ytterbium film containing dissolved Si atoms is formed on the substrate surface. In all stages of deposition, there is charge transfer from Yb to Si atoms, which is manifested by a shift of the Si 2*p* core level. This shift is especially pronounced (reaching 1.5 eV) for silicon atoms dissolved in the metallic film.

Acknowledgments. The work was supported by the Ministry of Industry, Science, and Technology of the Russian Federation (project no. 40.012.1.1.1152) and by the Russian–German Laboratory at BESSY II (Berlin, Germany).

REFERENCES

1. R. Hofmann, W. A. Henle, F. P. Netzer, and M. Neuber, Phys. Rev. B **46**, 3857 (1992).
2. E. Landemark, C. J. Karlsson, Y.-C. Chao, and R. I. G. Uhrberg, Phys. Rev. Lett. **69**, 1588 (1992).
3. T.-W. Pi, C.-P. Ouyang, J.-F. Wen, *et al.*, Surf. Sci. **514**, 327 (2002).
4. C.-P. Cheng, I.-H. Hong, and T.-W. Pi, Phys. Rev. B **58**, 4066 (1998).
5. K. Nakamura, H. W. Yeom, H. Koh, *et al.*, Phys. Rev. B **65**, 165332 (2002).
6. M. Kuzmin, R. E. Perälä, P. Laukkanen, *et al.*, Appl. Surf. Sci. **214**, 196 (2003).

Translated by P. Pozdeev

Technical Physics Letters, Vol. 30, No. 8, 2004, pp. 641–643. Translated from Pis'ma v Zhurnal Tekhnicheskoĭ Fiziki, Vol. 30, No. 15, 2004, pp. 48–54.

Initial Stages of the MBE Growth of Silicon Carbide Nanoclusters on a Silicon Substrate

Yu. V. Trushin*, E. E. Zhurkin, K. L. Safonov, A. A. Schmidt, V. S. Kharlamov, S. A. Korolev, M. N. Lubov, and J. Pezoldt

Ioffe Physicotechnical Institute, Russian Academy of Sciences, St. Petersburg, 194021 Russia
St. Petersburg State Technical University, St. Petersburg, 195251 Russia
Zentrum für Mikro- und Nanotechnologien, TU Ilmenau, Postfach 100565, 98684 Ilmenau, Germany
** e-mail: trushin@theory.ioffe.rssi.ru*

Received February 12, 2004

Abstract—The growth of silicon carbide (SiC) nanoclusters by molecular beam epitaxy on silicon substrates has been studied using a combination of experimental and theoretical methods. The first results concerning the initial stages of this growth are presented. © *2004 MAIK "Nauka/Interperiodica".*

Unique properties of silicon carbide (SiC), including high thermal and radiation stability, high thermal conductivity, large breakdown fields, high carrier injection rate, the possibility of operation at high frequencies, and some others, make this wide-bandgap semiconductor very attractive for applications in micro- and optoelectronics [1]. However, this material still has not found wide use because of the considerable difficulties encountered in all attempts to obtain high-quality defect-free single crystals of required dimensions at acceptable expenditures. The most promising method of obtaining 3C-SiC samples is molecular beam epitaxy (MBE) on high-quality single crystal silicon substrates for which the production technology is well developed.

Another promising field of application for silicon carbide is related to the creation of semiconductor heterostructures with SiC-based quantum dots. In such structures, SiC nanoparticles can play the role of quantum antidotes of tunnel barriers. Unfortunately, because of the large mismatch of the coefficients of temperature expansion and the lattice parameters of silicon (5.43 Å) and silicon carbide (4.35 Å), considerable elastic stresses arise at the interface and lead to the formation of structural defects significantly impairing the quality of growing epilayers. Therefore, solving the task of obtaining high-quality SiC-based structures with desired characteristics requires a complex experimental and theoretical investigation of the processes involved in the initial stage of the epitaxial growth of SiC on the surface of silicon substrates.

In this context, we have experimentally studied the initial stages of nucleation and growth of silicon carbide under the conditions of MBE using electron-beam evaporation of carbon with deposition onto (111)- and (100)-oriented single crystal silicon substrates. The deposition conditions were varied within a broad range of substrate temperatures (350–1250°C) and carbon flux densities (10^{12}–10^{17} cm^{-2}). The structure and morphology of the deposits and the kinetics of related processes were studied by reflection high-energy electron diffraction (RHEED), atomic force microscopy (AFM), and spectral ellipsometry (SE) [2]. Using AFM data, we also determined the surface density, dimensions, and shapes of SiC clusters.

As a result of these experimental investigations, it was established that the MBE growth of SiC involves the following main stages:

(1) adsorption of carbon atoms;

(2) modification of the surface superstructure and the formation of a $Si_{1-y}C_y$ solid solution;

(3) nucleation of SiC in the $Si_{1-y}C_y$ solid solution;

(4) transition from quasi-two-dimensional (2D) to 3D growth of the nuclei;

(5) growth and coalescence of the nuclei;

(6) growth of the SiC epilayer and the formation of cavities on the silicon side of the SiC–Si interface.

The minimum temperature necessary for the formation of SiC was 500°C. Figure 1 shows an AFM image illustrating nucleation on a Si(111) surface exposed to a carbon flux of 5×10^{13} cm^{-2} s^{-1} for a time period of about 10 s at 925°C. As can be seen, MBE results in the formation of cone-shaped 3D clusters with an average radius on the order of 700 Å, an average height of about 40 Å, and a surface density on the order of 10^9 cm^{-2}.

A physical model describing the nucleation and growth of SiC nanoclusters must take into account microscopic features of the system studied, involving diffusion transport of Si and C atoms on the surface and in the bulk of substrate, the surface structure, the presence of elastic stresses in the crystal lattice, etc. However, it is very difficult to trace the evolution of this

1063-7850/04/3008-0641$26.00 © 2004 MAIK "Nauka/Interperiodica"

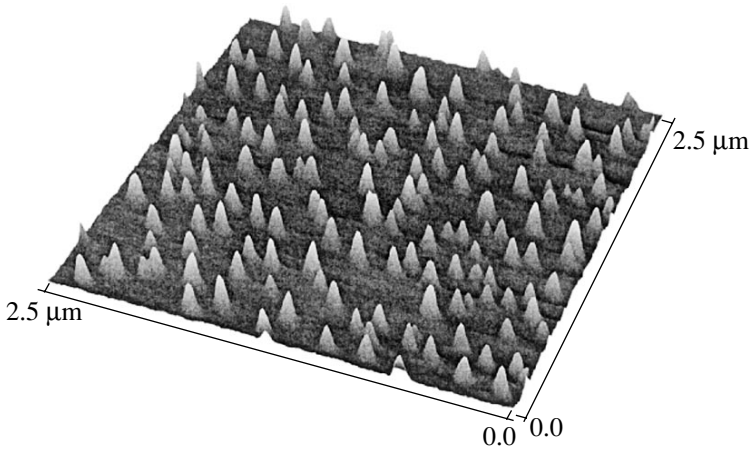

Fig. 1. AFM image of a Si(111) surface exposed for 5 s to an atomic carbon flux of 5×10^{13} cm^{-2} s^{-1} at 925°C.

macroscopic system on a macroscopic time scale. For this reason, we suggest using a combination of the aforementioned experimental techniques and a complex of computer-aided methods, including molecular dynamics, kinetic Monte Carlo calculations, and analysis of kinetic equations for modeling the growth of SiC nanoclusters and the evolution of their dimensions and shapes.

We have assessed the possibility of using the classical molecular dynamics (MD) method to estimate the activation energy of migration for carbon adatoms on the silicon crystal surface. The MD method, which is described in sufficient detail elsewhere (see, e.g., [3, 4]), reduces to solving the Newton equations of motion for a given system of atoms (representing a model crystal and growing crystalline clusters). The particular algorithm used in this study was described in [4–8]. Forces acting upon each atom were calculated using a many-body potential proposed by Tersoff [9], which is known to describe with good accuracy some properties of Si, C, and 3C-SiC, such as the cohesive energy, lattice parameters, elastic constants, and energies of point defect formation.

In order to determine the adsorption sites of atoms (Si or C) on the silicon surface and elucidate the possible pathways of diffusion, it is necessary to construct the so-called potential energy surface. The local minima on this surface correspond to the possible adsorption sites. The initial model considered Si adatoms on the Si(100) surface with a 2×1 reconstruction. The first calculation was performed for a silicon crystal with dimensions $6a_0 \times 6a_0 \times 6a_0$ (where a_0 is the crystal lattice parameter), possessing a diamond structure, a 2D periodicity, and two free (100) faces reconstructed according to the symmetric 2×1 superstructure (see, e.g., [10]). As is known, the uppermost layer of atoms in this reconstruction comprises rows of dimers aligned in the $\langle 110 \rangle$ direction. MD calculations for this surface were optimized by selecting a minimum periodicity cell with the *X* axis perpendicular to the rows of dimers and the *Y* axis parallel to these rows. The potential energy surface was calculated by placing an adatom in one of the preset positions (*x*, *y*) over a certain cell. The positions were selected proceeding from a uniform grid with a step of $0.04a_0$ (a total of 861 points). The initial height of the adatom over the surface was $0.5a_0$. Then, the total potential energy of the system was minimized so that atoms of the crystal could perform arbitrary displacements, while the adatom was capable of moving only in the *Z* axis direction (i.e., perpendicularly to the crystal surface).

Minimum activation energies of migration for Si adatom on a (2×1)-reconstructed Si(100) surface estimated using the MD method (this study), *ab initio* calculations [11], and experimental SEM data [12]

Activation energy of migration	MD	*Ab initio*	Experiment
E^m, eV	0.68	0.60	0.67 ± 0.08

In order to describe the diffusion of adatoms on the surface, it is necessary to determine the activation energy for the jumps between two adsorption sites. According to the results of Brocks *et al.* [11], there are two main directions for the possible diffusion of adatoms: along and across the rows of dimers on the reconstructed surface. An analysis of the potential energy profiles in these directions gave the values of minimum thresholds for the activation energy of migration along the rows (*Y* axis): $E_{Si}^m = 0.68$ eV for silicon (Fig. 2) and $E_C^m = 0.86$ eV for carbon. In the perpendicular direction (*X* axis), the minimum barrier height is the same (1 eV) for adatoms of both kinds. Thus, the surface diffusion of adatoms is anisotropic and proceeds predominantly along the rows of dimers. This conclusion, as well as the estimates obtained for the activation energy of migration agree well with the results of *ab initio* calculations [11] and with experimental data obtained by scanning electron microscopy (SEM) [12]. The mini-

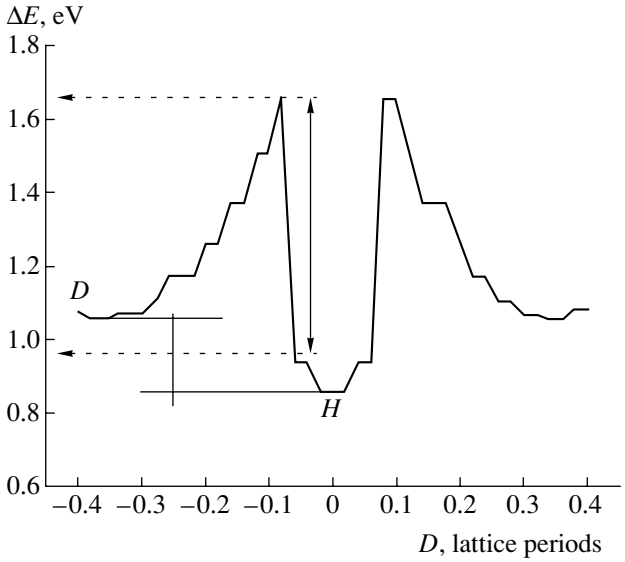

Fig. 2. Potential energy profile of a Si adatom on a (2×1)-reconstructed Si(100) surface in the direction corresponding to a minimum barrier for the surface migration (*D* and *H* are the local energy minima; the arrow indicates the barrier height).

mum estimates of E^{m} obtained by different methods are listed in the table.

The MD method cannot be used for simulating the process of cluster nucleation, because considerable computational requirements lead to a sharp increase in the characteristic time scale. In order to obtain information concerning the shapes of clusters and the distribution of their dimensions in the initial stage of the 2D growth, we used the kinetic Monte Carlo calculations [13] and developed a model of the formation of 3D nuclei of SiC on silicon. The model parameters were verified by comparing the results of Monte Carlo calculations to the available experimental data.

The growth of SiC nanoclusters and the evolution of their dimensions and shapes were studied using the method of kinetic equations [2, 14]. Within the framework of this analysis, we developed a physical model describing the growth of pyramids observed in experiment (Fig. 1) and their conversion into a SiC layer composed of cylinders or parallelepipeds (modeling a polycrystalline epilayer). Collisions between C adatoms deposited in the course of epitaxy and migrating over the surface of silicon lead to the nucleation of SiC nanoclusters [14]. Colliding with the existing clusters, C adatoms are attached to them, which accounts for the lateral growth. Mechanical stresses in the substrate plane increase with the cluster size [15–17], which leads to a decrease in the energy barrier for the migration of Si and C atoms from the periphery to the top of a cluster. The resulting atomic flow forms and completes the upper layers of the cluster. The need for silicon atoms in the uppermost layer is satisfied at the expense of their flow from a subsurface region, which results in the formation of cavities in the substrate [18, 19]. The proposed model is verified using available experimental data by comparison between the theoretical and experimental distributions of clusters with respect to the lateral size and height.

Thus, we have used a combination of experimental and theoretical methods to study the growth of silicon carbide nanoclusters and epilayers in the course of MBE on silicon substrates. The first results concerning the initial stages of this growth have been obtained.

Acknowledgments. This study was supported in part by the Russian Foundation for Basic Research (project nos. 02-02-17610 and 02-02-17605) and by the DAAD Project “Internationale Qualitätsnetzwerke (IQN): Ilmenauer Koordinationszentrum.”

REFERENCES

1. J. B. Casady and R. W. Johnson, Solid-State Electron. **39**, 1409 (1996).
2. V. Cimalla, J. Pezoldt, Th. Stauden, *et al.*, Phys. Status Solidi C **1**, 337 (2004).
3. V. V. Kirsanov, *Computer Experiment in Atomic Material Science* (Énergoatomizdat, Moscow, 1990).
4. D. S. Rapaport, *The Art of Molecular Dynamics Simulation* (Cambridge Univ. Press, Cambridge, 1995).
5. E. E. Zhurkin and A. S. Kolesnikov, Nucl. Instrum. Methods Phys. Res. B **202**, 269 (2003).
6. E. E. Zhurkin and A. S. Kolesnikov, Nucl. Instrum. Methods Phys. Res. B **193**, 822 (2002).
7. D. A. Terentiev and E. E. Zhurkin, Proc. SPIE **5127**, 116 (2003).
8. V. S. Kharlamov, E. E. Zhurkin, and M. Hou, Nucl. Instrum. Methods Phys. Res. B **193**, 538 (2002).
9. J. Tersoff, Phys. Rev. B **39**, 5566 (1989); **41**, 3248 (1990).
10. I. Batra, Phys. Rev. B **41**, 5048 (1990).
11. G. Brocks, P. J. Kelly, and R. Car, Phys. Rev. Lett. **66**, 1729 (1991).
12. Y. M. Mo, J. Kleiner, M. B. Webb, and M. G. Lagally, Surf. Sci. **268**, 275 (1992).
13. A. A. Schmidt, K. L. Safonov, Yu. V. Trushin, *et al.*, Phys. Status Solidi A **201**, 333 (2004).
14. K. L. Safonov, D. V. Kulikov, Yu. V. Trushin, and J. Pezoldt, Proc. SPIE **5127**, 128 (2003).
15. Yu. V. Trushin, *Theory of Radiation Processes in Metal Solid Solutions* (Nova Science, New York, 1996).
16. Yu. V. Trushin, *Radiation Processes in Multicomponent Materials: Theory and Computer Modeling* (Fiz.-Tekhn. Inst. im. A. F. Ioffe, St. Petersburg, 2002).
17. Yu. V. Trushin, K. L. Safonov, O. Ambakher, and J. Pezoldt, Pis’ma Zh. Tekh. Fiz. **29**, 11 (2003) [Tech. Phys. Lett. **29**, 663 (2003)].
18. V. Cimalla, W. Attenberger, J. K. N. Lindner, *et al.*, Mater. Sci. Forum **338**/**342**, 285 (2000).
19. V. Cimalla and J. Pezoldt, Mater. Res. Soc. Symp. Proc. **355**, 33 (1995).

Translated by P. Pozdeev

Technical Physics Letters, Vol. 30, No. 8, 2004, pp. 644–646. Translated from Pis'ma v Zhurnal Tekhnicheskoĭ Fiziki, Vol. 30, No. 15, 2004, pp. 55–61.

Lasing Wavelength of Quantum Dot Heterostructures Controlled within the 1.3–0.85 μm Range by Means of High-Temperature Annealing

E. V. Nikitina, A. E. Zhukov, A. P. Vasil'ev, E. S. Semenova, A. G. Gladyshev, N. V. Kryzhanovskaya, M. V. Maksimov, Yu. M. Shernyakov, V. M. Ustinov, and N. N. Ledentsov

Ioffe Physicotechnical Institute, Russian Academy of Sciences, St. Petersburg, 194021 Russia

Received March 15, 2004

Abstract—We have studied the effect of high-temperature annealing on the properties of a laser heterostructure with InAs quantum dots in AlAs/GaAs superlattice. By increasing the time of annealing at 700°C, it is possible to provide for a smooth variation of the lasing wavelength from 1290 to 916 nm at a constant threshold current density (250 A/cm^2 at T_0 = 110 K). By annealing the structure at 750°C, the lasing wavelength can be reduced to 845 nm. *© 2004 MAIK "Nauka/Interperiodica".*

Introduction. Lasers with quantum dots (QDs) in the active medium exhibit record low threshold currents, high differential efficiency, and high thermal stability [1]. However, the lasing wavelength of QDs in a GaAs matrix is limited from below on a level of 1.0–1.2 μm. In practice, laser QD structures obtained using various methods on GaAs substrates emit at 1.3 μm [2] and 1.5 μm [3]. However, from the standpoint of potential applications of QD lasers, it would be of importance to expand the working range of QD lasers toward shorter wavelengths.

As is known, high-temperature annealing of QD structures (either post-growth or in the course of deposition of the upper emitter layer) leads to a short-wavelength shift of the laser emission line as a result of partial mixing of the QD and matrix materials [4]. In particular, it was reported [5] that room-temperature emission at 950 nm was achieved in a laser heterostructure with InGaAs quantum dots in GaAs matrix upon annealing at 700°C. The threshold current density was about 240 A/cm^2. To the best of our knowledge, lasing at wavelengths below 900 nm was never reported in the literature.

Obviously, the short-wavelength limit of a QD laser heterostructure is determined by the bandgap width of the matrix. Therefore, materials with greater bandgap widths such as AlGaAs or Al(Ga)As/GaAs superlattices are preferred to GaAs as matrices for QD arrays. It would also be highly desirable to provide for a long-wavelength lasing in the initial (as-grown, unannealed) structure. Then, the possibility of wavelength tuning within a broad range through variation of the annealing regimen would open the way to obtaining lasers operating in various spectral regions from an epitaxial structure grown on the same wafer. Here, the key point is small variation of the threshold characteristics of QD lasers in the course of annealing.

It will be demonstrated below that annealing at 700°C weakly influences the threshold current density and the characteristic temperature of multilayer QD arrays in AlAs/GaAs superlattices. At a lasing wavelength of about 1.3 μm in the initial structure, the range of controlled variation of this wavelength exceeds 400 nm. The minimum lasing wavelength reached in our experiments was 845 nm.

Experimental. The laser heterostructures were grown on n^+-GaAs(100) substrates by molecular beam epitaxy in a Riber-32P system. Features of the epitaxial growth of InAs quantum dots are described elsewhere [6]. The room-temperature photoluminescence wavelength of these QDs is about 1.28 μm. The active region comprised five QD layers in a short-period AlAs/GaAs superlattice matrix. Emitters of the *n* and *p* type were obtained by depositing 1.3-μm-thick layers of $Al_{0.8}Ga_{0.2}As$ doped with Si and Be atoms, respectively. The substrate temperature during deposition of the laser structure did not exceed 600°C.

After epitaxial growth, the plate was cut into several parts and some of these were subjected to high-temperature annealing in a flow of arsenic in the growth chamber of the MBE setup. The annealing was performed at 700°C for various times within 1–4 h or at 750°C for 2 h.

All samples of the laser heterostructure were used to fabricate laser diodes in the geometry with four cleaved edges. The laser characteristics were studied at room temperature in the pulsed pumping regime at a frequency of 5 kHz and a pulse duration of 0.2 μs. The output signal was detected using a germanium photodiode.

1063-7850/04/3008-0644$26.00 © 2004 MAIK "Nauka/Interperiodica"

Results and discussion. Figure 1 shows the spectra of room-temperature lasing recorded 5% above the generation threshold for four-cleavage lasers fabricated from the samples annealed in various regimes. Figure 2 presents a summary of data for the dependence of the lasing wavelength on the time of annealing at 700°C and shows variation of the threshold current density.

In the initial structure, the lasing wavelength is 1290 nm at a threshold current density of 250 A/cm^2. As can be seen, annealing at 700°C for increasing times is accompanied by a gradual shift of the lasing wavelength toward shorter values. The shift is most significant after the first 1-h annealing, whereby the lasing wavelength decreases to 998 nm. Subsequently, the lasing wavelength exhibits saturation with increasing duration of annealing. The minimum lasing wavelength achieved in this series of experiments was 916 nm. The threshold current density exhibits weak growth after the first anneals but eventually again decreases to 250 A/cm^2. It should also be noted that the electrical properties of laser diodes, such as the forward voltage and resistance, remained constant during thermal treatment to within the experimental error.

Figure 3 shows the temperature dependence of the threshold current density (curves *1* and *3*) and the lasing wavelength (curves *2* and *4*) for lasers fabricated from the initial heterostructure (curves *2* and *3*) and the samples annealed for 4 h at 700°C (curves *1* and *4*). The lasing wavelength exhibits a linear increase with the temperature for both initial and annealed samples. The room-temperature threshold current density is described by a characteristic temperature of $T_0 = 110$ K. This high value is retained up to 100°C in the initial sample and up to 70°C in the sample upon the first anneal. Subsequent anneals decrease the characteristic temperature to 60 and 30 K.

The decrease in the lasing wavelength as a result of annealing is indicative of a decrease in the energy separation between electron states in the DQs and the matrix. We estimated the effective bandgap width of the obtained superlattice as 0.57 eV. Thus, the energy separation of levels decreases from 0.6 eV in the initial structure to 0.2 eV in the samples annealed at 700°C for 4 h. Such weakly localized QD arrays usually exhibit high values of the threshold current density and a strong temperature dependence of the characteristics, which is related to the thermal injection of charge carriers into the matrix [7].

The fact that a significant decrease in the lasing wavelength as a result of annealing in the structure studied is not accompanied by deterioration of the room-temperature threshold characteristics can be related to the presence of several DQ layers in the active region. Multilayer QD arrays allow the relative contribution of the thermal population of the matrix to be reduced as a result of the higher optical amplification. Another remarkable circumstance is the high stability of QD arrays with respect to the formation of structural

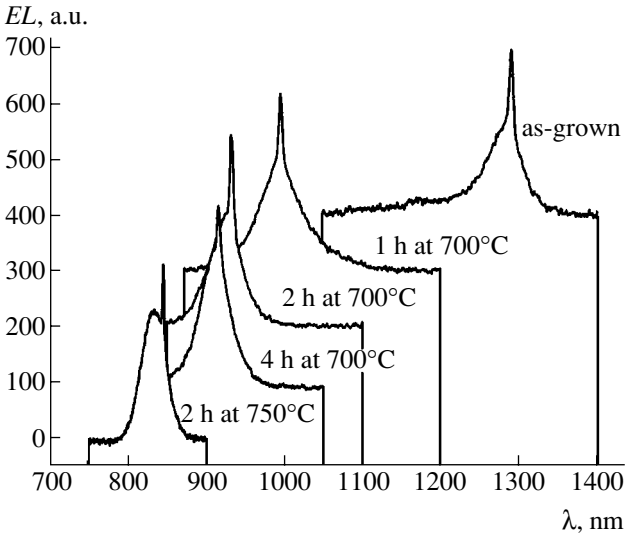

Fig. 1. Spectra of room-temperature lasing recorded 5% above the generation threshold for four-cleavage lasers fabricated from samples annealed in various regimes.

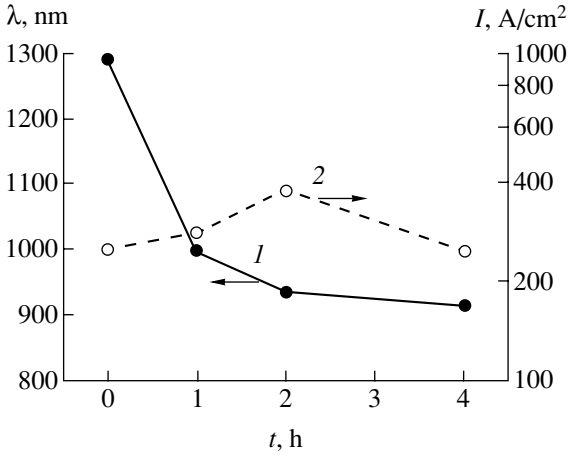

Fig. 2. Plots of (*1*) the lasing wavelength and (*2*) the threshold current density versus the time of annealing at 700°C.

defects in the course of prolonged high-temperature annealing. At the same time, a decrease in the energetic localization of QDs relative to the matrix upon annealing is manifested by a decrease in the range of high-temperature stability and in the T_0 values in the region of elevated temperatures.

Obviously, the change in the lasing wavelength depends not only on the duration of annealing, but on the annealing temperature as well. It is less evident that the effects of these factors are different. Saturation of the lasing wavelength with increasing annealing time determines the short-wavelength limit, which cannot be crossed at a given annealing temperature by further increasing the treatment duration. We can ascertain that, for the QD structure under consideration, the shortest wavelength achieved upon a very long ("infi-

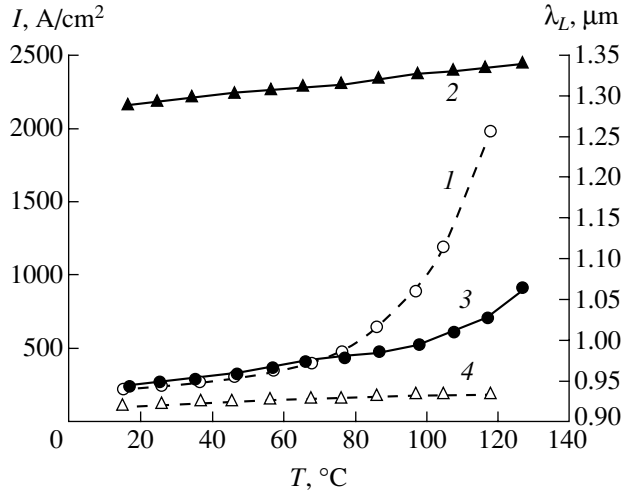

Fig. 3. The temperature dependence of (*1*, *3*) the threshold current density and (*2*, *4*) the lasing wavelength for lasers fabricated from (*2*, *3*) the initial heterostructure and (*1*, *4*) the samples annealed for 4 h at 700°C.

nite") annealing depends only on the annealing temperature.

In particular, annealing at a temperature of 600°C or below does not lead to any significant change in the lasing wavelength of the given QD array. For the structure studied, the minimum wavelength achieved by annealing at 700°C is about 0.9 μm. At the same time, an increase in the annealing temperature to 750°C allows the region of still shorter wavelengths to be reached: after a 2-h annealing at this temperature, the lasing wavelength decreased to 845 nm. However, the threshold current density of this laser increases to 750 A/cm^2, which is probably explained by a strong decrease in the energy localization of QDs relative to the matrix.

Conclusions. We demonstrated good prospects of using InAs quantum dot arrays in AlAs/GaAs matrices for obtaining lasers with working wavelengths controlled by high-temperature annealing. It was shown that, by changing the annealing regime, it is possible to reduce the lasing wavelength from 1290 to 845 nm. The annealing at 700°C is not accompanied by deterioration of the threshold characteristics of laser diodes.

Acknowledgments. This study was supported by the Russian Foundation for Basic Research, the joint project of the Ioffe Physicotechnical Institute (Russia) and Nanosemiconductor GmbH (Germany), and the Presidential Grant of the Russian Federation for Support of Young Scientists (project no. MD-4277.2004.2).

REFERENCES

1. V. M. Ustinov, A. E. Zhukov, A. Yu. Egorov, and N. A. Maleev, Quantum Dot Lasers, in *Oxford Science Publications, Series on Semiconductor Science and Technology* (Oxford Univ. Press, Oxford, 2003), Vol. 11.
2. S. S. Mikhrin, A. E. Zhukov, A. R. Kovsh, *et al.*, Fiz. Tekh. Poluprovodn. (St. Petersburg) **36**, 1400 (2002) [Semiconductors **36**, 1315 (2002)].
3. A. E. Zhukov, A. P. Vasil'ev, A. R. Kovsh, *et al.*, Fiz. Tekh. Poluprovodn. (St. Petersburg) **37**, 1461 (2003) [Semiconductors **37**, 1411 (2003)].
4. A. O. Kosogov, P. Werner, U. Gösele, *et al.*, Appl. Phys. Lett. **69**, 3072 (1996).
5. A. E. Zhukov, A. Yu. Egorov, A. R. Kovsh, *et al.*, Fiz. Tekh. Poluprovodn. (St. Petersburg) **31**, 105 (1997) [Semiconductors **31**, 84 (1997)].
6. M. V. Maximov, A. F. Tsatsul'nikov, B. V. Volovik, *et al.*, Phys. Rev. B **62**, 16671 (2000).
7. A. E. Zhukov, V. M. Ustinov, and Zh. I. Alferov, in *Selected Topics in Electronics and Systems*, Vol. 16: *Advances in Semiconductor Lasers and Applications to Optoelectronics*, Ed. by M. Dutta and M. A. Stroscio (World Scientific, Singapore, 2000), pp. 263–292.

Translated by P. Pozdeev

Technical Physics Letters, Vol. 30, No. 8, 2004, pp. 647–649. Translated from Pis'ma v Zhurnal Tekhnicheskoĭ Fiziki, Vol. 30, No. 15, 2004, pp. 62–68.

Analysis of Transient Processes in a Radiophysical Flow System

E. N. Egorov*, A. A. Koronovskiĭ, and A. E. Hramov

State Scientific Center "College," Saratov State University, Saratov, Russia

** e-mail: Egorov@cas.ssu.runnet.ru*

Received February 19, 2004

Abstract—Transient processes in a third-order radiophysical flow system are studied and a map of the transient process duration versus initial conditions is constructed and analyzed. The results are compared to the arrangement of submanifolds of the stable and unstable cycles in the Poincaré section of the system studied. © *2004 MAIK "Nauka/Interperiodica".*

In most investigations devoted to various dynamical systems, the effort is concentrated on the established regimes, while the transient processes preceding the attainment of a certain stable state receive much less attention. However, the knowledge about the behavior of the imaging point before attaining the attractor, the duration of this transient process, and the dependence of the transient time on the control parameters provides a deeper insight into various phenomena observed in the system (such as, e.g., transient chaos—a phenomenon representing essentially the transient process [1–3] of a special kind). Previously, we studied in much detail the transient processes in discrete maps [4–6].

This study addresses transient processes in a model system with continuous time and considers the dependence of the character of these processes on the regime of oscillations and on the arrangement of the manifolds of saddle cycles in the phase space.

The model system is a two-circuit radiophysical autooscillator described by the following system of equations [7]:

$$\frac{dx}{d\tau} = \frac{(\alpha - 1) f(x) - z}{\gamma},$$
$$\frac{dy}{d\tau} = -\frac{\alpha f(x)}{\gamma}, \qquad (1)$$
$$\frac{dz}{d\tau} = \gamma(x + y),$$

where α and γ are the control parameters and $f(x)$ is a dimensionless function determining the current–voltage characteristic of the nonlinear element of the system under consideration. This characteristic has the form

$$f(x) = -\frac{1}{2}x + \frac{3}{4}(|x + 1| - |x - 1|), \qquad (2)$$

representing a three-segment piecewise linear function. System (1) has been studied in sufficient detail [8–11] and, despite simple circuitry and the form of the characteristic function (2), admits complex periodic, quasiperiodic, and chaotic oscillations in the absence of external action [8]. We will consider the set of control parameters for which the system exhibits multistability [9, 10]: when $\alpha = 1.5$ and $\gamma = 3.0$, the system features oscillations with periods 7, 8, or 15, depending on the initial conditions.

A map of the transient process duration versus the initial conditions was constructed in the Poincaré section of the phase space by the $z = 0$ plane. Since the Poincaré section reduces the n-dimensional flow system to an $(n - 1)$-dimensional system with discrete time [12], the transient process duration can be determined using the method developed for maps [4, 5]. According to this, the phase trajectory with a length of several iterations is calculated for all values of the initial conditions (x_0, y_0) by the fourth-order Runge–Kutta method with a step of 0.005. This procedure determines a certain sequence of the points of intersection of the phase trajectory with the plane of the Poincaré section. It was suggested a priori that, upon this (sufficiently large) number of iterations, the transient process is completed. Then, the obtained sequence of the intersection points is checked for coincidence of the coordinates of these points to within a preset accuracy. If this verification does not reveal points with coinciding coordinates, a longer transient process is selected and the procedure is repeated until a regime attained by the system is found.[1] The period of a cycle attained by the imaging point is determined by the number of points in the Poincaré section between two points with coinciding coordinates, while the number of iterations accomplished by this moment multiplied by the time step

[1] Algorithm for determining the transient process duration in a chaotic regime is described in [5, 6].

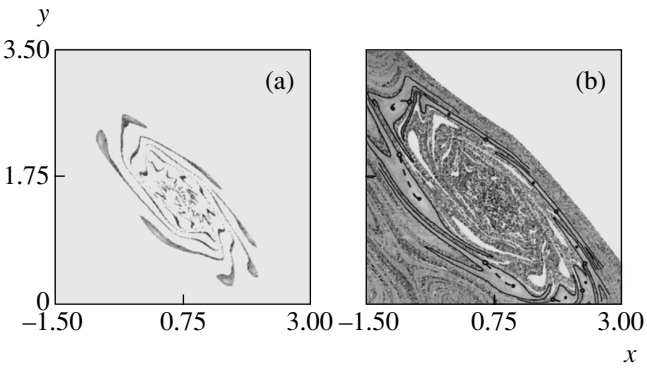

Fig. 1. Gray gradation maps of the transient process duration versus initial conditions for the cycles of periods (a) 7 and (b) 8. Bright regions correspond to shorter transient processes, while dark regions represent longer transients. In panel (b), solid and dashed lines indicate stable and unstable manifolds of the saddle cycle 1 : 8, respectively (not all of the unstable manifolds are depicted). Black and bright points correspond to stable and unstable saddle cycles, respectively. Region *1* corresponds to the initial conditions from which the imaging point goes to infinity.

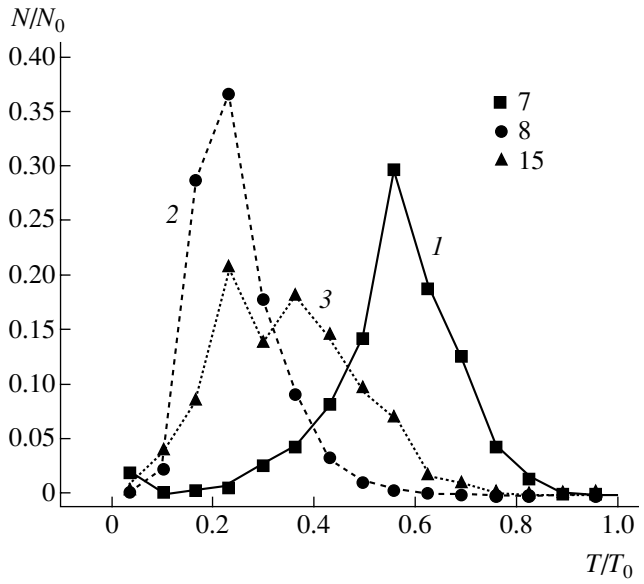

Fig. 2. Normalized distributions of the initial points in the basins of attraction with respect to the transient process duration for various cycles. The values in the abscissa axis are normalized to the maximum transient process duration (T_0) for the given cycle; the ordinates are normalized to the total number of points (N_0) in the given basin of attraction: (*1*) cycle 1 : 7 (T_0 = 1519, N_0 = 36339); (*2*) cycle 1 : 8 (T_0 = 3130, N_0 = 420900); (*3*) cycle 2 : 15 (T_0 = 3681, N_0 = 72198).

gives the transient process duration. Differences in the transient process duration are mapped in terms of the gray gradation scale.

Figures 1a and 1b present maps of the transient process duration versus initial conditions for the cycles of period 7 and 8, respectively. As can be seen, these maps exhibit more and less intensely colored regions. Dark regions are situated at the boundaries of shaded areas, while bright regions are situated inside these areas. Shorter transient processes correspond to bright regions, while longer transients are mapped by the dark regions.

We also determined which transient process durations (longer or shorter) dominate for a given set of control parameters in each oscillation regime. For this purpose, we constructed the distribution of initial conditions (x_0, y_0) occurring in the Poincaré section (N) over the intervals of transient process durations (ΔT). To determine this, we select a certain interval [T, $T + \Delta T$] and count the number of initial conditions in the basin of attraction in the Poincaré section for which the transient process durations fall within the selected interval. The corresponding normalized distributions are presented in Fig. 2, where values in the abscissa axis are normalized to the maximum transient process duration (T_0) and those in the ordinate axis are normalized to the total number of points (N_0) in the given basin of attraction. With this normalization, the area under a curve is equal to unity.

As can be seen from Fig. 2, the peaks of distributions for the cycles of periods 8 and 15 are shifted toward relatively shorter transient process durations (for each of these cycles, the transient process durations vary within a more or less broad range). This shift agrees with the data for 1 : 8 cycle in Fig. 1b, where the darkest regions (corresponding to maximum transient process durations) occupy the minimum area. Such behavior is related to the arrangement of stable manifolds of the unstable (saddle) cycles forming the boundaries of the basins of attraction of the corresponding attractors. Proximity of the peak of distribution for the cycle of period 1 : 7 to the middle of the interval of transient process durations can be explained by the relatively small size of the basin of attraction for this cycle in comparison to the basins of attraction for the other cycles (the total number of points for which this distribution was constructed is 36000; the corresponding number of points for the 1 : 8 cycle is greater by a factor of ten, while the number of points for the 2 : 15 cycle is greater by a factor of two). The main part of the basin of attraction for the 1 : 7 cycle occurs in a region distant from the attracting cycle. This implies that imaging points with the initial conditions distant from the limit cycle spend a rather long time for attaining the attracting cycle.

Another peculiarity observed in Fig. 2 is the presence of two humps in the distribution of initial conditions for the 2 : 15 cycle. This pattern can also be related to certain features in the structure of the given basin of attraction, which is significantly scattered over the entire Poincaré section. Another possible reason for this irregularity could be insufficient statistics, but the results of calculations of the maps of transient process durations with a fourfold difference in the numbers of

initial conditions showed no qualitative changes in the shape of distribution. Therefore, we can ascertain that the observed distribution shape is inherent in the system studied.

Figure 1b shows the arrangement of stable and unstable manifolds of the saddle limit cycle 1 : 8 in the Poincaré section. Near the immobile point, the manifold represents a straight segment coinciding with the eigenvector of the monodromy matrix [13]. Arbitrarily selecting a certain number of points in the vicinity of this manifold and tracing their evolution, it is possible to determine the arrangement of manifolds (more rigorous methods for determining this arrangement are described in [14]). Stable and unstable manifolds are indicated by solid and dashed lines, respectively. Intersections of the unstable saddle cycle and the Poincaré section are indicated by bright points, and intersections of the stable cycle and the $z = 0$ plane are indicated by black points. As can be seen from this figure, the darkest regions of the map coincide with stable manifolds of the saddle cycle. These very regions correspond to the maximum transient process durations. This is related to the fact that the motion of an imaging point over such a manifold takes a long time, because the velocity of this motion tends to zero as the point approaches the manifold (in this case, of the saddle cycle). At the same time, the lines of stable manifolds are directed from the regions corresponding to long transient times to the regions of shorter times surrounding the points of intersection of the stable cycle and the Poincaré section. Here, the stable manifold connects the stable and unstable saddle cycles. However close the imaging point is to the unstable cycle or its stable manifold, it will quite rapidly come to the stable cycle. This means that there is only a small number of imaging points starting from the initial conditions situated in the nearest vicinity of the stable manifold and performing actually long transients. This conclusion is confirmed by the fact that shorter transients are predominating in the distribution of the transient process durations (Fig. 2).

To summarize, we have studied transient processes in a third-order radiophysical flow system (an autooscillator of the Chua type), constructed a detailed map of the transient process durations in the plane of the Poincaré section in the region of control parameters corresponding to multistability, and determined distribution of the initial conditions with respect to the transient process duration. Analysis of these maps and distributions revealed important peculiarities in the behavior of transient processes in the basins of attraction of various cycles.

Acknowledgments. This study was supported by the Russian Foundation for Basic Research (project no. 02-02-16351), the program "Universities of Russia: Basic Research" (project UR.01.01.065), the Program of Support for Leading Scientific Schools, and the Federal Program "Integration."

REFERENCES

1. I. M. Janosi and T. Tel, Phys. Rev. E **49**, 2756 (1994).
2. Liqiang Zhu, Arving Raghu, and Ying-Cheng Lai, Phys. Rev. Lett. **86**, 4017 (2001).
3. C. Grebogi, E. Ott, and J. A. Yorke, Phys. Rev. Lett. **50**, 935 (1983).
4. A. A. Koronovskiĭ, D. I. Trubetskov, A. E. Hramov, and A. E. Khramova, Dokl. Akad. Nauk **383**, 322 (2002) [Dokl. Phys. **47**, 181 (2002)].
5. A. A. Koronovskiĭ, A. V. Starodubov, and A. E. Hramov, Izv. Vyssh. Uchebn. Zaved. Prikl. Nelineĭnaya Din. **10** (5), 25 (2002).
6. A. A. Koronovskiĭ, A. V. Starodubov, and A. E. Hramov, Pis'ma Zh. Tekh. Fiz. **29** (8), 32 (2003) [Tech. Phys. Lett. **29**, 323 (2003)].
7. T. Matsumoto, L. O. Chua, and R. Tokunaga, IEEE Trans. Circuits Syst. **34**, 240 (1987).
8. A. A. Kipchatov and A. A. Koronovskiĭ, Izv. Vyssh. Uchebn. Zaved. Prikl. Nelineĭnaya Din. **5** (2–3), 17 (1997).
9. A. V. Andrushkevich *et al.*, Izv. Vyssh. Uchebn. Zaved. Radiofiz. **38**, 1195 (1995).
10. E. N. Egorov and A. A. Koronovskiĭ, Izv. Vyssh. Uchebn. Zaved. Prikl. Nelineĭnaya Din. **10** (1–2), 104 (2002).
11. V. S. Anishchenko, in *World Scientific Series on Nonlinear Science* (World Scientific, Singapore, 1995), Ser. A, Vol. 8.
12. Yu. I. Neimark, *Method of Point Mapping in the Theory of Nonlinear Oscillations* (Nauka, Moscow, 1972).
13. N. V. Efimov, *Quadratic Forms and Matrixes* (Fizmatgiz, Moscow, 1963), pp. 126–130 [in Russian].
14. E. J. Kostelich, J. A. Yorke, and Z. You, Physica D **93**, 210 (1996).

Translated by P. Pozdeev

Technical Physics Letters, Vol. 30, No. 8, 2004, pp. 650–653. Translated from Pis'ma v Zhurnal Tekhnicheskoĭ Fiziki, Vol. 30, No. 15, 2004, pp. 69–76.

Quantum Effects Controlling Electron Beams

L. M. Baskin, V. É. Grikurov*, P. Neittaanmäki, and B. A. Plamenevskii

St. Petersburg State University, St. Petersburg, Russia

** e-mail: grikurov@math.nw.ru*

Received February 20, 2004

Abstract—Quantum effects accompanying the transport of electron beams in nanodimensional structures have been studied. The possibility of controlling the electron beam in such structures by external electric field is considered. A two-dimensional control system is proposed comprising a resonator connected to a finite number of waveguides. A method of calculation of the scattering matrix and the wave function in such structures is developed. It is possible to select the control field parameters for which the beam is reliably transferred to a preset channel. © *2004 MAIK "Nauka/Interperiodica".*

Introduction. The creation of solid state and vacuum structures on the micron and nanometer scales opens ways to the development of novel devices. Examples are offered by microwave devices with direct cold emission into the wave field [1], switching devices based on quantum wires [2], etc.

This study addresses the possibility of controlling electron beams in the domains with characteristic dimensions comparable with the electron wavelength, whereby quantum effects become predominating. It should be noted that such control systems can be created by methods of both solid state electronics and vacuum nanoelectronics.

Let us consider a two-dimensional control system comprising a resonator connected to three waveguides. One of these waveguides delivers an electron beam to the resonator, while the other two are used to shunt off the beam from the resonator. The waveguide and resonator walls represent potential barriers for electrons. Assuming the electron energies to be sufficiently small, we can ignore the effects of secondary emission [3]. A variable potential is applied to control electrodes situated at the outer boundaries of the resonator. Small dimensions (10–100 nm) and, hence, small capacitances of the system provide for the high operation speed. This device can be used, for example, as a switch with an ultrashort operation time, an element amplifying or generating microwave signals, etc.

Description of the model. Consider a two-dimensional domain D containing a resonator (a disk of radius ρ_0) connected to three channels (waveguides) representing semi-infinite bands of the same width d (Fig. 1). Let the directions of axes of two channels (for certainty, the 2nd and 3rd) be symmetric relative to the direction of the 1st channel.

In the one-electron approximation (with neglect of the self-consistent effect of the space charge of electrons), the electron wave function $\Psi(x, y)$ obeys the Schrödinger equation[1]

$$-\Delta\Psi + U(x, y)\Psi = E\Psi. \quad (1)$$

We assume that the motion of particles is restricted to the domain D and that the wave function $\Psi(x, y)$ is zero on the boundary of this domain.

In Eq. (1), the potential $U(x, y)$ controlling the electron beam is determined by the variable potentials V_1, V_2, and V_3 applied to the resonator walls A_1, A_2, and A_3. The system is assumed to be shielded along three nonclosed contours B_1, B_2, B_3 consisting of the circular segments of radius B and the rays going to infinity along the channel walls (depicted by thick dashed lines in Fig. 1). Thus, the potential U is a solution of the Dirichlet problem for the Laplace equation in the infinite domain D_B bounded by the shields B_1, B_2, B_3 (obeying zero boundary conditions) and segments A_1, A_2, A_3 with the given potentials V_1, V_2, V_3. As is known [4], this solution exponentially decays along the channels. Therefore, an approximation for U can be taken in the form of the above solution (continued by zero along the channels) in the finite domain of D_B inside a circle of sufficiently large radius with zero boundary conditions on the arcs crossing the channels.

The scattering problem in the part D will be considered in the range of energies $\pi^2 < E < (2\pi)^2$ because (i) in the adopted system of units, the energy E of electrons moving in the channels must exceed π^2; (ii) the number of scattering channels increases for the electron energies $E > (2\pi)^2$, which makes effect in question; and (iii) this energy range for d = 1–10 nm corresponds to the typical values of particle energies within 0.01–1 eV.

[1] Lengths are measured in units of the channel width d and energies are measured in the units of $\hbar^2/(2m^*d^2)$, where m^* is the effective mass of electron.

Let a low-intensity beam of electrons be injected into the system via the first channel, as described by the wave function $\Psi_{in} = \phi(z_1)e^{-i\lambda r_1}$, where $\lambda = \sqrt{E-\pi^2}$, $\phi(z) = \cos(\pi z)/\sqrt{\lambda}$, and (r_j, z_j) $(j = 1, 2, 3)$ are the longitudinal and transverse coordinates in the jth channel (the walls correspond to $z_j = \pm 1/2$). To within the terms exponentially decaying as $r_j \longrightarrow \infty$, the scattering field has the following form:[2]

$$\Psi_{scatt} = \sum_{j=1}^{3} s_{1j} e^{i\lambda r_j}\phi(z_j), \quad \sum_{j=1}^{3} |s_{1j}|^2 = 1. \qquad (2)$$

The question is whether a combination of the energy E and the control potentials V_1, V_2, V_3 can exist such that the scattering probability will be concentrated either in the 2nd or in the 3rd channel (i.e., either $|s_{12}|^2 \approx 1$ or $|s_{13}|^2 \approx 1$). If this is possible, we can switch the electron beam between output channels by reversal of the control potentials V_1 and V_3.

Below, we describe a rather general and effective method of numerical computation of the scattering coefficients, which provides a positive answer to the above question.

Method of calculation of scattering coefficients. Consider a solution to Eq. (1) with asymptotic behavior for $r_j \longrightarrow \infty$ of the type

$$\Psi \sim \phi(z_1)e^{-i\lambda r_1} + \sum_{j=1}^{3} s_{1j} e^{i\lambda r_j}\phi(z_j). \qquad (3)$$

We are interested in determining the scattering coefficients s_{1j}. The main idea of the proposed scheme of calculations is as follows.

Let us consider a finite domain D_R, obtained from D by rejecting the parts of channels with $r_j > R$, and find a function ψ_R satisfying equation (1) inside D_R, vanishing at the boundary of this domain except for the segments $r_j = R$ and obeying the Neyman conditions in these segments

$$\left.\frac{\partial \Psi_R}{\partial r_j}\right|_{r_j = R} = i\lambda(-\delta_{1j}\phi(z_1)e^{-i\lambda R} + c_j\phi(z_j)e^{i\lambda R}) \qquad (4)$$

with some coefficients c_j (to be determined). Let us

[2] Writing the scattering field in this form, we assume that each of the three terms is nonzero only in the corresponding channel.

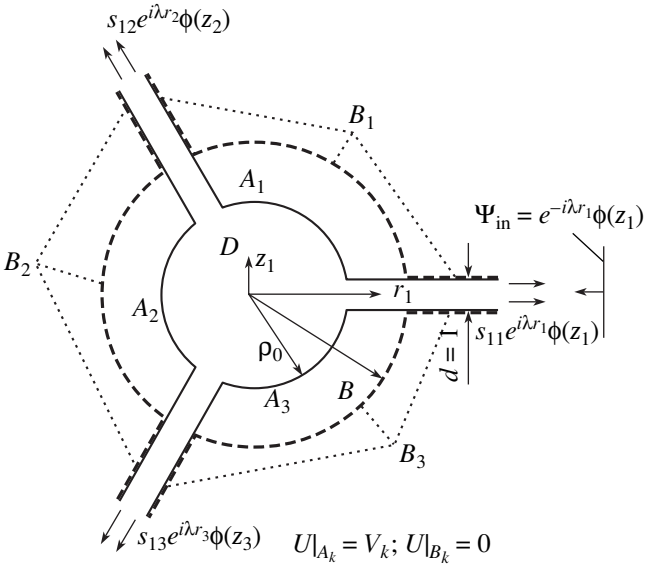

Fig. 1. Schematic diagram of the model system (see the text for explanations).

define the quantities c_j from the condition

$$\sum_{j=1}^{3}\int_{-1/2}^{1/2} \left|\Psi_R|_{r_j = R} - \delta_{1j}\phi(z_1)e^{-i\lambda R} + c_j\phi(z_j)e^{i\lambda R}\right| dz_j \mapsto \min. \qquad (5)$$

Used jointly, conditions (4) and (5) imply that relations (3) are approximately satisfied and we may hope that, provided R is sufficiently large, the quantities c_j will satisfactorily approximate the scattering coefficient s_{1j}.

Indeed, it is possible to show that

$$\sum_{j=1}^{3} |c_j - s_{1j}|^2 \underset{R\to\infty}{=} O(e^{-\gamma R}). \qquad (6)$$

This statement has been proved for a somewhat different (but more general) situation. This proof and estimation of the coefficient γ can be found in [5–7].

The functional in (5) is quadratic with respect to c_j. Calculating the coefficients of this functional at a fixed R, we can obtain the point c_j corresponding to its minimum in the form $\mathbf{c} = A^{-1}\mathbf{b}$, where

$$A_{jk} = \sum_{p=1}^{3}\int_{-1/2}^{1/2} \overline{(u_j^+|_{z_p = R} - \delta_{jp}\phi(z_p)e^{i\lambda R})} \times (u_k^+|_{z_p = R} - \delta_{kp}\phi(z_p)e^{i\lambda R})dz_p,$$
$$b_j = \sum_{p=1}^{3}\int_{-1/2}^{1/2} \overline{(u_1^-|_{z_p = R} - \delta_{1p}\phi(z_p)e^{i\lambda R})} \times (u_j^+|_{z_p = R} - \delta_{jp}\phi(z_p)e^{i\lambda R})dz_p. \qquad (7)$$

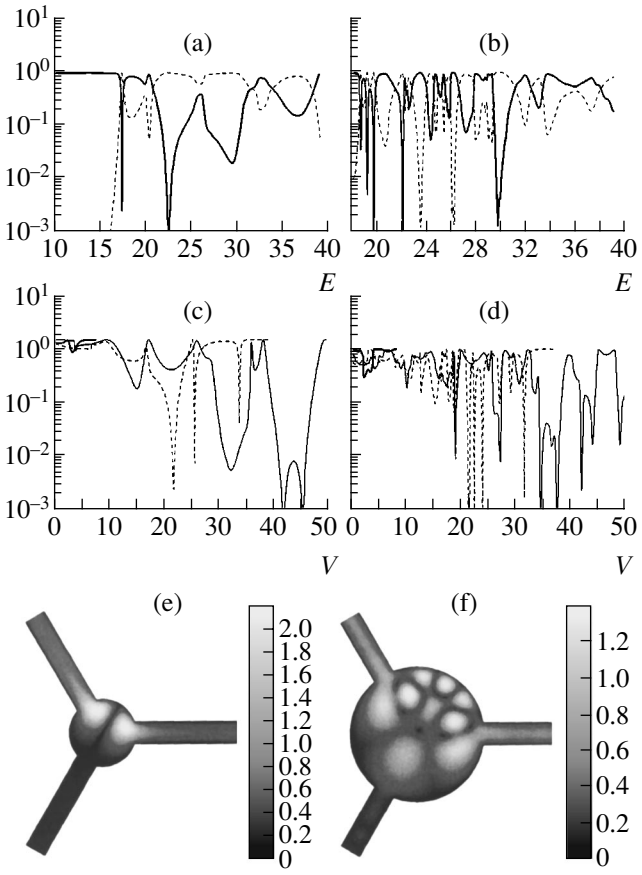

Fig. 2. The results of model calculations: (a, b) the scattering coefficients as functions of the energy E of incident electrons for the control potentials $V_1 = 0$, $V_2 = V_3 = V = (1.5\pi)^2 \sim 22.2$ and the resonator radius $\rho_0 = 1.5$ (a) and 3 (b) (solid cure shows the total losses $|s_{11}|^2 + |s_{13}|^2$, and dashed curve shows the transmission coefficient $|s_{12}|^2$); (c, d) the total losses $|s_{11}|^2 + |s_{13}|^2$ as functions of the control potential $V_2 = V_3 = V$ for $V_1 = 0$, the electron energies $E = (1.9\pi)^2$ (solid curve), $(1.5\pi)^2$ (dashed curve), and $(1.1\pi)^2$ (thick solid curve for $V \lesssim 10$), and the resonator radius $\rho_0 = 1.5$ (c) and 3 (d); (e, f) the patterns of wave function intensity $|\Psi(x, y)|^2$ for the control potentials $V_1 = 0$, $V_2 = V_3 = V = (1.5\pi)^2 \sim 22.2$ in the cases of (e) resonator radius $\rho_0 = 1.5$ and an electron energy of $E \approx 17.26$ (the first point of minimum losses in (a)) and (f) resonator radius $\rho_0 = 3$ and an electron energy of $E \approx 22.9$ (the fourth point of minimum losses in (b)).

Here, $u_j^{\pm}(x, y)$ are the functions satisfying Eq. (1) in the domain D_R, obeying the Dirichlet conditions everywhere on the boundary of D_R except for the segments $r_p = R$ (p = 1, 2, 3), and meeting the conditions $\partial u_j^{\pm}/\partial r_p|_{r_p = R} = \pm i\lambda\delta_{jp}\phi(z_p)e^{\pm i\lambda R}$ on these segments. Thus, we have reduced the calculation of the scattering coefficients to solving the partial boundary-value problems for the functions $u_j^{\pm}$. These solutions can be obtained by any appropriate numerical method. Obviously, the proposed approach is applicable for a system with any number of channels and is insensitive to the shape of the resonator.

Results of numerical analysis. Now, we will demonstrate numerical results showing the existence of combinations of the electron energy E and the control potentials V_1–V_3 for which $|s_{12}|^2 \approx 1$.

For the given numerical realization of the scheme described above, the boundary-value problems for the functions $u_j^{\pm}(x, y)$ were solved by the finite element method. The triangulation grid was selected so as to ensure calculation of the scattering coefficients with an absolute error not exceeding 0.005. Then, the probability of the total intensity of losses in the 1st and 3rd channels (i.e., the sum $|s_{11}|^2 + |s_{13}|^2$) can be considered as reliably computed if this probability is greater than $(2–5) \times 10^{-5}$.

The set of problem parameters, besides the control potentials V_1, V_2, V_3 and the energy E, includes the angles between channel axes, the resonator size ρ_0, and some other quantities. In order to reduce the number of parameters and simplify calculations, we assume that all angles between the channel axes are the same (as depicted in Fig. 1) and $V_1 = 0$. Preliminary test calculations showed that, owing to the symmetry of this system, the difference V_2–V_3 affects the final results very little, so that we can assume $V_2 = V_3 = V$.

Figure 2 shows some results of the model calculations. As can be seen, by varying one of the two parameters (E, V), it is possible to reduce the total intensity of losses to a level below 0.1%. Small losses take place when E and V are of the same order of magnitude. However, in the case of sufficiently small electron energies (see solid cures in Figs. 2c and 2d), the electron beam is virtually completely reflected. As can be seen from the comparison of Figs. 2a versus 2b and 2c versus 2d, the number of points corresponding to minimum losses increases with the resonator radius ρ_0 (this trend is more pronounced with further increase in ρ).[3]

Thus, by varying the potentials V_1, V_2, V_3 in the system under consideration, it is possible to control the electron beam so that it will be switched (with a probability close to unity) between output waveguides. Other numerical results showed that the control can be pro-

[3] One more parameter in the problem under consideration is the shielding radius B. The results presented here were obtained for $B = 6.5$; for a closer shielding, the effect of small losses is somewhat more pronounced.

vided by the field of an external electromagnetic wave as well.

REFERENCES

1. I. Brodie and C. A. Spindt, Appl. Surf. Sci. **2**, 149 (1979).
2. M. Sumetskii, J. Phys. D **3**, 2651 (1991).
3. L. N. Dobretsov and M. V. Gomoyunova, *Emission Electronics* (Nauka, Moscow, 1966) [in Russian].
4. S. A. Nazarov and B. A. Plamenevskii, *Elliptic Problems in Domains with Piecewise Smooth Boundaries* (Walter de Gruyter, Berlin, 1994).
5. V. E. Grikurov, P. Neittaanmäki, B. A. Plamenevskii, and E. Heikkola, Dokl. Akad. Nauk **385**, 465 (2002) [Dokl. Phys. Math. Sci. **66**, 136 (2002)].
6. V. E. Grikurov, E. Heikkola, P. Neittaanmäki, and B. A. Plamenevskii, Numer. Math. **94**, 269 (2003).
7. V. O. Kalvine, P. Neittaanmäki, and B. A. Plamenevskii, in *Proceedings of the 6th International Conference on Mathematical and Numerical Aspects of Wave Propagation "WAVES 2003," Springer, 2003*, pp. 469–474.

Translated by P. Pozdeev

Technical Physics Letters, Vol. 30, No. 8, 2004, pp. 654–656. Translated from Pis'ma v Zhurnal Tekhnicheskoĭ Fiziki, Vol. 30, No. 15, 2004, pp. 77–83.

Surface Wear Structures and Mechanisms in Zirconia-Based Ceramics

N. L. Savchenko[a] and S. N. Kul'kov[b,*]

[a] *Institute of Strength Physics and Materials Science, Siberian Division, Russian Academy of Sciences, Tomsk, 634055 Russia*

[b] *Tomsk State Polytechnical University, Tomsk, Russia*

** e-mail: kulkov@ms.tsc.ru*

Received January 22, 2004

Abstract—Correlations between the scale of surface structures formed upon high-velocity friction and the wear intensity have been studied for Y-TZP ceramics with various values of the average grain size. An increase in the sliding velocity from 4 to 11 m/s in the ceramics–steel friction couple leads to a decrease in the wear rate (caused by a change in the mechanism of wear from high-temperature adhesive wear to that in the regime of friction with boundary quasi-liquid lubricant film formation) and is accompanied by a decrease in the scale of the crack network formed on the friction surface. © *2004 MAIK "Nauka/Interperiodica".*

High mechanical properties of partly stabilized zirconia-based ceramics, related to the stress-induced martensitic transformation from a metastable tetragonal (T) to the stable monoclinic (M) phase, make such ceramics promising materials for friction units operating at high loads [1, 2]. Of special interest in this respect are yttria-stabilized tetragonal zirconia polycrystalline (Y-TZP) ceramics [3].

As is known, realization of one or another mechanism of wear during friction is closely related to structural transformations in the surface layers of materials under particular tribodeformation conditions. For this reason, analysis of the surface structures formed during friction in the ceramics subject to structural transformations is of considerable importance.

This study was devoted to the analysis of correlations between the scale of surface structures formed upon high-velocity friction and the wear intensity for Y-TZP ceramics with various values of the average grain size.

The experiments were performed on samples of two-phase Y-TZP ceramics with the composition ZrO_2—3 mol % Y_2O_3 with an average grain size varying from 0.9 to 2.9 μm, comprising (in the initial as-fired state) a mixture of equiaxial grains of the tetragonal and cubic zirconia phases. The friction tests were performed using the rod-on-disk scheme without lubricant, with a stepwise increase in the relative sliding velocity from 4 to 11.2 m/s at a loading pressure of 5 MPa. The counterbody was a disk made of cast high-speed steel. The friction path in all experiments was 1000 m. The structural and chemical transformations on the friction surface of samples were studied by methods of optical metallography, scanning electron microscopy (SEM), and electron probe microanalysis (EPMA).

The results of tests showed that, as the relative sliding velocity v increases from 4 to 11 m/s, the wear intensity (I) and the friction coefficient (f) of the studied ceramics decrease (Fig. 1a). This behavior was observed for all ceramics irrespective of the average grain size. Figure 1b shows plots of the tribological characteristics versus grain size d for Y-TZP ceramics studied. As can be seen, the wear intensity I measured at a velocity of v = 4.3 m/s grows with increasing d; at v = 11.1 m/s, the wear intensity slightly decreases with increasing grain size.

The results of SEM investigations showed that the surface of Y-TZP samples upon friction tests in the entire range of sliding velocities is covered with a network of cracks oriented along and across the sliding direction, forming a quasiperiodic pattern. As a result, the sample surface appeared to be cut by these cracks into rectangular fragments (blocks). After the tests at v = 7.7–11.1 m/s, the friction surfaces appeared relatively smooth and contained a smaller number of crashed and exfoliated regions as compared to the surfaces of samples tested at lower velocities. It should be noted that the observed crack networks appeared only during friction: the surface of the initial sample was free of cracks.

The dimensions of particles in the wear products depended on the sliding velocity. In the tests at v = 4–6 m/s, there appeared particles of two types: (i) relatively coarse fragments (with maximum size up to 70 μm) of irregular shapes and (ii) smaller particles of dimensions comparable with the ceramic grain size (1–3 μm). The tests at v = 7.7–11.1 m/s also led to the formation of two fractions of particles, but the size of

1063-7850/04/3008-0654$26.00 © 2004 MAIK "Nauka/Interperiodica"

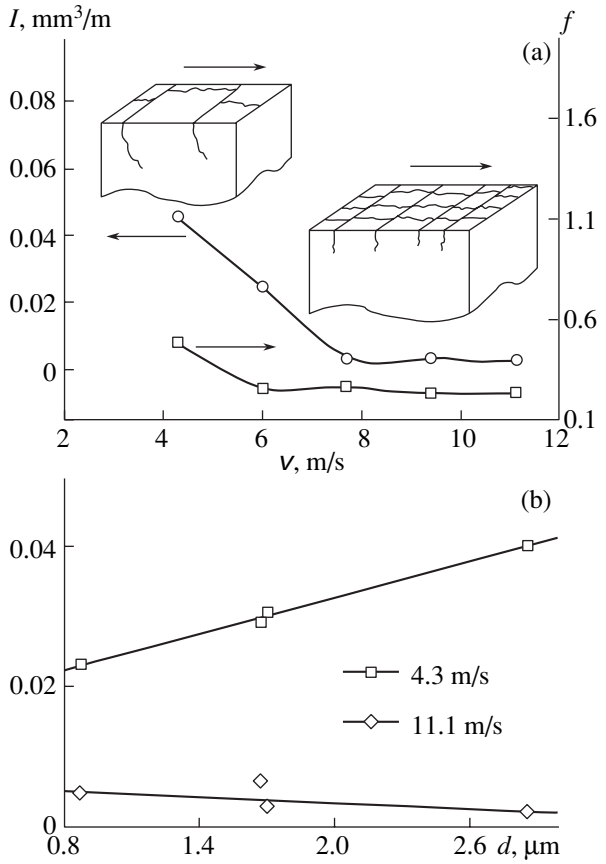

Fig. 1. Typical plots of (a) the wear intensity I and the friction coefficient f versus sliding velocity v for Y-TZP ceramics with an average grain size of 1.7 μm and (b) I versus average grain size for Y-TZP ceramics tested at lower and higher sliding velocities. The insets in (a) schematically illustrate the change in the scale of the surface crack network on the passage from high-temperature adhesive wear to that in the regime of friction with boundary quasi-liquid film formation.

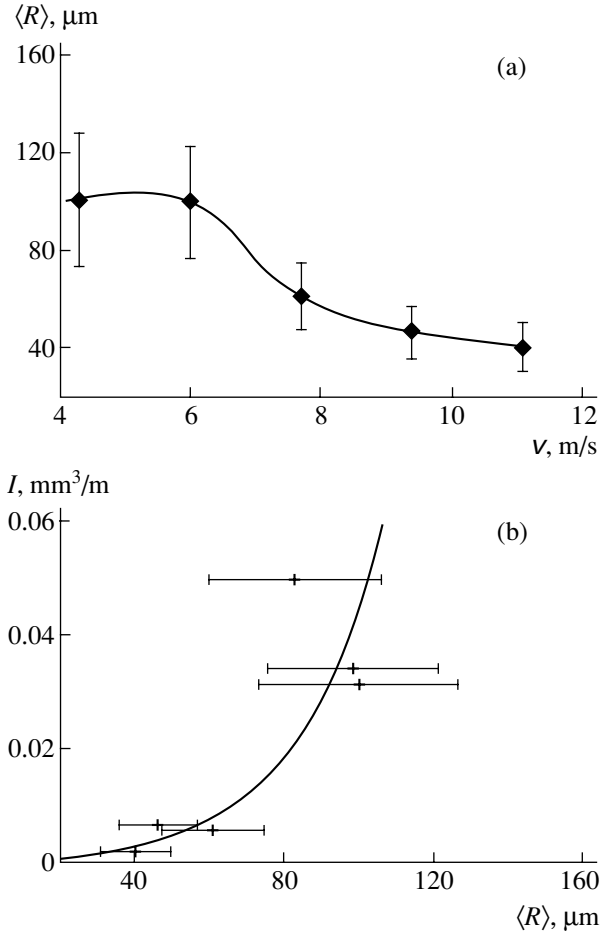

Fig. 2. The typical plots of (a) the average crack spacing $\langle R \rangle$ versus sliding velocity v for Y-TZP ceramics with an average grain size of 1.7 μm and (b) the wear intensity I versus average crack spacing $\langle R \rangle$ in the sliding direction for Y-TZP ceramics with an average grain size of 2.93 μm.

fragments in the coarse fraction (8–15 μm) was significantly smaller than that observed for the lower sliding velocities (4–6 m/s).

The results of EPMA analyses of the friction surface of ceramic samples in all cases showed the presence of a surface layer containing the material transferred during friction from the steel counterbody. SEM images showed that, in samples tested at v = 7–11 m/s, this layer covers virtually the entire friction surface of ceramics. The content of steel components both on the friction surface and in the particles of wear products increased with the sliding velocity.

Upon measuring distances between transverse cracks in the direction of sliding and constructing their distribution, we obtained the normal (Gaussian) profile with a clear maximum. This is evidence of a certain periodicity in the mutual arrangement of transverse cracks in the sliding direction. Figure 2a shows the typical plot of the distance between cracks in the sliding direction versus sliding velocity, which were observed for ceramics with various values of the average grain size. All such curves exhibit the same peculiarity: the spacing of transverse cracks at v = 7–11 m/s is smaller than at v = 4–6 m/s; moreover, the average distance between cracks was virtually independent of the average grain size.

The process of wear at v = 4–6 m/s can be interpreted in terms of the high-temperature adhesive interaction between ceramics and steel. This regime is characterized by high wear intensities and large friction coefficients, which is confirmed by data in Fig. 1a. As was pointed out previously [4, 5], a decrease in the wear intensity with increasing relative sliding velocity (Fig. 1a) can be related to a decrease in the level of contact stresses as a result of formation of the transfer layer and its transformation from solid to quasi-liquid state. This transformation is favored by high temperatures developed in the friction contact zone (estimates obtained according to [6], this region can be heated up to 1500–2000°C, which is comparable with or even

higher than the melting temperature of steel). The intense mass transfer from steel to ceramic surface leads to an increase in the amount of steel components both on the worn surface and in the particles of wear products. The aforementioned quasi-liquid film uniformly covering the friction surface on ceramic samples plays the role of a soft coat which, increasing the effective area of contact between ceramics and the counterbody, favors a decrease in the level of contact stresses on the friction surface. Under these conditions, whereby quasi-liquid film uniformly covers the surface of ceramics, the friction coefficient exhibits a minimum and approaches values typical of the regime of friction with boundary lubricant (0.15–0.20 [6, 7]).

One of the most probable factors responsible for the formation of a periodically arranged cracks are the elastic oscillations arising during sliding friction in the "sample-friction test machine" system. It was reported [8] that, at a certain relation between oscillation frequency and the level of impact on the surface layer of a tested material, such quasiperiodic cracking structures can appear in the region of tensile stresses. More evidence in favor of this mechanism is the decrease in the distance between cracks with increasing velocity (Fig. 2a). This behavior can be explained by the decrease in the spatial period of oscillations with increasing velocity (i.e., with increasing couterbody rotation frequency). In addition, high sliding velocities revealed similarity in the trends of the crack spacing variation observed for Y-TZP ceramics and a TiC–NiTi composite (with a metallic matrix), which was especially pronounced in the range of velocities above 5 m/s [4, 6]. Such a similarity in the behavior of materials with dissimilar nature and physical (mechanical) properties gives us ground to conclude that the aforementioned factor of oscillations in the "sample-friction test machine" system plays a significant role in our case.

Figure 2b shows a plot of the wear intensity versus average distance between transverse cracks in the sliding direction for Y-TZP ceramics studied. As can be seen from these data, a decrease in the intensity of wear is accompanied by a decrease in the spacing of cracks. The form of the particles of wear products indicates that wear in the entire range of sliding velocities takes place on a scale level comparable with the block size, whereby the dimensions of coarse particles decreases with increasing velocity similarly to the distance between cracks. In all likelihood, the process of wear is controlled to a considerable extent by the size of fragments (blocks) on the ceramic surface, since the strength in these regions is decreased by the boundary cracks. Removal of ceramic particles (bounded by the cracks) from the sample surface followed by their disintegration in the friction contact zone probably accounts for the two- to threefold difference between the size of particles in the wear products and the spacing of cracks observed in the ceramic surface. The depth of penetration of these cracks in depth of the sample decreases as well. The transverse sections of the samples tested in the regime of high-temperature adhesive wear exhibited cracks sloped at about 45° relative to the friction surface, penetrating to a depth of up to 25 μm. In the samples studied after friction in the regime of quasi-liquid film formation, the cracks penetrated along the normal to the friction surface and reached a depth not exceeding 13 μm.

Apparently, the appearance of small-particle fraction in the wear products observed at various sliding velocities can be related to two factors. First, such particles can be formed in the entire range of v as a result of disintegration of the fragments (blocks) bounded by cracks in the zone of friction contact. Second, based on the dependence observed in Fig. 1b (characteristic of the Hall–Petch effect), we may suggest that a certain fraction of small particles formed at v = 4–6 m/s appeared as a result of grain-boundary disintegration.

Thus, a change in the mechanism of wear in the Y-TZP–steel friction couple, taking place when the sliding velocity is increased from 4 to 11 m/s, is accompanied by a decrease in the scale of a crack network formed on the friction surface, whereby both the spacing of cracks and their penetration depth decrease as depicted in Fig. 1a.

Acknowledgments. This study was supported by the Ministry of Education of the Russian Federation (project no. 3.10-44), the U.S. Civilian Research and Development Foundation for Independent States of the Former Soviet Union (CRDF grant no. BRHE-016), and the Program of Support for Leading Scientific Schools of Russia (project no. NSh-2324.2003.1).

REFERENCES

1. S. W. Lee, S. H. Hsu, and M. C. Shen, J. Am. Ceram. Soc. **76**, 1937 (1993).
2. P. C. Becker, T. A. Libsch, and S. K. Rhee, Ceram. Eng. Sci. Proc., Nos. 7–8, 1040 (1985).
3. L. Nettleship and R. Stevens, Int. J. High Technol. Ceram., No. 3, 1 (1987).
4. N. L. Savchenko, P. V. Korolev, A. G. Mel'nikov, *et al.*, Trenie Iznos **22**, 322 (2001).
5. N. L. Savchenko, P. V. Korolev, A. G. Mel'nikov, *et al.*, Wear **249**, 892 (2002).
6. S. C. Lim and M. F. Ashby, Acta Metall. **35**, 1 (1987).
7. A. Ravikiran and B. N. Pramila Bai, J. Mater. Sci. **30**, 1999 (1995).
8. V. L. Popov and A. V. Kolubaev, Pis'ma Zh. Tekh. Fiz. **21** (19), 91 (1995) [Tech. Phys. Lett. **21**, 812 (1995)].

Translated by P. Pozdeev

Technical Physics Letters, Vol. 30, No. 8, 2004, pp. 657–659. Translated from Pis'ma v Zhurnal Tekhnicheskoĭ Fiziki, Vol. 30, No. 15, 2004, pp. 84–90.

Synthesis and Properties of Ge–$(Ge_2)_{1-x}(GaAs)_x$ ($0 \le x \le 1.0$) Epitaxial Heterostructures Grown by LPE from Lead-Based Solution Melts

B. Sapaev

Physicotechnical Institute, "Solar Physics" Research and Production Corporation, Academy of Sciences of the Republic of Uzbekistan, Tashkent, Uzbekistan

e-mail: bayram@physic.uzsci.net

Received February 25, 2004

Abstract—Epitaxial layers of wide-bandgap GaAs on germanium substrates were grown by liquid phase epitaxy from a lead-based solution melt in the temperature interval from 700 to 650°C. Depth–composition profiles of the obtained epilayers were determined. Scanning images obtained using characteristic X-ray emission show that the epilayers are structurally perfect and characterized by monotonic variation of the component concentrations both in depth and in the lateral direction, while the macroscopic defects and metal inclusions are absent. The photoluminescence spectra of solid solutions exhibit edge emission bands with the maxima at $h\nu_1$ = 1.32 eV and $h\nu_2$ = 1.43 eV. © *2004 MAIK "Nauka/Interperiodica".*

Using group IV elements and $A^{III}B^{V}$ semiconductor compounds, it is possible to obtain solid solutions with bandgap widths variable within a broad range, from values characteristic of the former elements (Ge, Si, Sn) to those typical of the latter compounds (GaAs, GaP, GaN, etc.). It was reported that limited solid solutions of the Si–GaAs and Ge–GaSb systems can be obtained by means of cathode sputtering, but the structural characteristics and physicochemical properties of such materials are still insufficiently studied [1, 2].

The synthesis of metastable continuous solid solutions of the Ga–GaAs system by pyrolysis was originally reported by Alferov *et al.* [3]. These researchers studied the dependence of the lattice parameter and bandgap width of $(Ge)_x(GaAs)_{1-x}$ solid solutions on the composition and determined the other physical properties of these materials [3, 4]. Recently, Andreev *et al.* [5] obtained Ge-based photocells using GaAs/Ge heterostructures grown by metalorganic vapor phase epitaxy (MOVPE) and doped by zinc diffusion. It was demonstrated that these photocells are characterized by increased open-circuit voltages and a high photoresponse approaching (under otherwise equal conditions) the level achieved in GaAs photocells.

Theoretical prerequisites for the synthesis of solid solutions of the $(C_2^4)_{1-x}(A^{III}B^{V})_x$ type are provided by the known conditions for their formation established using an analysis based on the method of generalized moments. According to data on the solubilities of Ge and GaAs in liquid metals, the use of lead as the solvent ensures all the necessary conditions for the formation of true solid solutions of the $(Ge_2)_{1-x}(GaAs)_x$ type [3], including a rather high supersaturation at the crystallization front with respect to both components of the solid solution. In addition, relatively low growth temperatures (700–650°C) prevent the spontaneous decomposition of solid solutions.

This paper reports on the growth and properties of $(Ge_2)_{1-x}(GaAs)_x$ epilayers grown by liquid phase epitaxy (LPE) from lead-based solution melts on germanium substrates. Since systems of the $(C_2^4)_{1-x}(A^{III}B^{V})_x$ type belong to the class of substitutional solid solutions, their formation is facilitated in the case of components possessing closer properties. In order to obtain epilayers possessing desired electrical properties, it is necessary to know the mutual solubilities of elements and study the influence of various technological factors on the growth of the target semiconductor compound. These factors include, in particular, the physical state of a solution melt contacting the substrate. The compositions of Pb–Ge–GaAs solution melts and the temperature intervals of crystal growth were determined using published data [7, 8] and the results of preliminary experiments.

Homogeneous epilayers of $(Ge_2)_{1-x}(GaAs)_x$ solid solutions were grown by the conventional LPE technique on vertical substrates [6]. The epitaxy proceeds from a large volume of intensively stirred solution melt. After termination of the growth process, the surface of the epilayer was cleaned from the residual material. The epilayers were grown on (111)0°15-oriented *p*-type single crystal germanium substrates (GDG grade) with a resistivity of 40 Ω cm, a thickness of 400 μm, and an area of about 1 cm^2. Prior to growth,

1063-7850/04/3008-0657$26.00 © 2004 MAIK "Nauka/Interperiodica"

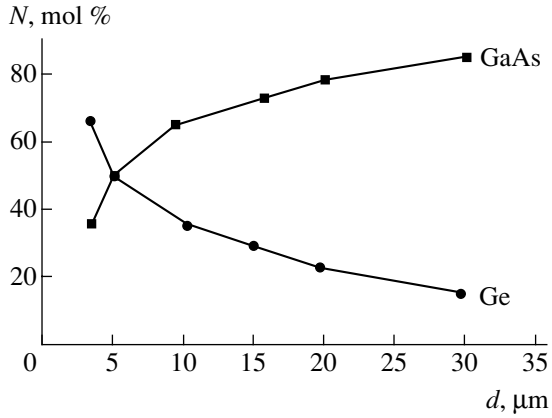

Fig. 1. The typical concentration–depth profiles of components in a $(Ge_2)_{1-x}(GaAs)_x$ film grown by LPE on germanium substrate.

the substrates were cleaned by etching in an HCl–NHO_3 mixture (*aqua regia*), repeatedly rinsed in deionized water, dried, and annealed for 1.5 h in vacuum (133×10^{-3} Pa) at 900°C. The epilayers were grown from Pb–Ge–GaAs solution melts saturated with respect to both Ge and GaAs by cooling at a rate of 0.5–2.0 K/min.

The thicknesses of the obtained $(Ge_2)_{1-x}(GaAs)_x$ films were determined by the regime of cooling and varied from 25 to 49 μm. Investigation of the effect of initial temperature and cooling rate on the film thickness and structure showed that the surface morphology of epilayers significantly depends on the these factors and the composition. This behavior is probably related to the mutual influence of the solubilities of Ge and GaAs in lead-based melts. The optimum technological regimes were determined in a special series of experiments. It was established that, when the crystallization begins at a temperature above 700°C or below 580°C and the cooling rate exceeds 1.5 K/min, the surface of epilayers is not smooth. On the other hand, decreasing the cooling rate below 0.5–0.75 K/min significantly increases the process duration and the energy consumption. Films grown for the crystallization onset temperature in the interval from 700 to 620°C and a cooling rate of 0.75–1.0 K/min exhibited a mirror smooth surface.

Analysis of the scanning images obtained using characteristic X-ray emission showed that epilayers grown under such conditions contain no macroscopic defects or metal inclusions and the solid solution components are homogeneously distributed both over the surface and in depth of the film.

Figure 1 shows the typical concentration–depth profiles in a $(Ge_2)_{1-x}(GaAs)_x$ film grown on germanium substrate. An analysis of such data leads to the following conclusions. At the onset of crystallization in the lead-based solution melt, germanium is predominantly deposited because, according to the phase diagram, the melt is saturated with this element. A decrease in the temperature creates thermodynamic conditions for the growth of a $(Ge_2)_{1-x}(GaAs)_x$ layer because the melt is supersaturated with respect to both components of the solid solution.

After termination of the growth process, the surface of the epilayer was cleaned from the residual material with the aid of a special device. According to data on the elemental depth profiles obtained using a Cameca microanalyzer, the content of GaAs increases along the growth axis and reaches 100% on the surface (Fig. 1). It was found that the structure of $(Ge_2)_{1-x}(GaAs)_x$ solid solutions is more perfect in the epilayers grown on Ge(111) substrates. This is confirmed by the study of morphology of the epilayers with a dislocation density of 3×10^4 cm^{-2}. According to scanning images obtained using characteristic X-ray emission (AsK_α, GaK_α, GeK_α), the epilayers are structurally perfect and characterized by quite monotonic variation of the component concentrations over the sample surface (Fig. 2).

The mobility of charge carriers in the epilayers of $(Ge_2)_{1-x}(GaAs)_x$ solid solutions was studied in the temperature interval T = 90–300 K using the samples with fused In–Zn alloy ohmic contacts. The measurements showed that the films with mirror smooth surfaces had a *p*-type conductivity with a charge carrier density of 1.4×10^{18} cm^{-3} and a mobility of 155 cm^2/(V s) at 300 K. An analysis of the temperature dependence of the carrier mobility in $(Ge_2)_{1-x}(GaAs)_x$ epilayers (Fig. 3) shows that this curve is described by the formula $\mu = AT^{-3/2}$.

Figure 4 shows the photoluminescence spectrum of a Ge–$(Ge_2)_{1-x}(GaAs)_x$ heterostructure excited by an

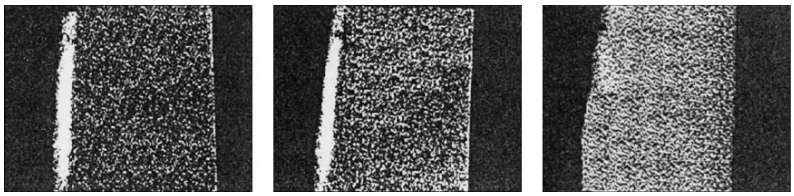

Fig. 2. Scanning images of the epilayer cross sections measured using characteristic X-ray emission (AsK_α, GaK_α, GeK_α).

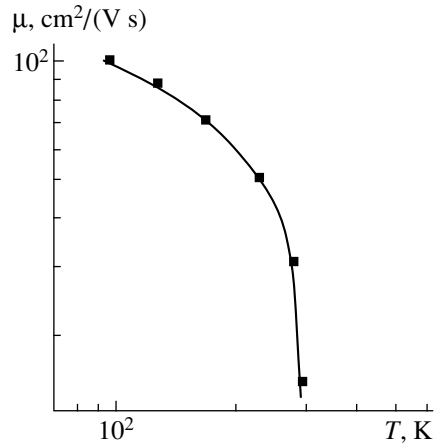

Fig. 3. The temperature dependence of the carrier mobility in $(Ge_2)_{1-x}(GaAs)_x$ epilayers measured in the temperature interval T = 90–300 K.

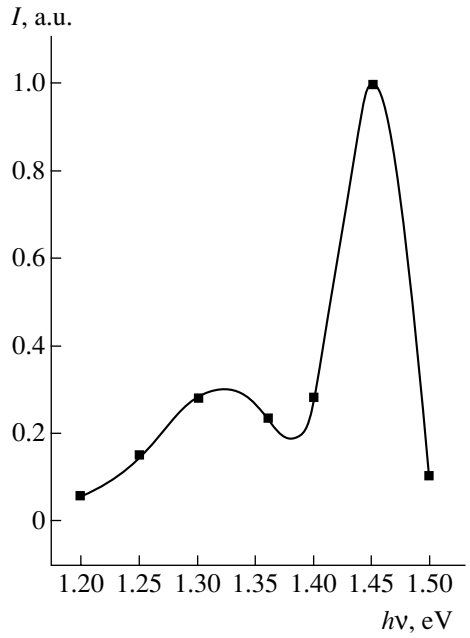

Fig. 4. The typical photoluminescence spectrum of a Ge–GaAs heterostructure measured at liquid nitrogen temperature.

LG-75 laser was recorded using a PbS detector and a FEU-62 photomultiplier. As can be seen, the spectrum displays two edge emission bands with the maxima at $h\nu_1$ = 1.32 eV and $h\nu_2$ = 1.43 eV. The latter peak is related to the edge emission from the $(Ge_2)_{1-x}(GaAs)_x$ solid solutions, while the former peak is probably due to a radiative recombination center in the forbidden band.

To summarize, it is possible to obtain structurally perfect variband layers of $(Ge_2)_{1-x}(GaAs)_x$ solid solutions on germanium substrates by LPE from a lead-based solution melt. These layers can be used in semiconductor microelectronics. Epitaxial Ge–$(Ge_2)_{1-x}(GaAs)_x$ ($0 \le x \le 1.0$) heterostructures can find application in solar cells for effective energy conversion in the IR spectral range.

REFERENCES

1. A. J. Noreika and M. H. Francole, Appl. Phys. **45**, 3690 (1974).
2. K. G. Gadien, J. L. Zilko, A. H. Eltonkky, and I. E. Greene, J. Vac. Sci. Technol. **17**, 441 (1980).
3. Zh. I. Alferov, M. Z. Zhingarev, S. G. Konnikov, *et al.*, Fiz. Tekh. Poluprovodn. (Leningrad) **16**, 831 (1982) [Sov. Phys. Semicond. **16**, 532 (1982)].
4. Zh. I. Alferov, R. S. Vartanyan, V. I. Korol'kov, *et al.*, Fiz. Tekh. Poluprovodn. (Leningrad) **16**, 887 (1982) [Sov. Phys. Semicond. **16**, 567 (1982)].
5. V. M. Andreev, V. P. Khvostikov, N. A. Kalyuzhnyi, *et al.*, Fiz. Tekh. Poluprovodn. (St. Petersburg) **38**, 369 (2004) [Semiconductors **38**, 355 (2004)].
6. M. S. Saidov, A. S. Saidov, V. V. Nikitin, and G. N. Kovardakova, USSR Inventor's Certificate No. 2076160 (1977).
7. V. M. Andreev, L. M. Dolginov, and D. N. Tret'yakov, *Liquid-Phase Epitaxy in Technology of Semiconductor Devices* (Sov. Radio, Moscow, 1975) [in Russian].
8. M. Hansen and K. Anderko, *Constitution of Binary Alloys* (McGraw-Hill, New York, 1958; Metallurgizdat, Moscow, 1962).

Translated by P. Pozdeev

Technical Physics Letters, Vol. 30, No. 8, 2004, pp. 660–662. Translated from Pis'ma v Zhurnal Tekhnicheskoĭ Fiziki, Vol. 30, No. 15, 2004, pp. 91–95.

Electron Beam Induced Explosive Luminescence of PETN

B. P. Aduev, G. M. Belokurov, S. S. Grechin, and E. V. Tupitsin

Kemerovo State University, Kemerovo, Russia

Institute of Solid State Chemistry and Mechanochemistry (Kemerovo Department), Siberian Division, Russian Academy of Sciences, Kemerovo, Russia

e-mail: lira@kemsu.ru; filial@kemnet.ru

Received March 4, 2004

Abstract—We have studied the spectrum and kinetics of optical emission in the wavelength range from 550 to 1000 nm accompanying explosive decomposition of pentaerythritol tetranitrate (PETN) single crystals initiated by a nanosecond electron beam. The explosive luminescence kinetics reveals two components with a continuous spectrum, identified as luminescence accompanying the explosive decomposition, and a component with a linear spectrum due to molecular nitrogen formed as a result of explosion. © *2004 MAIK "Nauka/Interperiodica".*

Use of high-current pulsed electron beams and high-power laser pulses in combination with electrical and optical measurements at a high time resolution provided a large body of experimental data on the physicochemical processes involved in the explosive decomposition of heavy metal azides belonging to the class of initiators [1–3]. To our knowledge, no analogous experiments were reported for high explosives such as pentaerythritol tetranitrate (PETN).

High explosives are characterized by relatively higher initiation thresholds as compared to those typical of initiators, which implies higher requirements to the power of excitation sources. For example, the action of laser pulses on the free surface of PETN does not initiate explosion even at maximum output power levels [4]. Recently, Korepanov *et al.* [5] succeeded in electron beam initiation of PETN samples pressed at 10^9 Pa from disperse powder with a surface area of S = 600 m^2/kg. The pulsed electron beam had an average electron energy of 250 keV, a pulse duration of ~25 ns, and a power density of $P > 4 \times 10^9$ W/cm^2. The experimental methods used in [5] allowed the kinetics of explosive luminescence to be measured but did not provide spectral information.

In our study, PETN samples were initiated by a pulsed electron beam with the parameters analogous to those used in [5]. The spectrum and kinetics of explosive (detonation) luminescence were measured using a setup including a polychromator and a photochronograph based on an electrooptical converter. Using this setup, it was possible to measure the optical emission spectrum in the wavelength range from 550 to 1000 nm during explosion of a single sample. the measurements were performed at a time resolution of 20 ns limited by the electron beam pulse duration.

The experiments were performed with $3 \times 2 \times 1$-mm PETN single crystals. The samples were initiated in a vacuum chamber at a residual gas pressure of 10^{-2} Pa and a temperature of 300 K. Each sample was glued with its side to a wire fixed on the chamber wall. The irradiated surface was oriented at 45° relative to the electron beam axis and the optical axis of the measuring setup. The results of measurements showed that the luminescence spectrum is continuous and the emission kinetics consists of two components: a relatively short initial peak followed by a longer emission.

In the presence of an obstacle (a transparent film) in front of a sample, the luminescence with a continuous spectrum is followed by emission with a line spectrum. The same phenomenon is observed for a sample glued with its rear side to a massive metal substrate.

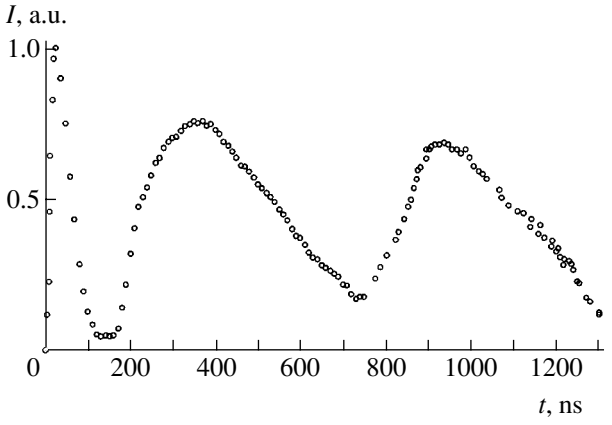

Fig. 1. Typical kinetics of the explosive luminescence from PETN single crystals measured at λ = 770 nm. The first two components have continuous spectra, while the third component exhibits a line spectrum.

1063-7850/04/3008-0660$26.00 © 2004 MAIK "Nauka/Interperiodica"

Figure 1 shows the kinetics of explosive luminescence from a PETN sample fixed on a massive substrate, measured at $\lambda = 770$ nm (coinciding with one of the spectral lines). Here, the leading front width of the first peak corresponds to the electron beam pulse duration. It should be noted that only this first peak is observed if the electron beam energy is below the initiation threshold.

Figure 2 shows the luminescence spectra (with allowance of the spectral sensitivity of the measuring setup) measured at the moments of time corresponding to the maxima of emission components in Fig. 1. Apparently, the line spectrum (Fig. 2, curve *3*) is due to the emission from products formed as a result of the explosion. These products rapidly expand to leave the region viewed by the measuring setup and can be observed only in the presence of a mechanical obstacle (transparent film or a metal substrate). The observed lines can be related to the emission from nitrogen molecules [6].

Interpretation of the emission components with continuous spectra encounters considerable difficulties. Apparently, this emission can be related to the luminescence from a PETN crystal accompanying the explosive decomposition reaction.

The first question to be answered is whether this emission represents thermoluminescence caused by the sample heating in the course of the explosive decomposition reaction. The results of our measurements show that the spectra of the first and second components of the emission kinetics coincide (see Fig. 2, curves *1* and *2*), which is evidence of the identical nature of these components.

If the emission were of a thermal nature, then, taking into account the duration of the first peak, it would be necessary to conclude that the sample is heated to a high temperature during the excitation pulse and then cools during a time period shorter than 10^{-7} s. This process is hardly possible, since thermal conduction during the sample heating by a high-power electron beam pulse with duration 10^{-7}–10^{-6} s can be ignored: this process really takes 10^{-5}–10^{-4} s [7].

Therefore, the first emission peak with continuous spectrum can be interpreted as electron-beam-induced luminescence caused by the excitation pulse.

In addition, if the emission were thermal, it would be possible to use the Wien displacement law and evaluate the radiation temperature from the position of the spectral maximum. In our case, $\lambda_{max} = 850$ nm (Fig. 2), which corresponds to $T = 3440$ K. Using the Planck formula, we may calculate the corresponding blackbody radiation spectrum (Fig. 2, curve *4*). As can be seen from Fig. 2, the experimental spectrum is not approximated by the Planck radiator spectrum.

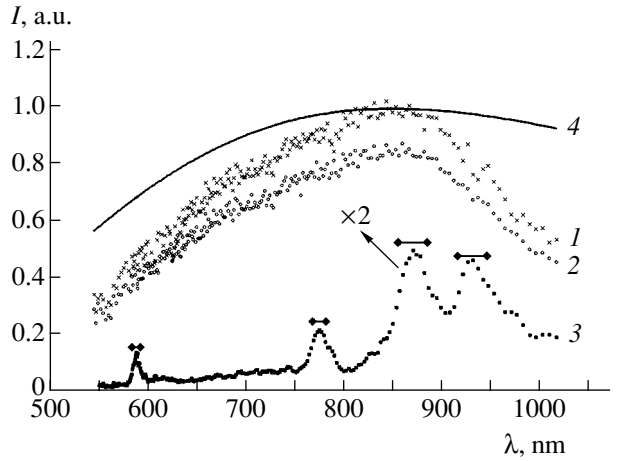

Fig. 2. The spectra of explosive luminescence of PETN single crystals measured at various moments of time after the initiation pulse front (ns): (*1*) 20; (*2*) 350; (*3*) 930. Curve *4* is the calculated radiation spectrum of blackbody at $T = 3440$ K.

Moreover, according to the estimates obtained in [5], the sample temperature at the moment of termination of the excitation pulse is ~1100 K. If this estimation is correct, the thermal emission spectrum would be shifted toward the IR range to fall out of the sensitivity range of the experimental equipment.

Thus, the entire combination of experimental facts leads to the unambiguous conclusion that the observed explosive emission should be interpreted as luminescence from PETN crystals in the course of development of the explosive decomposition reaction. It should be noted that we also carried out experiments with pressed PETN samples analogous to those studied in [5]. The results were qualitatively the same as those reported above for single crystals.

We may ascertain that the kinetics of luminescence from electron-beam-initiated PETN crystals reflects that of the reaction of their explosive decomposition. Elucidation of the mechanism of this reaction and the nature of related emission requires additional investigations. However, the similarity of the spectral and kinetic characteristics of the explosive decomposition of heavy metal azides [1–3] and PETN suggests that the initial stage of this reaction in PETN proceeds according to the chain mechanism. An analogous approach is theoretically developed in [8], where an exciton mechanism of the chain decomposition reaction of high explosives is proposed and numerical calculations for explosives of the RDX type are performed.

REFERENCES

1. B. P. Aduev, E. D. Aluker, G. M. Belokurov, *et al.*, Zh. Éksp. Teor. Fiz. **116**, 1676 (1999) [JETP **89**, 906 (1999)].

2. M. M. Kuklja, B. P. Aduev, E. D. Aluker, *et al.*, J. Appl. Phys. **89**, 4156 (2000).

3. B. P. Aduev, E. D. Aluker, G. M. Belokurov, *et al.*, in *Pre-Denotation Phenomena in Heavy Metal Azides* (TsÉI Khimmash, Moscow, 2002) [in Russian].

4. A. A. Brish, I. A. Galleev, and B. P. Zaĭtsev, Fiz. Goreniya Vzryva **2**, 132 (1966).

5. V. I. Korepanov, V. M. Lisitsyn, V. I. Oleshko, *et al.*, Pis'ma Zh. Tekh. Fiz. **29** (16), 23 (2003) [Tech. Phys. Lett. **29**, 669 (2003)].

6. R. W. B. Pearse and A. G. Gaydon, *The Identification of Molecular Spectra* (Chapman and Hall, London, 1941; Inostrannaya Literatura, Moscow, 1949).

7. G. A. Bleikher, V. P. Krivobokov, and O. V. Pashchenko, *Heat–Mass Transport in Solids under the Action of High-Power Charged Particle Beams* (Nauka, Novosibirsk, 1991).

8. M. M. Kuklja, E. V. Stefanovich, and A. B. Kunz, J. Chem. Phys. **112**, 3417 (2000).

Translated by P. Pozdeev

Technical Physics Letters, Vol. 30, No. 8, 2004, pp. 663–665. Translated from Pis'ma v Zhurnal Tekhnicheskoĭ Fiziki, Vol. 30, No. 16, 2004, pp. 1–6.

Polymer-Based Nanocomposites for Bolometric Applications

A. E. Varfolomeev*, A. V. Volkov, D. F. Zaretskiĭ, M. A. Moskvina, and V. Z. Mordkovich

Kurchatov Institute, Russian State Scientific Center, Moscow, 123182 Russia

** e-mail: varfol@imp.kiae.ru*

Received February 17, 2004

Abstract—We have studied the temperature dependences and kinetics of conductivity and the current–voltage characteristics of highly filled polymer-based nanocomposites containing CdS particles with an average size of about 50 Å. The conductivity activation energy, electron density, and electron mobility were determined. The temperature coefficient of resistance of the nanocomposites at room temperature reaches 0.15 K^{-1}. Polymer-based film nanocomposites with semiconductor particles are promising media for highly responsive temperature sensors, in particular, bolometers. © *2004 MAIK "Nauka/Interperiodica".*

Introduction. Polymer-based film nanocomposites containing semiconductor particles may possess unique physical characteristics, combining the properties of semiconductors and polymer films, while the presence of nanoparticles in a polymer matrix may lead to basically new effects. Such polymeric nanocomposites have been studied as new optical and electrophotographic media with improved characteristic [1]. We have synthesized nanocomposites with CdS semiconductor particles whose concentration can be varied in a broad range. In this system, it is possible to study the electrical properties and the collective effects related to the interaction between nanoparticles at high degrees of filling [2].

The properties of nanocomposites with high concentrations of semiconductor nanoparticles are still insufficiently studied, although there are many publications devoted to the conductivity of metal–dielectric nanocomposites near the percolation threshold. The hopping character of conductivity in a certain interval of compositions near the percolation threshold ensures a high sensitivity of nanocomposites to external factors. Therefore, the investigation of the electrical properties of polymer-based nanocomposites and creation of various highly responsive sensors based on such materials are important current tasks.

Experimental. A matrix for polymeric composites with high concentrations of CdS nanoparticles was prepared by mixing poly(vinyl alcohol) (PVA), possessing good film-forming properties, and poly(acrylic acid) (PAA), characterized by a high sorption potential with respect to cadmium ions. The composites were obtained using a two-stage process. First, cadmium ions were introduced into a swollen PVA–PAA matrix, and then, highly disperse cadmium sulfide was synthesized in the matrix as described in [3]. The films were prepared by casting a 4% aqueous solution of the polymer-based composite. The nanocomposite films had a typical thickness of 100 μm. The content of cadmium ions and CdS in a film sample was determined thermogravimetrically, using a residue of the sample burned in a Mettler TA-4000 thermal analyzer. The average particle size determined from the halfwidth of the X-ray diffraction reflection was ≈50 Å. The dimensions of particles in nanocomposites were studied in detail previously and confirmed by the results of electron-microscopic measurements [2].

This study was performed using a nanocomposite film with a CdS content of 31 vol % in the PVA–PAA matrix. The typical sample dimensions were 1×4 mm. The temperature dependence of the conductivity was studied by placing a sample with silver paste contacts on a corundum substrate bearing a resistive heater and a chromel–copel thermocouple. The measurements were performed using an E6-13A teraohmmeter, a V7-29 electrometer, and an N307/1 recorder. The bolometric measurements were carried out using an MDR-2 monochromator, a 500-W incandescent lamp, an INO-2 power meter, and an RTN-31S calibrated thermoelectric sensor.

Results. The shape of the current–voltage characteristics was typical of high-ohmic semiconductors, in which the current is limited by the space charge of trapped carriers [4]. For this reason, the *I–V* curves of the nanocomposites were measured after an equilibrium value of the current was established. The maximum voltage across the sample was 1000 V. In a double logarithmic scale, the *I–V* curve is well approximated by two lines corresponding to power dependences of the current on the applied voltage with exponents equal to 1 and 2. Thus, the *I–V* curve obeys the Ohm law in the initial region and the quadratic law at higher volt-

1063-7850/04/3008-0663$26.00 © 2004 MAIK "Nauka/Interperiodica"

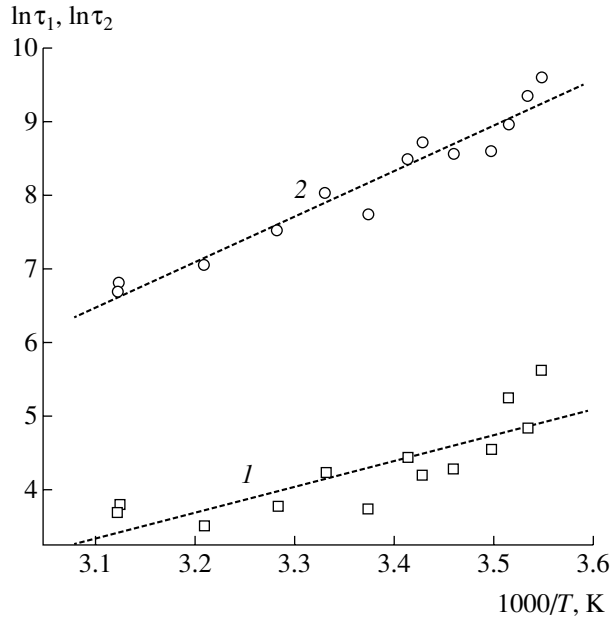

Fig. 1. The temperature dependence of the current relaxation times (*1*) τ_1 and (*2*) τ_2 in a polymer–CdS nanocomposite film.

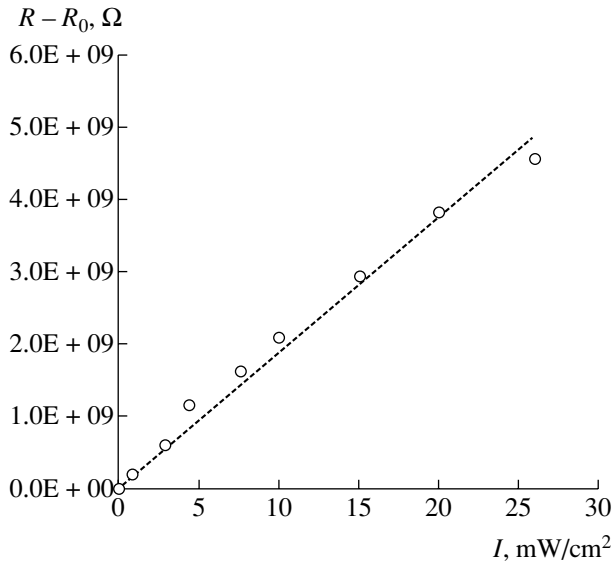

Fig. 2. A plot of the differential resistance $R - R_0$ versus incident light intensity I for a test bolometer based on a polymeric nanocomposite film.

ages, which is characteristic of the injection current limited by the space charge. Using the voltage $V_x \approx 200$ V, corresponding to the transition from linear to quadratic behavior, and the conductivity $\sigma = 3 \times 10^{-11}$ $(\Omega\ \text{cm})^{-1}$ in the ohmic region at $T = 20$°C, it is possible to evaluate the equilibrium density n of charge carriers and their drift mobility μ from the relations [5]

$$V_x = enL^2/\varepsilon, \qquad \sigma = \mu ne, \tag{1}$$

where L is the distance between contacts and ε is the permittivity of the nanocomposite. Our estimations gave the carrier density $n \approx 10^{11}$ cm^{-3} and the effective mobility $\mu \approx 0.1$ cm^2/(V s).

Our measurements revealed long-term relaxation currents in the nanocomposites studied. If the electrodes are short-circuited after keeping a sample at a high voltage, a discharge current is observed in the external electric circuit. The results of fitting by least squares showed that the relaxation current kinetics is best described by a sum of two exponents,

$$I(t) = A^* \exp[-t/\tau_1(T)] + B^* \exp[-t/\tau_2(T)], \tag{2}$$

where the typical vales of exponents at $T = 20$°C are $\tau_1 \sim 70$ s and $\tau_2 \sim 6200$ s. We have studied the temperature dependence of these characteristic times and established that both τ_1 and τ_2 values decrease with increasing temperature (Fig. 1). The temperature dependence of the relaxation time obeys the exponential law

$$\tau = A\exp(E_a/kT) \tag{3}$$

with the activation energies $E_a(\tau_1) = 0.3 \pm 0.06$ eV and ~70 s and $E_a(\tau_2) = 0.53 \pm 0.03$ eV. We may suggest that these energies characterize the positions of traps responsible for the discharge current in the polymeric nanocomposite studied.

Bolometer based on a polymer–CdS nanocomposite film. The temperature dependence of conductivity of the nanocomposite film studied in a temperature interval of 20–60°C is well described by a single exponent with an activation energy of 1.06 eV. This value corresponds to the temperature coefficient of resistance $\alpha = 0.15$ K^{-1} at room temperature. Materials with such a high α value can be used for the creation of thermal sensors. Thermosensitive elements based on polymeric nanocomposites could be used as bolometers [6]. The value of α reached in our nanocomposites is significantly greater than the values typical of bolometers with metallic ($\alpha \sim 0.003$ K^{-1}) and semiconductor ($\alpha \sim 0.03$ K^{-1}) sensors.

In order to evaluate the room-temperature parameters of a bolometer with a polymeric nanocomposite film, we measured the dependence of the film resistance on the intensity of incident light (Fig. 2). These measurements were performed for a sample with parameters analogous to those described above. The dark resistance of the sample at 100 V was 3.6×10^{10} Ω, which corresponded to the ohmic region of the current–voltage characteristic where the space charge could be ignored. The integral sensitivity of the test bolometer was 5×10^{12} Ω/W, which corresponded to a volt–watt responsivity of 1.39×10^4 V/W or a relative resistance response of 1.75×10^4%/W. Note that the

typical integral sensitivity of semiconductor bolometers reaches the same order of magnitude [7].

However, our nanocomposite film and the prototype design were not optimized for bolometric applications and, hence, the parameters can be further improved. In particular, the sample film was too thick (≈100 μm). A decrease in the film thickness and optimization of the design will increase the sensitivity. Use of the nanoparticles of other semiconductors may provide for an increase in the conductivity activation energy and, hence, in the thermal coefficient of resistance. In addition, by selecting the film material, it is also possible to modify the absorption spectrum of the active element and obtain either nonselective bolometers or devices selective with respect to a certain spectral interval. It is also possible to obtain an array of bolometers on the same flexible polymeric nanocomposite film of large area.

Acknowledgments. This study was supported by the Russian Foundation for Basic Research (project no. 01-03-32931) and the ICMR Foundation (Japan).

REFERENCES

1. I. A. Akimov, I. Yu. Denisyuk, and A. M. Meshkov, Opt. Spektrosk. **72**, 1026 (1992) [Opt. Spectrosc. **72**, 558 (1992)].
2. A. E. Varfolomeev, A. V. Volkov, and D. Yu. Godovskiĭ, Pis'ma Zh. Éksp. Teor. Fiz. **62**, 344 (1996) [JETP Lett. **62**, 367 (1996)].
3. A. V. Volkov, A. L. Volynskiĭ, M. A. Moskvina, and N. F. Bakeev, Vysokomol. Soedin., Ser. A **44**, 1390 (2002).
4. R. H. Bube, *Photoconductivity of Solids* (Wiley, New York, 1960; Inostrannaya Literatura, Moscow, 1962).
5. M. A. Lampert and P. Mark, *Current Injection in Solids* (Academic Press, New York, 1970; Mir, Moscow, 1973).
6. D. Zaretsky, A. Varfolomeev, A. Volkov, *et al.*, Jpn. Patent Appl. No. 11-366578 (1999).
7. R. A. Smith, F. E. Jones, and R. P. Chasmar, *Detection and Measurement of Infrared Radiation*, 2nd ed. (Clarendon Press, Oxford, 1957; Inostrannaya Literatura, Moscow, 1959).

Translated by P. Pozdeev

Technical Physics Letters, Vol. 30, No. 8, 2004, pp. 666–668. Translated from Pis'ma v Zhurnal Tekhnicheskoĭ Fiziki, Vol. 30, No. 16, 2004, pp. 7–12.

The Effect of Photon Flux on the Properties of a Ni–Cu Foil

A. A. Kolotov, F. Z. Gil'mutdinov, and V. Ya. Bayankin

Physicotechnical Institute, Ural Division, Russian Academy of Sciences, Izhevsk, Udmurtia, Russia

e-mail: less@fti.udm.ru

Received February 9, 2004

Abstract—Experimental data on the irradiation-induced long-range effects in rolled Ni–Cu foils are presented. Dose-dependent variations in the microhardness and composition of the surface layers were observed on both exposed and unexposed sides of the samples. Based on the observed microhardness and composition variations in depth of the samples and the results of X-ray diffraction measurements, a hypothesis concerning the role of the initial nonequilibrium state of a material in the photoinduced long-range effect is put forward. © *2004 MAIK "Nauka/Interperiodica".*

Introduction. In recent years [1–3], it was established that various energetic actions (e.g., ion bombardment) upon solids modify the sample properties in a layer whose thickness significantly exceeds theoretical estimates. There is no commonly accepted opinion concerning mechanisms of this phenomenon, referred to as the irradiation-induced long-range effect. Various possible mechanisms were proposed in [1, 2]. In most cases, the main mechanism responsible for the long-range effects caused by ion beams involves the excitation of elastic waves and their interaction with a system of extended defects, in particular, with impurity–defect clusters and dislocations (especially in highly dislocated materials).

Similar long-range effects were also observed in rolled metal foils (where the density of dislocations can be as high as 10^9–10^{10} cm^{-2} [1, 2]) exposed to photon fluxes. It was demonstrated [1, 3–5] that these effects have a profound nature, not reduced to simple radiation heating.

Experimental. The experiments were performed on 30-μm-thick rolled foils of a 40% Ni–60% Cu alloy. The samples were exposed in air to the radiation of 100- and 200-W halogen lamps at a source to sample distance of R = 70 mm. The radiation spectrum was close to that of an incandescent lamp with a tungsten filament. In order to improve the heat removal, each sample during the exposure was mounted on a massive metal plate.

The microhardness H was measured using a PMT-3 instrument at an indenter load of 20 g. The elemental concentration–depth profiles of the surface layers of the samples before and after irradiation were determined by secondary-ion mass spectrometry (SIMS) in combination with ion sputtering. The SIMS measurements were performed with an MS-7201 spectrometer; the sample surface was sputtered by 4.5-keV argon ions at an ion beam current density of 20 $\mu A/cm^2$, which corresponded to a calculated sputtering rate of 3 nm/min.

Results and discussion. By analogy with the results presented in [2], the irradiation of our foils at the source powers indicated above led to a change in the values of microhardness H measured on both the front (exposed) and rear side of the sample. Investigation of the dose dependence of H in a broad range of exposures (Fig. 1) showed that microhardness varied in a nonmonotonic manner: the changes had alternating signs and tended to zero for large doses. Upon termination of the exposure, the microhardness returned to the initial value. Taking into account that microhardness is a structure-sensitive parameter, this behavior can be explained by relaxation of the structure (most likely, of the defect structure) to the initial state. Similar effects were reported in [3–5].

Thus, we can ascertain that irradiation gives rise to structural changes in the surface layers and in the volume of the foil. This is accompanied by the redistribution of elements in the surface layers on both sides of the samples, as evidenced by the results of SIMS profiling. Figure 2 shows the typical pattern of redistribution of the alloy components (compared to the initial composition) in a film exposed for 3 s to a 100-W lamp (the profiles were measured within 1 h after irradiation of the sample). As can be seen, the redistribution of components takes place on both the exposed and (to a comparable extent) unexposed sides of the foil, thus showing manifestations of the long-range effect. The exposure leads to enrichment of the alloy surface with nickel. The question as to why nickel segregates at the sample surface is still unanswered. We may suggest that this ratio of components is unstable even relative to the initial state, being caused by the additional "energy

1063-7850/04/3008-0666$26.00 © 2004 MAIK "Nauka/Interperiodica"

pumping" and leading to the subsequent relaxation of the system to the initial state over the course of several hours after the exposure.

In order to elucidate the role of the structural factor in the manifestation of the photoinduced long-range effect, we studied foils annealed for 30 min at 600°C in a vacuum furnace. The measurements of microhardness in the annealed samples showed no evidence of the long-range effect. Thus, based on the obtained experimental data, we may suggest that the photoinduced long-range effect is related to the initial inhomogeneity of the alloy structure, that is, to the presence of an elastically stressed state in the as-rolled film material. Following [3–5], we suggest that the main mechanism responsible for the observed manifestations of the long-range effect is excitation of the elastic waves and their interaction with the initial structural imperfections. Naturally, the question arises as to what is the source of excitation of these waves. For photon irradiation, one possible mechanism of the long-range effect is as follows. From the standpoint of quantum mechanics, the interaction of matter with radiation is a resonance phenomenon corresponding to equality of the photon energy and the energy required for the system transition from one state to another. In metals, this is usually manifested by excitation of the electron subsystem. One of the main energy characteristics of a metal is the work function, defined as the energy required for transferring an electron from the Fermi level to the infinity.

In our case, the incident photon energy is too small to excite the electron subsystem of the metal, which at first glance contradicts the proposed model. However, it was demonstrated [6, 7] that the electron work function can be significantly reduced in strained materials. This effect is primarily related to a change in periodicity of the electron density, which, in turn, modifies the electrostatic potential in the metal. In addition, a very important factor decreasing the electron work function is the presence of surface dislocations. The dislocations produce a dissipative effect on emerging at the surface (both front and rear), thus favoring a decrease in the electron work function. Additional photon–electron interaction, dependent on the radiation frequency, may enhance this effect. Thus, the system under consideration may feature the photoeffect. An alternative model of the photoeffect proposed in [3] was based, in contrast to our model, on the presence of a natural oxide layer on the metal surface. We believe that the photoeffect leads to excitation of the electron subsystem in the surface layers, which is equivalent to the formation of a localized hole. This hypothesis is confirmed by a change in the surface potential observed for the irradiated surface. If the hole localization time is comparable with the period of thermal oscillations of atoms, the surface layers may feature structural transformations.

Thus, we may suggest that the elastically stressed state of our samples makes possible the photoeffect leading to violation of the energy balance in the system.

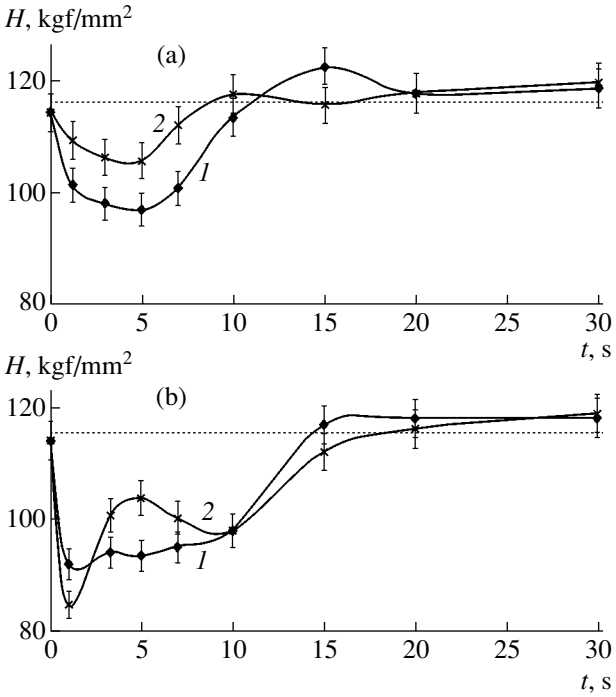

Fig. 1. Variation of the microhardness H of the (*1*) front (exposed) and (*2*) rear sides of Ni–Cu foils with increasing exposure time t for samples irradiated using (a) 100-W and (b) 200-W halogen lamps.

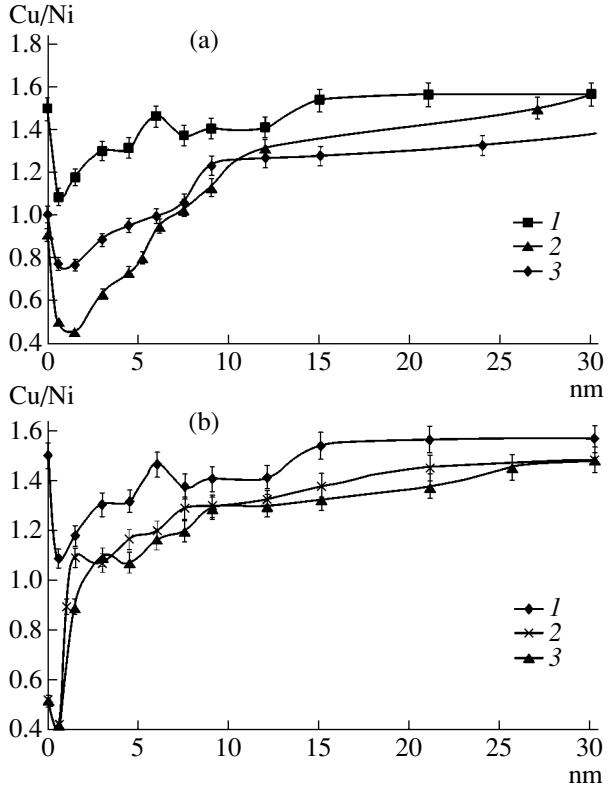

Fig. 2. SIMS depth–composition profiles of a NI–Cu foil after 3-s exposure to a 100-W halogen lamp: (a) front (exposed) side (*1*) before irradiation and (*2*) 5 and (*3*) 50 min after irradiation; (b) rear (unexposed) side (*1*) before irradiation and (*2*) 15 and (*3*) 40 min after irradiation.

In systems with developed dislocation structures, this is manifested by displacement of the dislocation loops toward sinks (surfaces, grain boundaries, etc.), which is probably the driving force for the out-diffusion of nickel atoms to the foil surface. In the field of elastic stresses, this process can acquire an avalanche character and is accompanied by a change in the defect structure in the volume and in the surface layers on both the exposed side and (due to the long-range effect) the rear side of the foil. Considering the dependence of the observed effect on the exposure time (i.e., on the absorbed radiation dose), we may suggest that the initial irradiation stage (small exposure times) is characterized by a relatively small density of mobile defects. Under these conditions, the dislocation loops move freely and change the dislocation structure. For prolonged irradiation, the intensity of motion of the dislocation loops increases and the moving loops begin to collide with each other. If the colliding loops have different orientations, the collisions result in the formation of sessile dislocation loops capable of blocking the motion of other dislocations.

Acknowledgments. This study was supported by the Russian Foundation for Basic Research, project no. 02-02-16670.

REFERENCES

1. D. I. Tetelbaum, E. V. Kuril'chik, A. Yu. Azov, *et al.*, Poverkhnost, No. 5, 87 (2000).
2. Yu. V. Martynenko, Itogi Nauki Tekh., Ser.: Puchki Zaryazhennykh Chastits i Tverd. Telo **7**, 8 (1993).
3. D. I. Tetelbaum, A. Yu. Azov, and P. I. Golyakov, Pis'ma Zh. Tekh. Fiz. **29** (2), 35 (2003) [Tech. Phys. Lett. **29**, 57 (2003)].
4. D. I. Tetelbaum, A. A. Trofimov, A. Yu. Azov, *et al.*, Pis'ma Zh. Tekh. Fiz. **24** (23), 9 (1998) [Tech. Phys. Lett. **24**, 910 (1998)].
5. D. I. Tetelbaum, E. V. Kuril'chik, A. Yu. Azov, *et al.*, Poverkhnost, No. 4, 67 (2003).
6. V. V. Pogosov and O. M. Shtepa, Metallofiz. Noveĭshie Tekhnol. **24**, 1651 (2002).
7. V. A. Zhuravlev, *Lectures on Quantum Theory of Metals* (Inst. Komp'yut. Issled., Moscow, 2002) [in Russian].

Translated by P. Pozdeev

Technical Physics Letters, Vol. 30, No. 8, 2004, pp. 669–671. Translated from Pis'ma v Zhurnal Tekhnicheskoĭ Fiziki, Vol. 30, No. 16, 2004, pp. 13–18.

Simulation of the Interaction of Low-Energy Ions with Copper Clusters on a Graphite Surface

G. V. Kornich*, G. Betz, V. I. Zaporojtchenko, and E. V. Pugina

Zaporozhye National Technical University, 69063 Zaporozhye, Ukraine
Institut für Allgemeine Physik, Technische Universität Wien, A-1040 Wien, Austria
Technische Fakultät, Christian Albrechts Universität, 24143 Kiel, Germany
** e-mail: gkornich@zntu.edu.ua*

Received March 3, 2004

Abstract—The sputtering of a lone cluster consisting of 27 copper atoms from a (0001) graphite surface bombarded by normally incident 100- and 200-eV Xe^+ ions was simulated by the molecular dynamics method. The angular distributions of sputtered copper atoms and scattered xenon ions are discussed. © *2004 MAIK "Nauka/Interperiodica".*

Previously [1–3], we studied by the molecular dynamics method [4] the sputtering of copper clusters comprising several dozens of atoms from a (0001) single crystal graphite surface bombarded by 200-eV Ar^+ ions at normal incidence. It was shown that the angular distributions of the scattering probability exhibit six peaks in the ⟨1100⟩ directions corresponding to the most open directions in the structure of copper clusters on the graphite substrate.

In this study, we have simulated the sputtering of a lone surface cluster consisting of 27 copper atoms (27Cu) from a (0001) single crystal graphite surface bombarded by 100- and 200-eV xenon ions. We have also traced the scattering of Xe^+ ions interacting with the target. The (0001) graphite substrate was modeled by two atomic layers, each containing 960 carbon atoms, respectively. The initial 27Cu cluster on the graphite surface comprised three atomic layers consisting of 14, 10, and 3Cu atoms (in order of increasing distance from the substrate surface). The method used for creating the two-component cluster–substrate system and the molecular dynamics algorithm were described in detail previously [1]. In the present model, in contrast to that studied in [1], the 27Cu–graphite substrate system was created by free relaxation allowed only in the (0001) plane in order to avoid uncontrolled distortions. For each primary ion energy, we simulated 500 events of the normal incidence of Xe^+ ions onto the target. The development of each collision cascade was followed for 3 ps.

Figure 1 shows the azimuthal distribution of the differential sputtering yield $dY/d\alpha$ of single Cu atoms from a 27Cu cluster on the graphite surface bombarded by xenon ions of two energies. The distribution obtained for the 200-eV Xe^+ ions (curve *1*) is qualitatively similar to that observed for 75Cu clusters sputtered by Ar^+ ions of the same energy [1, 3]. In particular, there are six peaks of the $dY/d\alpha$ value separated by 60°, which correspond to the most open directions of

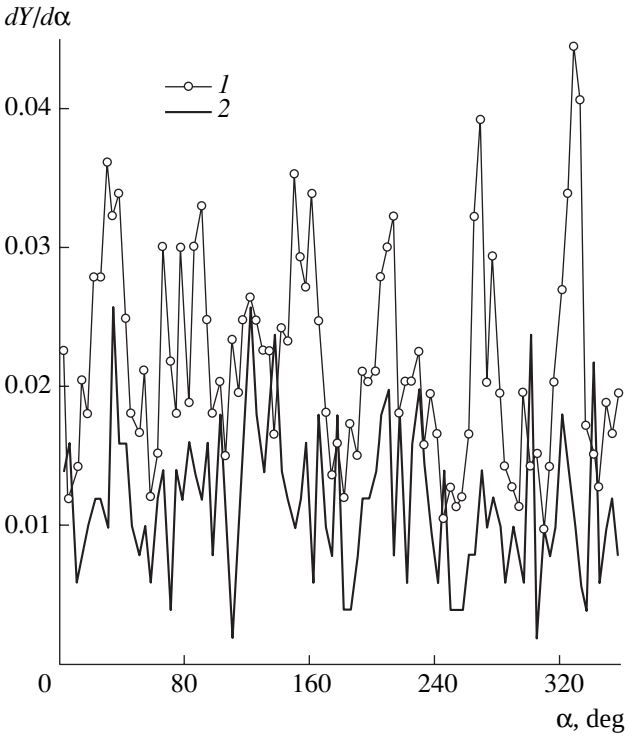

Fig. 1. The azimuthal distribution of the differential sputtering yield $dY/d\alpha$ of single Cu atoms from a 27Cu cluster on the (0001) graphite surface bombarded by (*1*) 200-eV and (*2*) 100-eV Xe^+ ions; Y is the sputtering yield (atoms per ion) and α is the azimuthal angle measured from the [1000] direction counterclockwise in the (0001) plane on the graphite surface).

1063-7850/04/3008-0669$26.00 © 2004 MAIK "Nauka/Interperiodica"

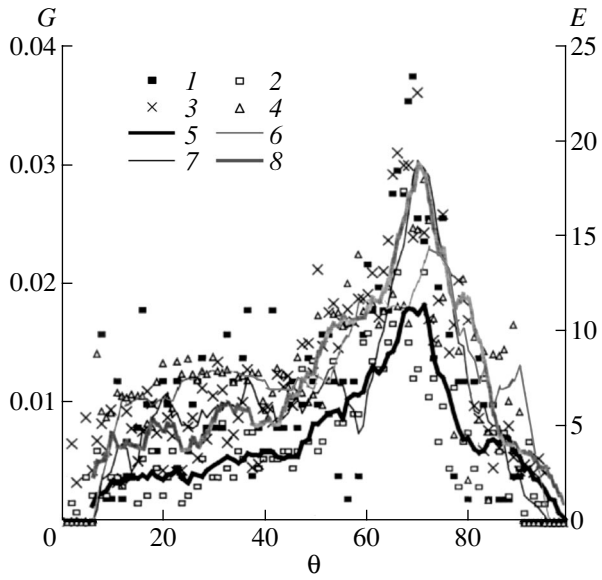

Fig. 2. The polar distribution of the (*1*, *6*; *2*, *5*) scattering probability *G* and (*3*, *8*; *4*, *7*) average energy *E* ions scattered from a 27Cu cluster on a (0001) graphite surface bombarded by Xe^+ ions with a primary energy of (*1*, *6*; *4*, *7*) 100 eV and (*2*, *5*; *3*, *8*) 200 eV. Curves *6*, *5*, *8*, and *7* are six-point piecewise-linear approximations of experimental points *1*, *2*, *3*, and *4*, respectively.

the 27Cu cluster structure. In contrast, the distribution of $dY/d\alpha$ for Cu atoms sputtered by 100-eV Xe_+ ions (Fig. 1, curve *2*) exhibits no azimuthal periodicity.

Xenon ions with a primary energy of 100 eV, striking the same points of the 27Cu cluster as the 200-eV ions, transfer a lower energy in the course of sequential collisions, leading to sputtering of a terminal atom from the cluster. Due to many-body atom–atom and ion–atom interactions, which play a relatively more significant role with decreasing energy and increasing ion mass (Xe versus Ar), the effect of focusing of a sputtered atom by the surrounding atoms of the cluster is not manifested. This leads to an increase in the contribution of recoil atoms (having randomly distributed directions of motion) to the sputtering yield. In addition, the lack of periodicity in the pattern of azimuthal peaks of $dY/d\alpha$ for 100-eV Xe^+ ions is also due to the fact that an incident ion transfers energy to the surrounding atoms and does not reach the atomic chain (accessible for a 200-eV ion) capable of releasing a sputtered atom.

Angular distributions of the sputtered Cu atoms with respect to the polar angle θ (measured from the external normal to the substrate surface) observed for Xe^+ ions with a primary energy of both 100 and 200 eV are qualitatively similar to the distributions observed for 200-eV Ar^+ ions [1–3] and exhibit a single maximum in the region of 90°. An insignificant number of sputtered Cu atoms, together with scattered Xe^+ ions moving at polar angles above 90°, were not reflected from the substrate because of its limited size.

Figure 2 shows the polar distributions of the scattering probability *G* of Xe^+ ions and their average energies for a primary ion energy of 100 eV (points *1* and the corresponding six-point piecewise-linear approximation *6*) and 200 eV (points *2* and approximation *5*). As can be seen, the distributions exhibit maxima at virtually the same polar angle (~70°), which represent overlapping peaks in the probability of ion scattering from the cluster and, in many cases, of the secondary (after the ion–cluster interaction) reflection from the graphite substrate. A significant increase in the scattering probability for the 100- and 200-eV ions begins at $\theta \sim 60°$ and 45°, respectively, reflects the increasing contribution of ions reflected from the substrate. The probability of reflection at smaller polar angles for these energies decreases because a considerable fraction of incident ions penetrates into the graphite surface. The difference between the critical angles corresponding to a sharp increase in the scattering probability of ions with different energies is determined by the elastic properties of the (0001) graphite plane bombarded by the ions. The total reflection coefficients for 100- and 200-eV Xe^+ ions are ~1.0 and 0.68, respectively, which is manifested by the mutual arrangement of the scattering probability curves in Fig. 2. Interacting with the 27Cu cluster, incident xenon ions with a primary energy of 100 and 200 eV transferred 67–72% of their initial energy to the cluster.

As can be seen from the data in Fig. 2, the polar angles corresponding to maxima in the average energies of reflected xenon ions virtually coincide with the angles of maxima in the scattering probability for both energies, which is indicative of the dominating contribution of high-energy ions to the peak of ions reflected at large polar angles. The mutual arrangement of the curves of average energy shows that, for 100-eV incident ions (points *4*, approximation *7*), a greater average energy of scattered ions is observed within the interval of polar angles below 45°, while for 200-eV incident ions (points *3*, approximation *8*), ions of greater average energies are scattered in the interval of angles above 45°. This behavior is also related to the effect of substrate.

Ions scattered at small polar angles interact predominantly with the copper cluster. The 200-eV projectiles are obviously capable of penetrating deeper into the cluster and give a part of their energy to the substrate. In contrast, 100-eV Xe^+ ions interact predominantly with copper atoms in the two upper layers. In both cases, many-body interactions of Xe^+ ions with copper atoms in the cluster are also manifested by the effect of collective reflection of a heavy ion from much lighter atoms of the surface cluster. An analogous phenomenon of the collective reflection of a heavy ion from much

lighter target atoms was simulated [5] for 50-eV Xe^+ ions normally incident onto a Ni(100) surface.

A comparison of the above data and the results observed for copper clusters on a graphite substrate bombarded by 200-eV Ar^+ ions shows that the average energies of scattered Xe^+ ions are on the average two to four times smaller than those of Ar^+ ions of the same primary energy. This difference is related to different mechanisms of the reflection of heavy and light ions from copper clusters. The polar angles corresponding to maxima in the scattering probabilities and average energies of reflected Xe^+ and Ar^+ ions generally coincide, which reflects the dominating role of a graphite substrate in the formation of the angular distributions for normally incident low-energy ions of both kinds scattered at large polar angles.

REFERENCES

1. G. V. Kornich, G. Betz, V. I. Zaporojtchenko, and A. I. Bazhin, Pis'ma Zh. Tekh. Fiz. **29** (22), 33 (2003) [Tech. Phys. Lett. **29**, 938 (2003)].
2. G. V. Kornich, G. Betz, V. I. Zaporojtchenko, and A. I. Bazhin, in *Proceedings of the 16th International Conference on Surface–Ion Interaction, Moscow–Zvenigorod, 2003*, Vol. 1, pp. 65–68.
3. G. V. Kornich, G. Betz, V. I. Zaporojtchenko, and A. I. Bazhin, Izv. Ross. Akad. Nauk, Ser. Fiz. **68**, 304 (2004).
4. J. M. Haile, *Molecular Dynamics Simulation–Elementary Methods* (Wiley, New York, 1992).
5. G. V. Kornich, G. Betz, A. I. Bazhin, and V. G. Kornich, Izv. Ross. Akad. Nauk, Ser. Fiz. **66**, 89 (2002).

Translated by P. Pozdeev

Technical Physics Letters, Vol. 30, No. 8, 2004, pp. 672–674. Translated from Pis'ma v Zhurnal Tekhnicheskoĭ Fiziki, Vol. 30, No. 16, 2004, pp. 19–25.

High-Current Penning Discharge with Self-Heated Cathode

L. A. Zyul'kova, A. V. Kozyrev*, and D. I. Proskurovsky

Institute of High-Current Electronics, Siberian Division, Russian Academy of Sciences, Tomsk, Russia

** e-mail: kozyrev@to.hcei.tsc.ru*

Received March 1, 2004

Abstract—A theoretical model of self-sustained Penning (reflective) discharge is formulated based on the equation of continuity of the electron flow and the equation of energy balance on the cathode. Using the proposed theory, it is possible to calculate the current–voltage characteristic of a high-current reflective discharge with self-heated cathode in a broad range of discharge cell dimensions, magnetic fields, and electron work functions of the cathode materials. The theory predicts two regimes of discharge operation with thermionic emission from the cathode: (i) a low-voltage regime with a high current density and (ii) a high-voltage regime with a significantly lower current density. An advantage of the developed theory is that, in the limiting case, it also describes the operation of normal cold cathode reflective discharge. *© 2004 MAIK "Nauka/Interperiodica".*

Reflective discharge, also known as Penning discharge, has been known for many years and used as the source of charged particles—electrons and ions [1–3]. An important advantage of this discharge is high efficiency of the process of plasma formation in a broad range of electrical parameters and system geometries. Although the main laws of Penning discharge (in particular, a decrease in the discharge voltage with increasing gas pressure and magnetic induction in the gap) are well known, no convenient theory capable of calculating all discharge parameters (including the current–voltage characteristic) under preset conditions has been developed so far. Recently, Nikulin [4] formulated a theoretical model which describes the interplay of the ionization processes and the loss of charged particles in the reflective discharge quite well. Using this model, it is possible to determine in the general case the conditions necessary for maintaining the existence of discharge plasma in crossed electric and magnetic ($B \times E$) fields. Unfortunately, the original model [4] was considered in one-dimensional geometry, which does not allow the results of calculations to be applied to real (usually axisymmetric) discharge cells.

There are several factors hindering calculations of the current–voltage characteristic of a real reflective discharge with satisfactory accuracy. First, considerable difficulties are encountered in calculations of the ionization rate and the motion of charged particles in the crossed fields. Second, even within the framework of a linear model of gas ionization and charged particle drift ensuring a quite reliable evaluation of the discharge voltage, the discharge current cannot be calculated without introducing external circuit parameters. However, once such parameters are introduced, the model loses generality and does not allow general relations between the system parameters and characteristics to be analyzed.

Sometimes, additional electrodes are specially introduced into the discharge. These electrodes exhibit self-heating and emit electrons, thus significantly influencing the discharge voltage and current [3, 5]. On the one hand, such an additional heated element complicates calculation of the discharge parameters and introduces significant nonlinearity into the system of model equations. On the other hand, the presence of this element "binds" the theoretical model to certain absolute values of the electrode temperature and emission current. Below, we will demonstrate that such a nonlinear element introduced into a theoretical model allows all other parameters of the reflective discharge to be calculated with satisfactory accuracy.

Consider the classical axisymmetric discharge cell comprising a ring anode and two parallel disk cathodes of radius R spaced by distance h. The magnetic field lines are parallel to the anode axis and perpendicular to the cathode plane. One disk cathode is assumed to be thermally insulated and, being strongly self-heated, can produce thermionic emission. The other disk cathode remains cold. We have calculated the current–voltage characteristic of this discharge cell using the following simplifying assumptions.

(i) We consider a stationary high-current regime, whereby all voltage drops in a cathode region of the volume discharge. The main part of the interelectrode volume is occupied by quasi-neutral plasma (discharge plasma column) separated from electrodes by narrow space charge regions.

(ii) It is assumed that plasma in the discharge column is weakly ionized and the density of neutral atoms is independent of the current. This assumption restricts

the applicability of the model to the range of relatively high pressures, especially in the high-current regime.

(iii) We assume that a flow of fast electrons with energies approximately corresponding to the discharge voltage is formed in the cathode region. This electron flow transfers energy from the source to the plasma and ensures ionization of the gas in the discharge column.

(iv) Ionization of the gas by slow plasma electrons is ignored. The role of plasma electrons reduces to transferring a part of the electric current through the gap in the direction perpendicular to the magnetic field. This assumption is valid, provided that the discharge voltage is much greater than the ionization potential of the gas [4].

(v) The model assumes that ions in the plasma column are not influenced by the magnetic field and the ion current is homogeneously distributed over the cathode surface. Inhomogeneity of the plasma distribution in height of the discharge cell is ignored. This averaging over the height significantly simplifies calculations and facilitates the analysis of the general features of discharge.

(vi) A disk cathode capable of producing thermionic emission is assumed to be thermally insulated. The cathode temperature is determined by the balance of power supplied with bombarding ions and the radiative heat removal from the surface. The temperature of the self-heated cathode is assumed to be the same over the whole surface.

The current–voltage characteristic of the Penning discharge can be calculated as described in [5]. One parameter in this problem is the λ of fast electrons, which determines the scale on which a fast electron with the kinetic energy eU_c moves across the magnetic field during the lifetime τ_f. Such electrons perform random walk across the magnetic field with a step on the order of the Larmor radius and a frequency close to the rate of collisions in the plasma. The characteristic electron diffusion length is given by the formula

$$\lambda(U_c, B) = \sqrt{D_f \tau_f} = \sqrt{\frac{4m}{3E_i}}\frac{U_c}{B}, \quad (1)$$

where U_c is the voltage drop across the cathode region, D_f is the diffusion coefficient, B is the magnetic induction, m is the electron mass, and E_i is the average energy of the electron–ion pair formation. Within the framework of the proposed model, the λ value is independent of the gas pressure [4, 5].

Another parameter in the problem under consideration is the electron multiplication coefficient μ, equal to the number of secondary electrons appearing upon the loss of one fast electron. This coefficient is defined as

$$\mu(U_c) = eU_c/E_i. \quad (2)$$

Applying the calculation procedure developed in [5] to our discharge geometry, we obtain the condition of self-sustained discharge involving the discharge cell parameters R and h:

$$\left[\frac{J_{em}}{J_{ic}} + \gamma\right]\left[\mu + \frac{\lambda}{R}\left(\frac{R}{h} - 2(\mu + 1)\right)\frac{I_1(R/\lambda)}{I_0(R/\lambda)}\right] = 1. \quad (3)$$

Here, J_{em} is the total current of thermionic emission from the self-heated cathode, J_{ic} is the total ion current to the cathode, γ is the coefficient of ion-induced electron emission from the cathode, and $I_0(x)$ and $I_1(x)$ are the modified Bessel functions of the zeroth and first order.

The power balance on the hot cathode surface can be written as

$$S_t \varepsilon_T \sigma T_c^4 \simeq 1/2 U_c J_{ic}, \quad (4)$$

where σ is the Stephan–Boltzmann constant, T_c is the hot cathode temperature, $\varepsilon_T \approx 0.5$ is the emissivity of the hot cathode, S_t is the cathode surface area, and the factor 1/2 takes into account that only half of the ion current strikes the self-heated cathode.

The total current of thermionic emission can be calculated using the Richardson–Dushman formula

$$J_{em} = \pi R^2 A_0 T_c^2 \exp(-\varphi_c/kT_c), \quad (5)$$

where φ_c is the electron work function of the hot cathode material and $A_0 \approx 100$ A/(cm^2 K^2).

Using the system of Eqs. (1)–(5), it is possible to calculate the cathode temperature, thermionic emission current, and ion current to cathode for a given discharge cell geometry, magnetic induction, and discharge voltage. Then, we readily determine the total discharge current as

$$J = J_{em} + (1 + \gamma) J_{ic}. \quad (6)$$

Thus, we have calculated the current–voltage characteristic of a discharge cell with known characteristics of the cathode material. Simplifications introduced into the model resulted in the absence of gas pressure in all equations. For this reason, the obtained current–voltage characteristic also does not explicitly depend on the gas pressure. This parameter can be implicitly taken into account if we allow for the relationship between the average energy E_i of the electron–ion pair formation and the real kinetics of the ionization process dependent on the gas pressure.

Analysis of the above system of equations showed that there exists a certain critical magnetic induction B_{cr} determining the range of voltages admitting solutions for the discharge current. It was found that, for $B < B_{cr}$, a solution for the current exists for any applied voltage, while $B > B_{cr}$ implies that there appears an interval of voltages in which no stationary solutions for the current can exist. The physical reasons for the appearance of this "forbidden" interval can be elucidated by tracing variations of the discharge current and the self-heated

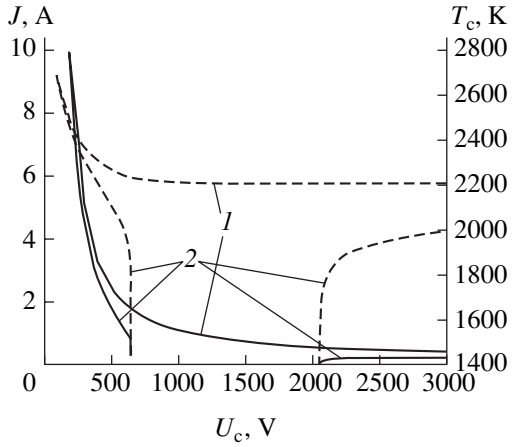

Fig. 1. Calculated current–voltage characteristics (solid curves) and temperatures (dashed curves) of the reflective discharge with self-heated tungsten cathode (h = 1 cm, R = 1 cm, γ = 0.1) for the magnetic induction below and above the critical value ($B_{cr} \approx 0.087$ T): (*1*) B = 0.05 T ($<B_{cr}$); (*2*) B = 0.1 T ($>B_{cr}$).

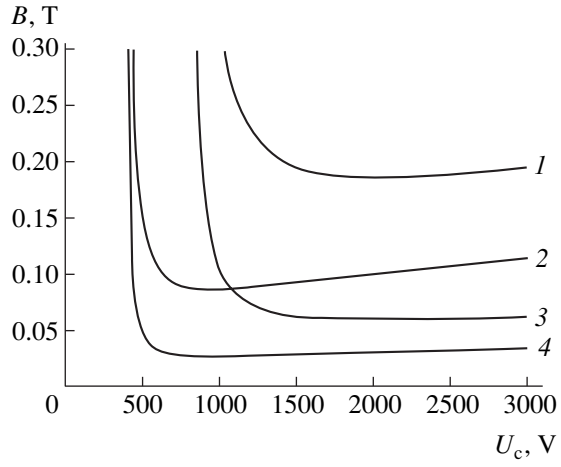

Fig. 2. Plots of the discharge voltage U_c versus magnetic induction B for the cold cathode reflective discharge calculated for various cathode parameters (γ, R): (*1*) 0.05, 1 cm; (*2*) 0.05, 3 cm; (*3*) 0.1, 1 cm; (*4*) 0.1, 3 cm.

cathode temperature as functions of the discharge voltage at a given magnetic induction.

Figure 1 shows two examples of behavior of the discharge current and the cathode temperature dependent on the voltage for different relations between B and B_{cr}. As can be seen for $B > B_{cr}$, the current–voltage characteristic separates into two parts: one branch is characterized by a high current density at relatively low voltages, while the other branch corresponds to high voltages and significantly lower current densities. Note that both branches correspond to high cathode temperatures. In the high-voltage region, the current is almost independent of the voltage. The main peculiarity of this regime is that, on approaching the forbidden interval of voltages, the cathode temperature and the discharge current sharply drop and tend to zero. This behavior allows the boundaries of the forbidden interval to be interpreted as the voltages corresponding to reflective cold cathode discharge at a given magnetic induction.

The relation between magnetic induction and applied voltage, $B(U)$, for the reflective discharge with cold cathodes can be obtained from Eq. (3) by assuming that $J_{em} = 0$, which corresponds to the absence of thermionic emission from cold cathodes. Figure 2 gives several examples of such curves for E_i = 40 eV. Evidently, these curves correspond to a small current of the reflective discharge (low-current regime) with cold cathode, which not only is determined by processes in the discharge but also depends on the parameters of the external circuit and the voltage source.

In the B–U plane, the region of existence of the reflective discharge with self-heated cathode is bounded from above by the $B(U)$ curve, exhibiting a clear minimum corresponding to the critical magnetic induction B_{cr}. The position of this curve is determined primarily by the discharge cell geometry and the ion–electron emission coefficient γ.

As can be seen from the current–voltage characteristic for $B < B_{cr}$ (Fig. 1), the standard discharge with self-heated cathode can be self-sustained in a broad range of voltages. This discharge regime is especially useful in devices intended for operation in a broad range of current densities [3, 5]. The current–voltage characteristics of Penning discharge with self-heated cathode exhibit negative differential resistance typical of the arc discharge. This is a natural result, because these discharges feature the same mechanism of electron emission determined by the high cathode temperature. In the limiting case of a very high current, the current–voltage characteristics cease to depend on the magnetic induction, which corresponds to the usual arc discharge.

Acknowledgments. The authors are grateful to V.A. Kagadeĭ and G.E. Ozur for stimulating and fruitful discussions.

REFERENCES

1. M. D. Gabovich, *Physics and Technology of Ion Plasma Sources* (Atomizdat, Moscow, 1972) [in Russian].
2. Yu. E. Kreĭndel', *Plasma Sources of Electrons* (Atomizdat, Moscow, 1977) [in Russian].
3. A. P. Semenov, *Sputtering Ion Beams: Production and Application* (Izd. BNTs SO RAN, Ulan-Ude, 1999) [in Russian].
4. S. P. Nikulin, Zh. Tekh. Fiz. **68** (7), 56 (1998) [Tech. Phys. **43**, 795 (1998)].
5. V. A. Kagadeĭ, A. V. Kozyrev, I. V. Osipov, *et al.*, Zh. Tekh. Fiz. **71** (3), 22 (2001) [Tech. Phys. **46**, 292 (2001)].

Translated by P. Pozdeev

Technical Physics Letters, Vol. 30, No. 8, 2004, pp. 675–676. Translated from Pis'ma v Zhurnal Tekhnicheskoĭ Fiziki, Vol. 30, No. 16, 2004, pp. 26–30.

Parameters of a Noisy Lorenz System Reconstructed Using the Method of Proper Coordinates

V. V. Afanasiev*, R. R. Nigmatullin, and Yu. E. Polsky

Kazan State Technical University, Kazan, Tatarstan, Russia

** e-mail: vafv@kstu-kai.ru*

Received February 25, 2004

Abstract—Parameters of a noisy Lorenz system were reconstructed from its time series using the method of proper coordinates. The effects of low- and high-frequency additive and multiplicative noise on the relative error of reconstruction of the system parameters have been studied. It is demonstrated that the method of proper coordinates provides for increased accuracy of reconstruction of the Lorenz system parameters in the presence of additive noise. © *2004 MAIK "Nauka/Interperiodica".*

Nonlinear systems featuring dynamical chaos are widely used for secret data transmission and in communication systems using dynamical chaos as a source of oscillations bearing information [1]. Important prerequisites for the creation of effective data transmission systems of this type is the possibility of identification of nonlinear systems generating chaotic signals and reconstruction of the parameters of nonlinear systems in the presence of internal and external noise.

An effective means of determination of the parameters of noisy structures described by systems of nonlinear differential equations is offered by the method of proper coordinates [3]. Using this method, it is possible to transform functions of the $y(x, V)$ type (where x is an independent variable and V is the vector of initial parameters) into relations

$$Y(x) = C_1(V)X_1(x) + \ldots + C_k(V)X_k(x) \qquad (1)$$

via differential equations satisfied by the y functions. Relations (1) allow the vector V to be reconstructed using the realizations of processes generated by the given nonlinear system without analytically solving the initial systems of nonlinear differential equations. Evaluation of the parameters of nonlinear systems with the aid of the method of proper coordinates is performed through transformation of the differential equations into integral equations, followed by an original linear regression procedure [3].

This paper reports on the results of investigation of the possibility of using the method of proper coordinates for reconstruction of the parameters of a noisy system with dynamical chaos. For this purpose, we have used the well-known dynamical system of the Lorenz type,

$$\dot{X} = -\sigma X + \sigma Y, \quad \dot{Y} = -XZ + rX - Y, \quad \dot{Z} = XY - bZ, \qquad (2)$$

where X, Y, and Z are the variables and r, σ, and b are the system parameters [2]. Equations (2) describe the formation of chaotic signals and the course of dynamical processes in various multimodal nonlinear devices and systems.

Using numerical simulation methods, we have studied the effect of noise on the quality of parameters of dynamical system (2) reconstructed from the time series of X, Y, and Z variables generated by numerical integration of system (1) using the Euler method. The additive and multiplicative noise was introduced into the model as described by the equations

$$\begin{aligned} \dot{X} &= \sigma(1 + m_\sigma)(Y - X) + u_x X_0, \\ \dot{Y} &= -XZ + r(1 + m_r) + X - Y + u_y Y_0, \\ \dot{Z} &= XY - b(1 + m_b)Z + u_z Z_0. \end{aligned} \qquad (3)$$

Here, the quantities m_σ, m_r, and m_b determine the relative intensity of the multiplicative noise (fluctuations of the system parameters) with respect to the values of r, σ, and b, while the quantities u_x, u_y, and u_z determine the relative intensity of the additive noise with respect to the values of X_0, Y_0, and Z_0 in the state of equilibrium ($X_0 = Y_0 = \sqrt{b(r-1)}$, $Z_0 = r - 1$ [2]). The m and u values were simulated using random number generators.

Parameters of the model Lorenz system ($r = 28$, $\sigma = 10$, $b = 8/3$) were selected so as to ensure the regime of dynamical chaos with a strange attractor [2]. We have reconstructed the system parameters using two methods and performed comparative analysis of the results.

The first method, providing a basis for comparison of the accuracy of reconstruction of r, σ, and b, is based

Reconstruction of parameters of the noisy Lorenz system using the method of proper coordinates (I) and the Euler method (II)

Noise		Average noise intensities (%) for which the relative error of reconstruction is <1.5%					
		σ		*r*		*b*	
		I	II	I	II	I	II
HF noise	*m*	0.5	2	3	5	4	6
	u	0.075	0.025	1.5	0.3	2	0.4
LF noise	*m*	0.3	1.5	2	3	2.5	4
	u	0.002	0.00065	0.025	0.008	0.07	0.02

on evaluation of the parameters $\tilde{\sigma}$, $\tilde{r}$, and $\tilde{b}$ using Eqs. (2) according to the Euler method:

$$\tilde{\sigma} = \frac{1}{N}\sum_i \frac{x_{i+1}-x_i}{h(y_i-x_i)}, \quad \tilde{r} = \frac{1}{N}\sum_i \frac{\dfrac{y_{i+1}-y_i}{h} + x_i z_i + y_i}{x_i}, \quad \tilde{b} = \frac{1}{N}\sum_i \frac{x_i y_i - \dfrac{z_{i+1}-z_i}{h}}{z_i}. \tag{4}$$

Here, X_i, Y_i, and Z_i are the values of time series of the system variables on the Ith step ($I = 1, \ldots N$) and h is the step of numerical integration. The second method of reconstruction of the Lorenz system parameters is based on the method of proper variables [3].

During simulation of the time series of X_i, Y_i, and Z_i, the N value was no less than 10^4 and the h value did not exceed 1% of the period of quasi-resonance oscillations in the Lorenz system [4]. In order to determine the influence of the noise spectrum on the reconstruction of parameters of the dynamical Lorenz system, we compared the effects of the initial noise in Eqs. (3) and the noise obtained by its low-frequency filtration. The accuracy of reconstruction was evaluated by the relative errors of $\tilde{\sigma}$, $\tilde{r}$, and $\tilde{b}$.

Data on the average m and u noise intensities (in %) for which the relative error of reconstruction of the Lorenz system parameters does not exceed 1.5% are presented in the table, where values I were obtained by the method of proper coordinates and values II refer to the method using Eqs. (4).

As can be seen from the data in the table, the method of proper coordinates increases the accuracy of restoration of the parameters of the dynamical Lorenz system in the presence of additive noise by a factor of 3–5 as compared to the method using Eqs. (4). The low-frequency (LF) noise influences the accuracy of restoration stronger than the high-frequency (HF) noise, which is related to the inertial character of processes in nonlinear devices and systems with chaotic dynamics. It should also be noted that the inertia in the dynamical Lorenz system depends nonlinearly on the amplitude of oscillations of the *X*, *Y*, and *Z* variables [5]. For this reason, the degree of noise influence depends on the number of transitions of the phase trajectory of the Lorenz system between the regions with different equilibrium states in the phase space. For the multiplicative noise, the method based on Eqs. (4) is advantageous only in the case of a noise with zero mean. On the other hand, this method is characterized by anomalous errors related to the fact that some values of $(X_i - Y_i)$, Y_i, and Z_i in the time series of processes generated by the Lorenz system are close to zero.

In order to check the reliability of results, the reconstruction of the Lorenz system parameters based on the method of proper coordinates was used for an analysis of the X_i, Y_i, and Z_i time series generated by nonlinear systems (Duffing and van der Pol oscillators, fractal Brownian motion) basically different from the Lorenz system. The obtained $\tilde{\sigma}$, $\tilde{r}$, and $\tilde{b}$ estimates have proved to be physically unrealizable in the Lorenz system and were characterized by anomalous shapes of the regression relations obtained by the method of proper coordinates. This fact points to the principal possibility of using the method of proper coordinates for identification of a given system in a set of several nonlinear systems.

Conclusions. (i) Using the method of proper coordinates, it is possible to identify nonlinear systems and reconstruct their parameters from the realizations generated by these systems in the regime of dynamic chaos with strange attractors.

(ii) The method of proper coordinates increases the accuracy of restoration of the parameters of the dynamical Lorenz system in the presence of additive noise by a factor of 3–5 as compared to the Euler method.

REFERENCES

1. A. S. Dmitriev and A. I. Panas, *Dynamical Chaos: New Communication Facilitates* (Fizmatlit, Moscow, 2002) [in Russian].
2. A. J. Lichtenberg and M. A. Lieberman, *Regular and Stochastic Motion* (Springer-Verlag, New York, 1982; Mir, Moscow, 1984).
3. R. R. Nigmatullin, Appl. Magn. Reson. **14**, 601 (1998); Physica A **285**, 547 (2000); M. Al-Hasan and R. R. Nigmatullin, Renewable Energy **28**, 93 (2003).
4. V. V. Afanasiev, S. V. Mikhaĭlov, Yu. E. Polsky, and A. Yu. Toropov, Pis'ma Zh. Tekh. Fiz. **21** (23), 10 (1995) [Tech. Phys. Lett. **21**, 953 (1995)].
5. V. V. Afanasiev and Yu. E. Polsky, Vestn. Kazansk. Gos. Tekh. Univ. im. A. N. Tupoleva, No. 1, 1 (1997).

Translated by P. Pozdeev

Technical Physics Letters, Vol. 30, No. 8, 2004, pp. 677–678. Translated from Pis'ma v Zhurnal Tekhnicheskoĭ Fiziki, Vol. 30, No. 16, 2004, pp. 31–35.

Molecular-Dynamics Study of Nanofragmentation during Relaxation in After-Loaded Solids

A. I. Dmitriev* and S. G. Psakhie

Institute of Strength Physics and Materials Science, Siberian Division, Russian Academy of Sciences, Tomsk, 634055 Russia

** e-mail: dmitr@usgroups.com*

Received March 16, 2004

Abstract—The possibility of nanofragmentation development during the initial relaxation stage in the subsurface layer of a solid after preliminary loading is studied by computer simulation using the molecular dynamics method. It is established that disoriented nanoblocks can form in the initial stage of relaxation. This fragmentation arises in the region of strain localization in the vicinity of stress concentrators and then spreads in depth of the material. In the region of strain localization, the radial distribution function (RDF) of atomic density exhibits smeared maxima corresponding to peaks in the RDF of the ideal fcc crystal structure. In the crystal region free of strain localization, the RDF peaks exhibit splitting caused by the strain-induced symmetry breakage. The obtained results suggest that fragmentation is the possible mechanism of relaxation of internal stresses in loaded solids. *© 2004 MAIK "Nauka/Interperiodica".*

The knowledge of elementary events and mechanisms involved in the development of plastic deformation in solids is among the key aims of investigations in materials science and the physics of strength and plasticity. In addition to the classical mechanisms, modern physical mesomechanics also recognizes the very important role of fragmentation processes involving the rotational deformation mode [1–3]. It was demonstrated [3] that, in the analysis of these processes, it is necessary to take into account the influence of the surface as a special state of solids. Such phenomena are usually studied in the stage of active loading. However, the characteristic rates of related processes are rather low, which makes possible their realization in the initial stages of relaxation or upon a change in the regime of straining (for example, during fatigue loading). For this reason, it is also necessary to study the possible fragmentation of materials in the initial relaxation stage. Experimental investigations of such phenomena encounter considerable difficulties related to their extremely small temporal and spatial scale.

In this context, we used the molecular dynamics method to study the features of plastic deformation near the free surface of a model solid in the initial stage of relaxation, that is, immediately after termination of the stage of active loading.

We have simulated the behavior of a copper crystal in response to preliminary mechanical loading. The model crystal, having the shape of a parallelepiped with edges parallel to the crystallographic directions [100], [010], and [001], comprised three regions. The central region represented a freely strained part of the crystal, while the boundary planar regions parallel to the (001) plane simulated the external action. In this study, the boundary regions realized the so-called string boundary conditions [4] with fixed values of the projections of atomic velocities onto the [001] direction. The behavior of atoms in the other directions was not preset and was determined by the corresponding atomic environment. In order to take into account the extension of the model crystal, we used periodic boundary conditions in the [010] direction and simulated free boundaries in the [100] direction. The interatomic interactions were described within the framework of the method of embedded atom [5, 6].

In order to avoid the induced effects related to the symmetry of the ideal crystal lattice, the model copper crystal was heated to 20 K. The load was applied when the atomic structure attained the equilibrium state corresponding to this temperature. Initially, the model crystal was subjected to compression by displacing the boundary regions in the opposite directions at a velocity of 50 m/s. The loading was continued until reaching various degrees of straining and then the crystal was allowed to relax.

Detailed investigation of the relaxation process was performed by tracing the time evolution of atomic configurations and constructing the radial distribution functions (RDFs) of atomic density [7]. The results of our investigation showed that relaxation of the model crystal is accompanied by the formation and development of strain localization bands. Detailed analysis showed that these bands originate at the free surface, from sources in the vicinity of stress concentrators occurring in the middle parts of free surfaces and at the interfaces between the central strained region and the boundary regions simulating the external load. This is illustrated in Fig. 1, which shows the structure of the

1063-7850/04/3008-0677$26.00 © 2004 MAIK "Nauka/Interperiodica"

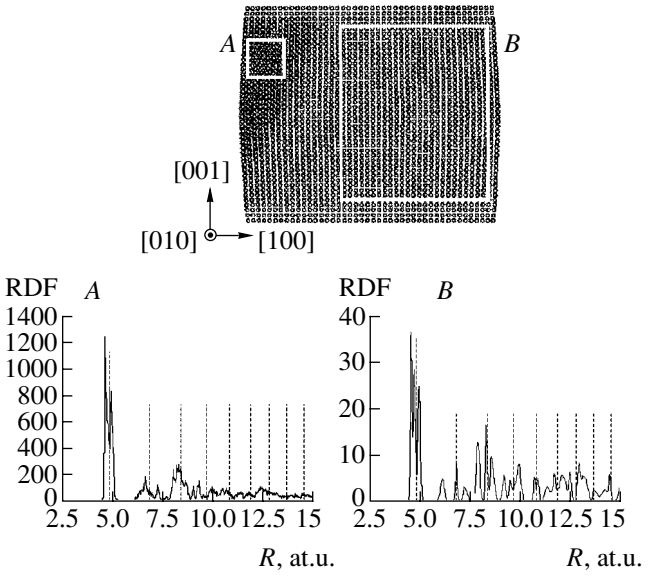

Fig. 1. The atomic structure and the RDF functions of atomic density in regions *A* and *B* of the model crystal at the moment corresponding to the onset of a strain localization band. The dashed lines indicate the positions of RDF peaks corresponding to the ideal fcc crystal lattice. The atomic unit of length corresponds to 0.529177×10^{-10} m.

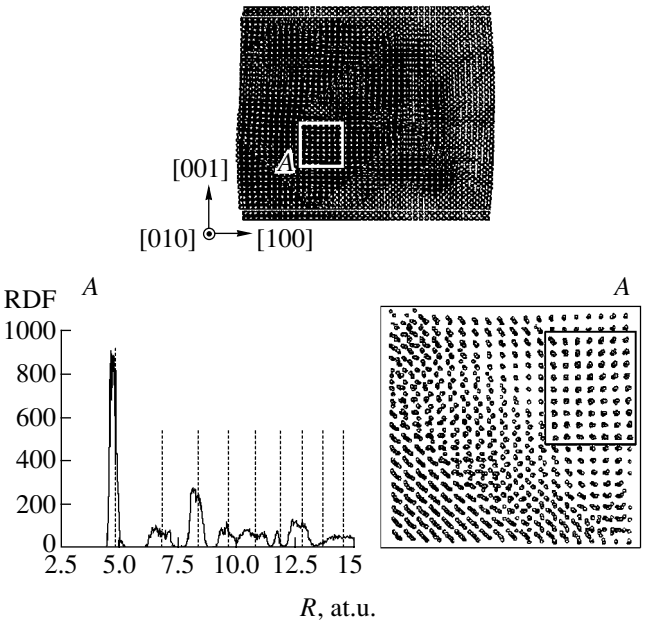

Fig. 2. The atomic structure and the RDF function of atomic density in region *A* of the model crystal in the fragmentation stage. The frame in the structure of region *A* shows one of the nanoblocks formed as a result of fragmentation.

model crystal at the moment corresponding to the onset of formation of the strain localization band. As can be seen, the band originates at the surface and then spreads in depth of the material. A thorough analysis of the RDF of atomic density in various parts of the model crystal showed that the formation of the strain localization band is accompanied by rearrangement of the atomic structure. Figure 1 shows that the initial "split" RDF peaks observed for a strained crystal lattice exhibit transformation in the localized strain region into smeared maxima corresponding to peaks in the RDF of the ideal fcc crystal structure.

Further analysis of the relaxation process elucidated the mechanism of rearrangement of the atomic structure. Figure 2 shows the model crystal structure in the subsequent moment of time, from which it is seen that fragmentation has spread virtually over the whole crystal. Thus, the process of plastic straining in the relaxation stage can proceed via the formation of disoriented crystalline nanoblocks. Each fragment has an fcc structure, as evidenced by the RDF function of one of the blocks presented in Fig. 2. The smearing of the RDF peaks (corresponding to peaks in the RDF of the ideal fcc crystal structure) is explained by the existence of boundaries between nanoblocks and by the mutual influence of these blocks.

Acknowledgments. This study was supported in part by the Presidential Program of Support for Leading Scientific Schools in Russia (project no. NSh-2324.2003.1), the Ministry of Education of the Russian Federation (project no. PD02-1.5-425), the Russian Science Support Foundation, and the U.S. Civilian Research and Development Foundation for the Independent States of the Former Soviet Union (CRDF grant no. TO-016-02).

REFERENCES

1. *Physical Mesomechanics and Computer Design of Materials*, Ed. by V. E. Panin (Nauka, Novosibirsk, 1995), pp. 297, 320 [in Russian].
2. V. E. Panin, Fiz. Mezomekh. **4** (3), 5 (2000).
3. V. E. Panin, V. M. Fomin, and V. M. Titov, Fiz. Mezomekh. **6** (2), 5 (2003).
4. A. I. Mel'ker, A. I. Mikhaĭlin, and E. Ya. Baĭguzin, Fiz. Met. Metalloved. **64**, 1066 (1987).
5. K. P. Zol'nikov, T. Yu. Uvarov, and S. G. Psakhie, Pis'ma Zh. Tekh. Fiz. **27** (7), 1 (2001) [Tech. Phys. Lett. **27**, 263 (2001)].
6. S. G. Psakhie and K. P. Zol'nikov, Pis'ma Zh. Tekh. Fiz. **23** (14), 43 (1997) [Tech. Phys. Lett. **23**, 555 (1997)].
7. V. A. Polukhin, V. F. Ukhov, and M. M. Dzugutov, *Computer Simulation of Dynamics and Structure of Liquid Metals* (Nauka, Moscow, 1981) [in Russian].

Translated by P. Pozdeev

Technical Physics Letters, Vol. 30, No. 8, 2004, pp. 679–681. Translated from Pis'ma v Zhurnal Tekhnicheskoĭ Fiziki, Vol. 30, No. 16, 2004, pp. 36–40.

Electrooptics of Hybrid Aligned Nematics in the Regime of Flexoelectric Instability

V. A. Delev and O. A. Skaldin*

Institute of Molecular and Crystal Physics, Russian Academy of Sciences, Ufa, Bashkortostan, Russia

** e-mail: delev@anrb.ru*

Received November 24, 2003

Abstract—Flexoelectric instability was observed in a hybrid aligned nematic liquid crystal layer with the director having planar orientation at one substrate and homeotropic at the other substrate. The threshold and contrast characteristics of the electrooptical cell and the differential flexoelectric coefficient $e = e_{11} - e_{33}$ for this configuration were determined. The e value is in good agreement with theoretical predictions and experimental data obtained by different methods. © *2004 MAIK "Nauka/Interperiodica"*.

The flexoelectric effect in nematic liquid crystals (NLCs) is caused by the linear relation between orientational deformation of the director **n** and the electric polarization **P** [1]. In planar NLC layers, the development of flexoelectric instability leads to a static periodic spatial deformation of the director field. This is manifested by the appearance of a domain structure, in which the domain lines parallel to the initial director. Such domains were originally described by Vistin [2] and their flexoelectric nature was established in subsequent experimental [3, 4] and theoretical investigations [5, 6].

Cholesteric liquid crystals and twist NLC layers also exhibit flexoelectric instability [7, 8], which differs from that developed in the liquid crystal layers with planar orientation of the director. The differences are related to inhomogeneity (twist structure) of the director field. The standard liquid crystal geometries with planar and homeotropic director orientations were theoretically studied by Derzhanski *et al.* [9–11]. At the same time, investigations of NLC layers with hybrid orientations are almost unstudied, although such systems may feature the flexoelectric effect coexisting with various orientational instabilities such as the nonthreshold Fréedericksz effect and electroconvection [12]. It should be emphasized that information of this kind can be can be of considerable value for application in an electrooptical system based on liquid crystals.

This study was aimed at determining the electrooptical characteristics of hybrid aligned NLC layers in the regime of flexoelectric instability.

We studied NLC crystals based on 4-*n*-methoxybenzilidene-*n*-butylaniline (MBBA) prepared by casting MBBA solution between glass plates bearing transparent SnO_2 electrodes. The NLC layer thickness could be varied by placing mylar spacers of different preset thicknesses between the substrates. The planar orientation of the director was provided by rubbing the substrate in one direction or by oblique deposition of silicon oxide. The homeotropic orientation was spontaneously formed after treatment of the substrate surface with ethanol. The influence of the NLC layer thickness on the flexoelectric effect was determined using cells prepared with spacer thicknesses d = 13, 23, and 40 μm. The lateral cell dimensions were 1 × 1.5 cm. All measurements were performed at $T = 25 \pm 0.1$°C.

The domain structures were observed with an Amplival-Pol.U polarization microscope (Carl Zeiss, Jena), recorded using a video camera, and digitized by a framegrubber with 512 × 512-pixel resolution and 256 gray levels. During the measurements, the applied dc bias voltage was varied from $U = 0$ V to $U > U_c$ with a step of $\Delta U = 50$ mV. The measurements at each bias voltage were performed after equilibration of the sample for 3 min (the characteristic time of relaxation processes in the NLC samples was ≈1–10 s). The digitized images were stored, processed, and displayed on a computer.

The image contrast was calculated by the formula

$$K = \left\langle \sqrt{\frac{1}{512}\sum_{i=1}^{512}\left(\frac{I_{ij}}{I_j^{\mathrm{av}}} - 1\right)^2} \right\rangle,$$

where I_{ij} is the intensity of Ith pixel in the jth line, I_j^{av} is the average intensity of the jth line, and angle brackets denote averaging over various lines. We determined the contrast using 100 lines in each recorded image. The period of domain structures was determined by Fourier transformation of digitized images obtained at a threshold voltage.

Let us consider the structural and phase transformations in the NLC cells studied. Figure 1 shows the pattern of flexoelectric domains in a hybrid aligned NLC layer. The domains are oriented in the direction parallel to the initial director at the substrate with planar orien-

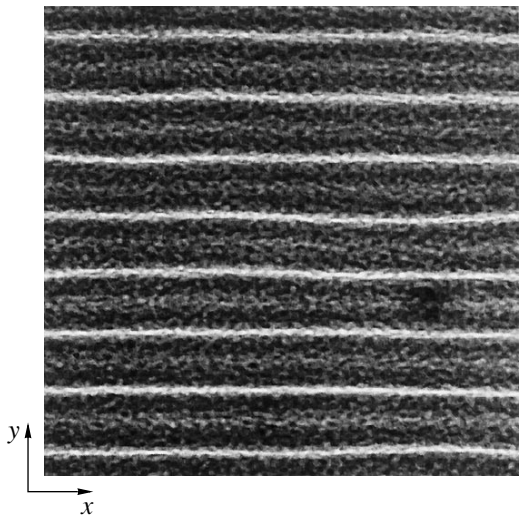

Fig. 1. The pattern of flexoelectric domains in a hybrid aligned MBBA-based NLC layer near the threshold voltage $U_c = 2.4$ V.

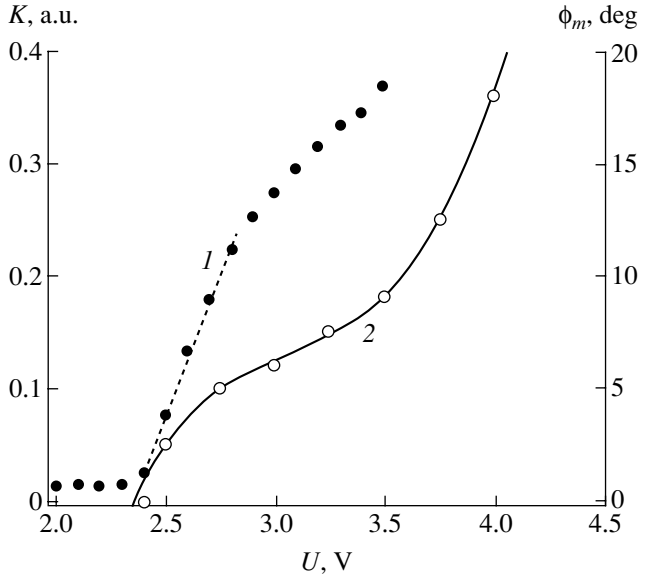

Fig. 2. Plots of (*1*) the contrast K and (*2*) the angle ϕ_m of the director deviation from the *XOZ* plane versus applied dc bias voltage U.

tation. This pattern of longitudinal domains was obtained with the polarizer and analyzer parallel to the director (X axis) at the bottom surface of the NLC layer. The threshold voltage U_c for the longitudinal domain formation was $U_c = 2.4$ V (Fig. 2), regardless of the bias voltage polarity and the NLC cell thickness. The period λ of the domain structure increased in proportion to the cell thickness: $\lambda/d = 2.5 \pm 0.1$.

Observation of the behavior of impurity particles showed that they are immobile when the bias voltage reaches the flexoelectric instability threshold. This is indicative of a stationary character of deformation of the director field. As the voltage increases to $U \approx 2.74$ V, the impurity particles begin to rotate in the direction perpendicular to the axes of longitudinal domains, which is evidence of a hydrodynamic flow arising inside the flexoelectric domains. The results of the optical polarization analysis sowed that the director deviates from the *XOZ* plane corresponding to the initial orientation. The angle of deviation was determined as follows. The NLC cell was fixed on the table of the polarization microscope and crossed Nicol prisms were rotated with a 1° step relative to the direction of initial planar orientation of the director at the bottom substrate. Then, the intensity profiles in the *Y* axis direction were compared using images averaged over 100 lines. For a homeotropic director orientation at the upper substrate, the polarization of the transmitted light is parallel to the director orientation **n** in the middle of the NLC layer. Thus, the intensity reaches maximum when the analyzer axis coincides with the director **n**. Figure 2 shows the dependence of the angle of the director deviation from the *XOZ* plane (the plane of initial director orientation in the hybrid aligned cell) on the applied voltage. When the bias voltage reaches $U_{2c} = 5.8 \pm 0.1$ V, an electrohydrodynamic instability develops inside the flexoelectric domains and the Williams domains moving in the *X* axis direction are observed [12].

Selecting the flexoelectric coefficient $e = 1.7 \times 10^{-11}$ C/m (close to the experimental value recently reported in [13]) and using the MBBA parameters in the single-constant approximation ($K = 6.5 \times 10^{-12}$ N/m, $\varepsilon_\alpha = -0.53$), we obtain $\mu = \varepsilon_0\varepsilon_\alpha K/e^2 = -0.1$ [12]. This corresponds to a threshold voltage of the flexoelectric domain formation of $U_c = 2.7$ V and a period of $\lambda = 2.1d$, which are close to the values obtained in our experiments. When the applied voltage is increased further, the electroconvection suppresses the flexoelectric instability.

Thus, we have observed for the first time the flexoelectric instability development in the form of longitudinal domains in a hybrid aligned MBBA-based NLC layer. It was established that the threshold voltage of the longitudinal flexoelectric domain formation is independent of the NLC layer thickness, while the spatial period increases linearly with the layer thickness. Using the obtained results, it is possible to estimate the values of flexoelectric coefficients.

Acknowledgments. This study was supported by the Federal Program "Integration" (project no. B0065) and by the Russian Foundation for Basic Research (project no. 02-02-17435).

REFERENCES

1. R. B. Meyer, Phys. Rev. Lett. **22**, 918 (1969).
2. L. K. Vistin', Dokl. Akad. Nauk SSSR **194**, 1318 (1970) [Sov. Phys. Dokl. **14**, 908 (1970)].

3. M. I. Barnik, L. M. Blinov, A. N. Trufanov, and B. A. Umanskiĭ, Zh. Éksp. Teor. Fiz. **73**, 1936 (1977) [Sov. Phys. JETP **46**, 1016 (1977)].
4. M. I. Barnik, L. M. Blinov, A. N. Trufanov, and B. A. Umanski, J. Phys. (France) **39**, 417 (1978).
5. Yu. P. Bobylev and S. A. Pikin, Zh. Éksp. Teor. Fiz. **72**, 369 (1977) [Sov. Phys. JETP **45**, 195 (1977)].
6. Y. P. Bobylev, V. G. Chigrinov, and S. A. Pikin, J. Phys. Colloq. **40**, 331 (1979).
7. B. A. Umanskiĭ, L. M. Blinov, and M. I. Barnik, Pis'ma Zh. Tekh. Fiz. **6**, 200 (1980) [Sov. Tech. Phys. Lett. **6**, 87 (1980)].
8. B. A. Umanskiĭ, V. G. Chigrinov, L. M. Blinov, and Yu. B. Pod'yachev, Zh. Éksp. Teor. Fiz. **81**, 1305 (1981) [Sov. Phys. JETP **54**, 694 (1981)].
9. A. I. Derzhanski and H. P. Hinov, J. Phys. (France) **38**, 1013 (1977).
10. A. I. Derzhanski, A. G. Petrov, and M. D. Mitov, J. Phys. (France) **39**, 273 (1978).
11. A. I. Derzhanski and A. G. Petrov, Acta Phys. Pol. A **55**, 747 (1979).
12. V. A. Delev, A. P. Krekhov, and L. Kramer, Mol. Cryst. Liq. Cryst. **366**, 2701 (2001).
13. T. Takahashi, S. Hashidate, H. Nishijou, *et al.*, Jpn. J. Appl. Phys., Part 1 **37**, 1865 (1998).

Translated by P. Pozdeev

Technical Physics Letters, Vol. 30, No. 8, 2004, pp. 682–686. Translated from Pis'ma v Zhurnal Tekhnicheskoĭ Fiziki, Vol. 30, No. 16, 2004, pp. 41–50.

Kinetic Model of the Growth of Nanodimensional Whiskers by the Vapor–Liquid–Crystal Mechanism

V. G. Dubrovskii, N. V. Sibirev, and G. E. Cirlin

Institute of Analytical Instrument Building, Russian Academy of Sciences, St. Petersburg, Russia

Ioffe Physicotechnical Institute, Russian Academy of Sciences, St. Petersburg, 194021 Russia

St. Petersburg State University, St. Petersburg, Russia

Received March 15, 2004

Abstract—A new kinetic model describing the growth of nanodimensional whiskers according to the vapor–liquid–crystal (VLC) mechanism is proposed. A self-consistent equation determining the whisker growth rate as a function of the liquid drop radius and the growth conditions is obtained. A manifold increase in the growth rate on the drop containing an activating substance as compared to the case of growth on the nonactivated crystal surface is explained. The proposed approach generalizes the phenomenological Givargizov–Chernov model and allows the functional form and the kinetic coefficients in the dependence of the growth rate on the control and energy parameters to be determined. The results of numerical calculations of the whisker growth rate as a function of the drop radius for various growth conditions are presented and compared to experimental data on the growth of nanodimensional GaAs whiskers on gold-activated GaAs(111)B surface. © *2004 MAIK "Nauka/Interperiodica".*

The growth of whiskers according to the vapor–liquid–crystal (VLC) mechanism was discovered in 1964 by Wagner and Ellis [1] in experiments with crystals growing on the surface of silicon activated by a gold layer. Subsequently, the formation and physical properties of whiskers grown in various systems have been extensively studied. The characteristic cross-sectional dimensions of whiskers reported in the 1960s–1970s were 1–10 μm [1, 2]. At present, using advanced crystal growth technologies and diagnostic methods, it is possible to obtain and study whiskers with a diameter of 10–100 nm [3]. Nanodimensional whiskers (NWs) of silicon, GaAs, and other semiconductors are promising materials for micro- and optoelectronics [3–6]. As for the theory of whisker (and NW) growth, the phenomenological Givargizov–Chernov model [2] developed in the 1970s based on the VLC mechanism is still the main model. However, this model, while satisfactorily explaining some experimental facts, cannot provide an exhaustive description of the laws of NW growth.

This study was aimed at the development of a kinetic model of NW growth describing this process in a rather general form, containing the Givargizov–Chernov model as a particular case, and determining the functional form and the kinetic coefficients of the dependence of the NW growth rate on the control and energy parameters of particular systems.

Consider a system comprising an NW of substance A with a diameter D, growing from a drop of supercooled solution of substance A in the melt ($A + B$) containing activating substance B (Fig. 1a). Supersaturation of the growth solution is created as a result of supply of component A from the gaseous phase. The gaseous phase may be either vapor or a molecular beam, depending on the method of deposition: vapor phase epitaxy (VPE) versus molecular beam epitaxy (MBE). The rate of this supply is characterized by the flux density J of component A to the drop surface. It is assumed that the binary system $A + B$ has a simple phase diagram of the Au + Si type. In such cases, the components exhibit no mixing in the solid state; above the eutectic temperature, the system comprises a binary liquid phase of $A + B(I)$ (not forming chemical compounds) in equilibrium with a solid phase of component A. According to the VLC growth mechanism, a particle (molecule) of substance A passes from the gaseous phase (vapor, indicated below by index (v)) into the liquid phase (indicated by (l)) on a part of the crystal surface (solid, indicated by (s)) covered by a drop of this liquid. The liquid phase gradually solidifies on the crystal surface and the liquid drop propagates upward [1]. The NW diameter is believed to be equal to the diameter of the liquid drop, which depends on the method of preparation of the activating substance and on the substrate temperature T. Therefore, the temperature T, the flux J of substance A, and the drop diameter D are control parameters of the growth process. The problem consists in determining the NW growth velocity $V_L = dL/dt$ as a function of these parameters.

In most cases, crystals grow from solution layer by layer [2, 7]. In such cases, the mechanism of normal growth of a face with diameter D depends on the

dimensionless parameter ID^3/v, where I is the rate of formation of two-dimensional nuclei of the crystal (solid) phase (nucleation rate) and v is the rate of their lateral growth. For $ID^3/v \gg 1$, the growth proceeds via polycenter nucleation, while $ID^3/v \ll 1$ corresponds to monocenter nucleation [7].

It is natural to assume that the growth of NWs possessing small diameters D ($Q \sim$ 10–100 nm) proceeds by means of monocenter nucleation, so that

$$V_L = \frac{\pi D^2}{4} hI, \quad (1)$$

where h is the monolayer (ML) step height [7]. To determine the nucleation rate, we use the following expression for the free energy of formation of a crystalline nucleus consisting of i molecules A in a supersaturated solution (Fig. 1b):

$$F_i = 2(ai)^{1/2} - \Delta\mu i. \quad (2)$$

Here, the first term is the energy required for the formation of a boundary of the nucleus: $a \equiv \pi\sigma(\alpha_{ls}/k_B T)^2$, α_{ls} is the energy of the liquid–crystal boundary per unit length, σ is the area occupied by a molecule of substance A on the surface, and k_B is the Boltzmann constant. The second term shows the gain of the volume energy as a result of the phase transition from liquid to solid phase: $\Delta\mu$ is the difference of chemical potentials for substance A in the solid and liquid phases (expressed in $k_B T$ units). To determine this difference, it is necessary to take into account the Gibbs–Thomson dimensional effect [2], related to the presence of an additional Laplace pressure in both the liquid drop and the NW possessing curved surfaces. For simplicity, the contact angle between the liquid drop and the solid surface is assumed to be 90° and the drop curvature is equal to that of the cylindrical NW. In this case,

$$\Delta\mu = \ln(1 + \zeta) - D_0/D, \quad (3)$$

where $D_0 = 4(\Omega_s\gamma_{sv} - \Omega_l\gamma_{lv})/k_B T$ is a quantity (with the dimensionality of length) determined by the difference of the specific surface energies at the crystal–gas (γ_{sv}) and liquid–gas (γ_{lv}) interfaces; Ω_s and Ω_l are the specific volumes per molecule of substance A in the solid and liquid phases, respectively; $\zeta = (C/C_{eq}) - 1$ is the supersaturation of the solution; C is the concentrations of substance A in the drop of solution; and C_{eq} is the equilibrium concentration of this solution. The expression for the supersaturation is written using the approximation of dilute solution; in the general case, the concentration C should be replaced by the solution activity [7]. Here and below, we assume that the gradient of concentration of substance A in the drop is small.

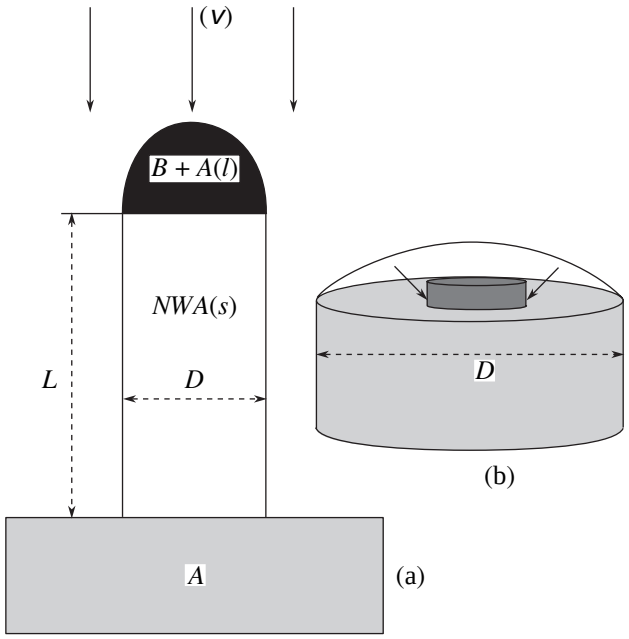

Fig. 1. Schematic diagrams illustrating (a) the NW growth of substance A (NWA(s)) from a liquid drop of the solution of A in activating substance B ($B + A(l)$) on the surface of crystal A by the VLC mechanism ($v \longrightarrow l \longrightarrow s$; the flux of substance A from the vapor phase (v) is J) and (b) the mechanism of NW growth from solution by mechanism of two-dimensional nucleation at the liquid–crystal interface. The NW is a cylinder of diameter D and height L and the two-dimensional nucleus is a disk of monoatomic height h.

Relation (2) yields the following simple expressions for the main parameters of the classical theory of nucleation [8]:

$$i_c = \frac{a}{\Delta\mu^2}; \quad F \equiv F(i_c) = \frac{a}{\Delta\mu}; \quad -F''(i_c) = \frac{\Delta\mu^3}{2a}, \quad (4)$$

where i_c is the number of molecules in the critical nucleus, F is the activation barrier for nucleation (expressed in $k_B T$ units), and $-F''(i_c)$ is the free energy of the formation of nucleus in the subcritical region. Finally, assuming that the growth of nuclei proceeds by means of the diffusion transfer of molecules from the liquid phase to a monoatomic step formed at the boundary of the nucleus [7] (Fig. 1b), using the Zeldovich formula [8] for the nucleation rate on the NW surface, and taking into account formula (4), we arrive at the following expression for the nucleation rate:

$$I = \sqrt{\frac{a}{\pi}} \frac{\Omega_l C_{eq}}{\sigma} \tau_D^{-1} (1 + \zeta) \sqrt{\Delta\mu} \exp[-F(\Delta\mu)]. \quad (5)$$

Here, $\tau_D = \nu_D^{-1}\exp[(E_D + E_B)/k_BT]$ is the average time between two sequential deliveries of molecules to the monoatomic step, E_D is the activation barrier for the diffusion of molecule A in solution, E_B is the activation barrier for the incorporation of molecule A into the monoatomic step, and ν_D is the preexponential factor (having the same order of magnitude as the frequency of thermal oscillations in the bulk of liquid).

To determine the supersaturation in the drop of solution, we use the equation of balance for the number of molecules A in the drop:

$$\frac{2}{3}\pi R^3\frac{dC}{dt} = \pi R^2\chi_{vl}J - 2\pi R^2\frac{r_lC}{\tau_A} - \pi R^2\frac{V_L}{\Omega_s}, \qquad (6)$$

where the first term on the right-hand side gives the number of molecules A adsorbed from the vapor phase on the drop surface per unit time, the second term is the number of desorption events, and the third term describes the loss of molecules A from the liquid phase as a result of crystallization. The quantity $\tau_A = \nu_A^{-1}\exp(E_A/k_BT)$ is the average lifetime of molecules A in the surface layer of the liquid, E_A is the activation barrier for desorption from the liquid surface, ν_A is the preexponential factor (having the same order of magnitude as the frequency of thermal oscillations in the bulk of liquid), χ_{vl} is the coefficient of condensation of molecules A at the vapor–liquid interface, $r_l = (3\Omega_l/4\pi)^{1/3}$, and $R = D/2$ is the drop radius. The above equation of balance is written for the case of deposition by means of MBE; in the case of VPE, the adsorption term should be doubled. An analysis of Eq. (6) shows that supersaturation rapidly reaches a stationary value, for which Eqs. (1)–(3), (5), and (6) give the self-consistent stationary equation

$$\begin{gathered}\Phi - \zeta - bd^2 f(\zeta);\\ f(\zeta) = (1+\zeta)\sqrt{\ln(1+\zeta) - 1/d}\\ \times\exp\left[-\frac{a}{\ln(1+\zeta) - 1/d}\right].\end{gathered} \qquad (7)$$

This equation contains four dimensionless parameters: a is related to the energy of the liquid–crystal interface; $d \equiv D/D_0$ is the dimensionless drop diameter; $\Phi = (\chi_{vl}\tau_A J/2r_lC_{eq}) - 1$ is the parameter determined by the balance of the adsorption–desorption processes on the drop surface; and $b = (\sqrt{\pi a}/8\sigma)(\tau_A/\tau_D)D_0^2$ reflects the ratio of the lifetime of molecules of A on the drop surface and the characteristic time of attachment to the nucleus.

According to Eqs, (1), (5), and (7), the NW growth rate is proportional to the difference of supersaturations in the gas and liquid phases,

$$V_L = V_0(\Phi - \zeta) \qquad (8)$$

with the coefficient $V_0 = 2r_l\Omega_sC_{eq}/\tau_A$.

Using Eqs. (7) and (8), it is possible to draw several general inferences concerning the character of NW growth by the VLC mechanism. First, by analogy with the Givargizov–Chernov model, allowance for the Laplace pressure in the drop and nanocrystal gives the minimum critical size below which the growth of NWs is impossible [2]. This minimum drop diameter is

$$D_{\min} = \frac{D_0}{\ln(1+\Phi)} \propto \frac{1}{T\ln J/J_0}. \qquad (9)$$

In the narrow interval of growth temperatures, the surface energies can be approximately considered as independent of the temperature. In this approximation, the minimum diameter decreases in inverse proportion to the temperature and to the logarithm of the flux of substance A to the surface.

The problem of a rate-limiting stage in the whisker growth was repeatedly discussed in the literature [2, 3, 7]. If the growth is controlled by processes at the gas–liquid interface, the supersaturation in the gas phase is significantly greater than that in the solution ($\Phi \gg \zeta$). In this case, Eqs. (7) and (8) give a trivial result: $V_L = \chi_{vl}\Omega_sJ - 2r_l\Omega_sC_{eq}/\tau_A$, which implies that the NW growth rate is determined only by the balance of adsorption–desorption processes at the drop surface. An increase in the normal growth rate on the activated part of the surface can be explained only by better adsorption and/or higher efficiency of the chemical reaction over the drop of solution, as well as by lower desorption from the drop surface as compared to that on the nonactivated surface of the crystal. In this case, NWs of various diameters grow at the same rate.

If the main role is played by processes at the liquid–crystal interface (which has numerous experimental evidence [2, 3]), the NW growth proceeds under the condition that $\Phi \approx \zeta$. In this case, it is possible to obtain an automodel solution of Eq. (7) using the sharp dependence of the nucleation rate on the supersaturation. For this purpose, $f(\zeta)$ is represented as [8]

$$f(\zeta) = f(\Phi)\exp[-\Gamma(\Phi - \zeta)], \qquad (10)$$

where $\Gamma = -(\partial F/\partial\zeta)|_{\zeta=\Phi} = i_c(\Phi)/(\Phi + 1)$ is a large parameter (on the order of the critical drop size for $\Phi = \zeta$ and not too large supersaturations). Substituting repre-

sentation (10) into Eq. (7) and taking into account (8), we obtained an automodel solution for the NW growth rate:

$$V_L = a\chi_{vl}\Omega_s J F_*^{-2} x[\beta d^2 F_*^{3/2}\exp(-F_*)]. \quad (11)$$

Here, $F_* \equiv F(\Phi) = a/[\ln(1+\Phi) - 1/d]$ is the activation barrier for nucleation at $\Phi = \zeta$, $\beta \equiv b/a^{1/2}$, and $x(U)$ is a solution of the equation

$$xe^x = U. \quad (12)$$

Equations (11) and (12) suggest two important partial cases. For relatively large $D \sim D_{\min}$, we have a strong inequality $U \ll 1$ and, hence, $x \approx U$ and the dependence of the NW growth rate on the control parameters acquires an exponential form

$$V_L \propto \exp(-F_*) = \exp\left[-\frac{a}{\ln(1+\Phi) - D_0/D}\right]. \quad (13)$$

For small D, the NW growth rate rapidly increases with the drop diameter and, at a diameter exceeding $D_{\min}$, a solution of Eq. (12) reaches the asymptote $x \approx \ln U$ beginning with $U \sim e$. In this case, the NW growth rate is described by the formula

$$V_L = \frac{\chi_{vl} J h}{\pi}\left(\frac{k_B T}{\alpha_{ls}}\right)^2\left[\ln\left(\frac{\beta a^{3/2}}{(\ln(1+\Phi) - D_0/D)^{3/2}}\left(\frac{D}{D_0}\right)^2\right) \times\left(\ln(1+\Phi) - \frac{D_0}{D}\right)^2 - a\left(\ln(1+\Phi) - \frac{D_0}{D}\right)\right]. \quad (14)$$

This expression explains why NW growth by the VLC mechanism proceeds much faster than in the absence of activating agents. According to formula (14), the NW growth rate is inversely proportional to the square of the energy α_{ls} of the liquid–crystal interface. For most substances, this value is five or six times smaller than that (α_{vs}) at the gas–crystal interface [7]. Therefore, even for equal coefficients of condensation on the liquid and crystal surfaces ($\chi_{vl} \approx \chi_{vs}$), the ratio of growth rates on the activated and nonactivated surfaces (for the same face areas) is $(\alpha_{vs}/\alpha_{ls})^2 \sim 30$. Formula (14) also explains the quadratic dependence of V_L on $\Delta\mu_* = \ln(1+\Phi) - D/D_0$ empirically introduced in the Givargizov–Chernov model. Indeed, ignoring the logarithmic dependence in formula (14) and rejecting the term linear in $\Delta\mu_*$, we obtain the Givargizov–Chernov formula $V_L = K[\ln(1+\Phi) - D/D_0]^2$ [2]. In addition, the proposed model allows us to interpret the kinetic coefficient of crystallization K. Moreover, formula (14) explains an increase in the growth velocity with the drop diameter observed in many experiments [2–7].

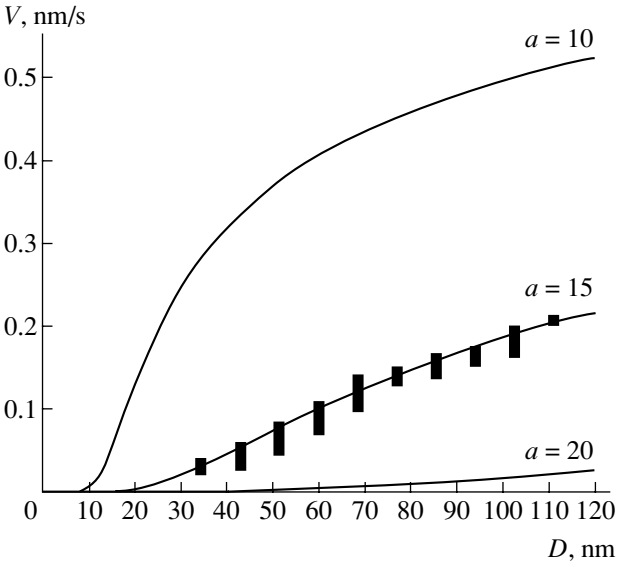

Fig. 2. Plots of the NW growth rate V versus drop diameter D calculated using Eqs. (7) and (8) for $b = 100$, $\Phi = 3$, $V_0 = 0.35$ ML/s, $D_0 = 5$ nm, and various values of $a = 10$, 15, and 20. Solid symbols show the experimental data obtained by processing scanning electron microscopy images of GaAs whiskers on gold-activated GaAs(111)B surface [9]. These GaAs whiskers were grown by MBE under the following conditions: gold layer thickness, 2.5 nm; temperature of the gold-activated surface, 610°C; GaAs layer thickness, 200 nm; surface temperature during GaAs growth, 550°C; GaAs deposition rate, 0.4 ML/s.

Figure 2 shows the results of numerical calculations of the NW growth rate as a function of the drop diameter performed using Eqs. (7) and (8) for various values of the control parameters. These numerical solutions confirm the above qualitative conclusions and agree with experimental data on the MBE growth of nanodimensional GaAs whiskers on the GaAs(111)B surface activated with gold [9]. Thus, the proposed kinetic model describes the dependence of the NW growth rate on the control parameters and explains a number of physical phenomena observed for the MW growth by the VLC mechanism. Fine processes related to the dependence of the interfacial and surface energies on the solution concentration, the transition from monocenter to polycenter nucleation, the growth from drops of controlled size, etc., will be considered in separate publications.

Acknowledgments. The authors are grateful to I.P. Soshnikov, Yu.B. Samsonenko, and A.A. Tonkikh for kindly providing experimental data and fruitful discussions and to V.M. Ustinov for his support of this study.

One of the authors (G.E.C.) gratefully acknowledges support from the Alexander von Humboldt Foundation (Germany). This study was supported in part by

the Ministry of Science and Technology of the Russian Federation and the Russian Academy of Sciences.

REFERENCES

1. R. S. Wagner and W. C. Ellis, Appl. Phys. Lett. **4** (5), 89 (1964).
2. E. I. Givargizov, *Vapor Growth of Whisker and Plate Crystals* (Nauka, Moscow, 1977) [in Russian].
3. K. Hiruma, M. Yazawa, T. Katsuyama, *et al.*, Appl. Phys. **77**, 447 (1995).
4. X. Duan, J. Wang, and C. M. Lieber, Appl. Phys. Lett. **76**, 1116 (2000).
5. Y. Cui, J. Lauhon, M. S. Gudiksen, and J. Wang, Appl. Phys. Lett. **78**, 2214 (2001).
6. B. J. Ohlsson, M. T. Bjork, M. H. Magnusson, *et al.*, Appl. Phys. Lett. **79**, 3335 (2001).
7. A. A. Chernov, E. I. Givargizov, X. S. Bagdasarov, *et al.*, in *Modern Crystallography*, Vol. 3: *Formation of Crystals* (Nauka, Moscow, 1980) [in Russian].
8. S. A. Kukushkin and A. V. Osipov, Usp. Fiz. Nauk **168**, 1083 (1998) [Phys. Usp. **41**, 983 (1998)].
9. A. A. Tonkikh, G. E. Cirlin, Yu. B. Samsonenko, and I. P. Soshnikov, Fiz. Tekh. Poluprovodn. (St. Petersburg) **38** (2004) (in press) [Semiconductors **38** (2004) (in press)].

Translated by P. Pozdeev

Technical Physics Letters, Vol. 30, No. 8, 2004, pp. 687–689. Translated from Pis'ma v Zhurnal Tekhnicheskoĭ Fiziki, Vol. 30, No. 16, 2004, pp. 51–57.

Magnetic Interaction between Superparamagnetic Particles in Nanogranular Cobalt Films

R. S. Iskhakov, G. I. Frolov, V. S. Zhigalov*, and D. E. Prokof'ev

Kirensky Institute of Physics, Siberian Division, Russian Academy of Sciences, Krasnoyarsk, Russia

** e-mail: zhigalov@iph.krasn.ru*

Received March 19, 2004

Abstract—A system of cobalt nanoparticles exhibits a transition from the superparamagnetic state into the state with cooperative magnetic ordering caused by the magnetic interaction between Co particles. It is shown that this transition can be used for obtaining nanogranular materials possessing soft magnetic properties at a large electric resistivity. *© 2004 MAIK "Nauka/Interperiodica".*

The magnetic properties of ferromagnetic (FM) nanoparticles (with diameters not exceeding 10 nm) are determined by a combination of characteristic dimensional effects: first, by the transition of particles into a monodomain state, whereby the particle size is comparable with the correlation length of exchange interaction; second, by the structural transformation accompanied either by a change in the phase state or by the formation of a complex nanostructural system comprising a "core" and a passivating "shell;" third, by the transition of the system of monodomain FM nanoparticles into a superparamagnetic state, whereby thermal fluctuations exceed the remagnetization threshold determined by the magnetic anisotropy. In other words, above a certain temperature (called the blocking temperature T_B), the ensemble of monodomain particles behaves like a gas of paramagnetic molecules possessing large magnetic moments.

In the class of nanocrystalline magnetic materials, a special position is occupied by granular nanocomposites comprising magnetic nanoparticles dispersed in a nonmagnetic matrix. Both the practical value and basic significance of such materials are determined by the fact that their magnetic properties can be controlled by varying the size and density of magnetic nanoparticles. An important role in the modification of magnetic properties of these systems is played by the magnetic interaction between particles.

Investigations of the magnetic properties of granulated systems [1–3] showed magnetic hysteresis at temperatures above the blocking temperature ($T > T_B$). This hysteresis is related to the magnetic interaction between nanoparticles, which otherwise would exhibit a purely superparamagnetic behavior. The transition from a superparamagnetic state into the state with a cooperative magnetic ordering caused by the magnetic interaction was theoretically and experimentally studied for composite materials with a magnetic phase content not exceeding 20 vol % [4–7]. However, interpretation of the magnetic properties of such systems is hindered by their complex dependence on many parameters and factors, including the dispersion of particle dimensions, the existence of various structural and magnetic phases in nanoparticles, the presence of a specific local anisotropy of nanoparticles, and the aforementioned magnetic interaction between nanoparticles. It is very difficult to establish with confidence which of these factors plays a decisive role in the formation of magnetic properties of such granular systems.

From the standpoint of practical applications, it would be of interest to study the magnetic properties of a system with a large volume fraction ($v > 40\%$) of the magnetic phase [8]. In such cases, the integral magnetic properties can be interpreted assuming a dominating role of the magnetic interaction between FM nanoparticles.

This letter presents the results of investigation of nanogranular films prepared by pulsed plasma sputtering of a $SmCo_5$ target in vacuum at a residual pressure of 10^{-6} Torr [9]. The thickness of the sample films was ~100 nm. Using these samples, we studied the effect of annealing on the structure, magnetic properties (coercive force, magnetization), and electric conductivity of nanogranular layers. The samples were annealed in vacuum at a pressure of 10^{-5} Torr with applied magnetic field of $H \sim 10^3$ Oe.

An important peculiarity of the employed technology is that the $SmCo_5$ phase is absent in the synthesized layers. This is explained by a high activity of sputtered samarium particles, which exhibit rapid oxidation in the residual atmosphere of the vacuum chamber. The data of Auger electron spectroscopy (AES) showed evidence of a considerable amount of carbon in the samples. The results of electron microscopy and X-ray diffraction measurements showed that the sample film structure comprises magnetic particles of a Co(C) solid solution with an average size of $D = 1.5$ nm surrounded

1063-7850/04/3008-0687$26.00

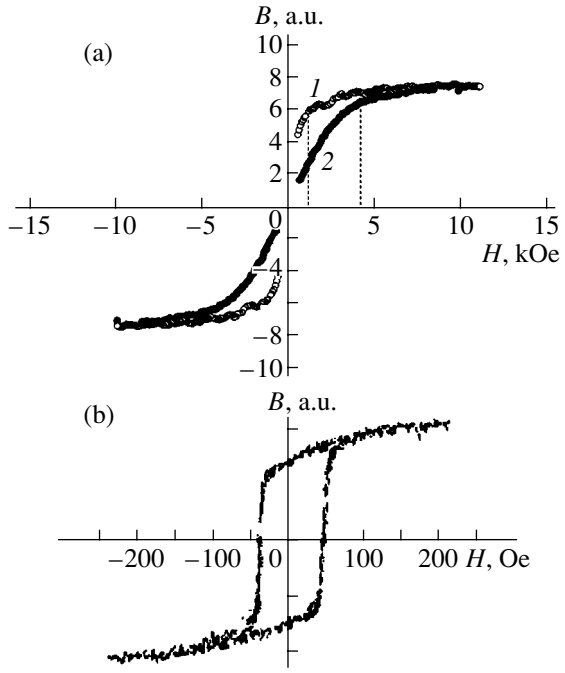

Fig. 1. Magnetization of the nanogranular films in the initial state: (a) room-temperature magnetization in the magnetic field oriented (*1*) in the sample plane and (*2*) in the perpendicular direction; (b) hysteresis loop observed at $T = 77$ K.

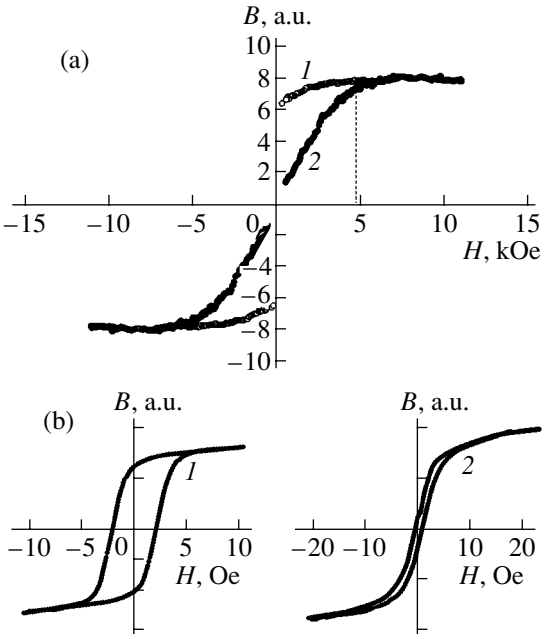

Fig. 2. Magnetization of the nanogranular films upon annealing at $T_{an} = 530$ K: (a) room-temperature magnetization in the magnetic field oriented (*1*) in the sample plane and (*2*) in the perpendicular direction; (b) hysteresis loops observed at room temperature in the directions of the (*1*) easy and (*2*) hard magnetization axis.

by samarium oxide (Sm_2O_3); the volume fraction of the magnetic phase amounted to ~60% [10]. Evidently, this morphology accounts for the relatively high resistivity of the samples ($\rho \sim 5 \times 10^{-2}$ Ω cm).

Figure 1a presents the magnetization curves measured at $T = 300$ K in the film plane (curve *1*) and in the perpendicular direction (curve *2*). Figure 1b shows the results of measurements at $T = 77$ K, which reveal a hysteresis loop. At room temperature, the magnetization curves exhibited no hysteresis, which was observed only at low temperatures ($T < T_B$). This behavior of the hysteresis loop is characteristic of a superparamagnetic material. Previously [10], it was established that the magnetic moment in such films is oriented in the sample plane. Therefore, using curve *2* in Fig. 1, it was possible to evaluate the effective saturation magnetization (~300 G).

Figure 2 presents analogous data—magnetization curves (a) and hysteresis loops (b)—for a film annealed at $T_{an} = 530$ K. The electron-microscopic examination showed that annealing did not produce any visible increase in the particle size. As can be seen, the magnetization curve *2* measured in the direction perpendicular to the sample plane remained virtually unchanged. This result suggests that the saturation magnetization also remained the same. On the other hand, there is a significant change in magnetic properties measured in the sample plane (curve *1*): the film becomes ferromagnetic and exhibits hysteresis even at $T = 300$ K ($H_C \le 3$ Oe); in addition there is evidence of a uniaxial anisotropy ($H_K \ge 10$ Oe).

To explain these changes in magnetic properties of the annealed film, let us consider the temperature dependence of the coercive force H_C (Fig. 3). This curve reveals two regions. In the region of low temperatures, H_C exhibits a sharp decrease with increasing temperature T (region I). At high temperatures, H_C varies less sharply with the temperature (region II) and turns to zero at $T = T_P$.

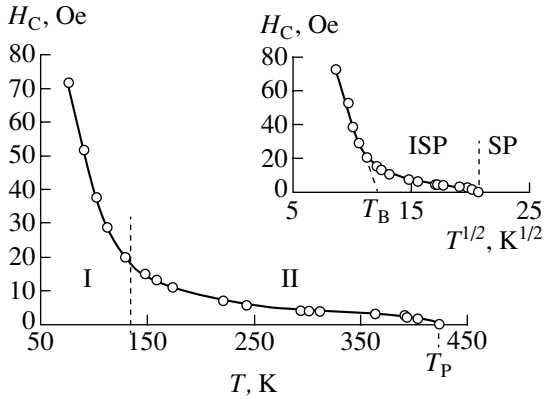

Fig. 3. Temperature dependence of the coercive force for a nanogranular film upon annealing. The inset shows the plot of $H_C = f(T^{1/2})$. See the text for explanations.

In order to interpret the behavior of $H_C = f(T)$, we use a phase diagram of the magnetic state of an ensemble of superparamagnetic particles proposed by Allia *et al.* [4]. According to this phase diagram, the $H_C = f(T)$ curve reflects the transition of our system from an FM-blocked superparamagnetic state (SP state, region I) to the state with magnetic ordering caused by the magnetic interaction between nanoparticles (region II). In the latter region, an increase in the temperature leads (instead of the usual transition from the FM to superparamagnetic state) to the appearance of an intermediate magnetically ordered state in the ensemble of superparamagnetic particles (ISP state, region II), where the material exhibits unusual magnetic properties (e.g., small coercive force H_C). In addition to the blocking temperature, the material is characterized by another critical temperature: the temperature of transition to the superparamagnetic state (T_P).

The blocking temperature can be estimated using the well-known relationship

$$H_C = H_{C0}[1 - (T/T_B)^{1/2}] \quad (1)$$

and the plot of $H_C = f(T^{1/2})$ presented in the inset in Fig. 3. The blocking temperature determined from these data is $T_B \sim 130$ K. In the interval $T_P > T > T_B$, the coercive force has a nonzero value, which is indicative of the existence of a magnetic order (region II). The magnetic energy of the ensemble of interacting magnetic nanoparticles can be expressed as [5]

$$E = KV + K_m M^2, \quad (2)$$

where K is the anisotropy constant, V is the particle volume, M is the magnetization, and K_m is the magnetic interaction constant. The system exhibits a transition to the superparamagnetic state ($H_C = 0$) at

$$T_P = K_m M^2/3k_B, \quad (3)$$

where k_B is the Boltzman constant. As can be seen from Fig. 3, in our samples, $T_P \sim 450$ K.

The magnetic and electrical properties of the samples exhibit insignificant variations depending on the conditions of synthesis and annealing. Data for the films in the initial (as-grown) state and upon annealing are presented in the table. As can be seen, the annealed films exhibit soft magnetic properties at a relatively high electric resistivity.

Thus, instead of the traditional method of obtaining magnetically soft nanocrystalline materials by means of a structural transition from the amorphous to nanocrystalline state [12], we suggest using the magnetic transition in nanogranular composites from superparamagnetic state to the state with a cooperative magnetic ordering caused by the magnetic interaction between nanoparticles. Using this method, it is possible to obtain materials with increased electric resistivity, having good prospects for use in microwave devices.

Magnetic and electrical properties of Co–Sm–O films before and after annealing

Sample	M, G	H_C, Oe (T = 300 K)	H_k, Oe (T = 300 K)	ρ, Ω cm
Initial	~300	–	–	5×10^{-2}
Annealed	~360	0.5–3	10–25	4.3×10^{-2}

Acknowledgments. The authors are grateful to S.V. Komogortsev for fruitful discussions of results and to T.N Isaev for help in conducting magnetic measurements.

REFERENCES

1. B. J. Jönsson, T. Turkbi, V. Strömetal, *et al.*, J. Appl. Phys. **79**, 5063 (1996).
2. T. Morikawa, M. Suzuki, and Y. Taga, J. Appl. Phys. **83**, 6664 (1998).
3. P. Allia, M. Coisson, M. Knobel, *et al.*, Phys. Rev. B **60**, 12207 (1999).
4. P. Allia, M. Coisson, P. Tiberto, *et al.*, Phys. Rev. B **64**, 144420 (2001).
5. S. Morup, M. B. Madsen, and J. Franck, J. Magn. Magn. Mater. **40**, 163 (1983).
6. S. Morup, Europhys. Lett. **28**, 671 (1997).
7. D. Kechrakos and K. N. Trohidon, Phys. Rev. B **58**, 12169 (1998).
8. J. R. Childress and C. L. Chen, Phys. Rev. B **43**, 8089 (1991).
9. V. S. Zhigalov, G. I. Frolov, and K. I. Kveglis, Fiz. Tverd. Tela (St. Petersburg) **40**, 2074 (1998) [Phys. Solid State **40**, 1878 (1998)].
10. G. I. Frolov, V. S. Zhigalov, S. M. Zharkov, *et al.*, Fiz. Tverd. Tela (St. Petersburg) **45**, 2198 (2003) [Phys. Solid State **45**, 2303 (2003)].
11. E. F. Kneller and F. E. Luborsky, J. Appl. Phys. **34**, 656 (1963).
12. G. Herzer, Scr. Metall. Mater. **33**, 1741 (1995).

Translated by Pozdeev

Technical Physics Letters, Vol. 30, No. 8, 2004, pp. 690–692. Translated from Pis'ma v Zhurnal Tekhnicheskoĭ Fiziki, Vol. 30, No. 16, 2004, pp. 58–64.

The First Experimental HF Heating of Plasma at Ion Cyclotron Frequencies in the Globus-M Spherical Tokamak

V. K. Gusev*, V. V. D'yachenko, F. V. Chernyshev, Yu. V. Petrov, N. V. Sakharov, and O. N. Shcherbinin

Ioffe Physicotechnical Institute, Russian Academy of Sciences, St. Petersburg, 194021 Russia

** e-mail: Vasily.Gusev@mail.ioffe.ru*

Received February 12, 2004

Abstract—We present the results of the first experiments on the HF heating of hydrogen–deuterium plasma at ion cyclotron frequencies in the Globus-M spherical tokamak. A power of 200 kW at a frequency of 9.1 MHz introduced via a single-loop antenna led to an increase in the ion temperature from 170 to 300 eV. Characteristic times of the ion temperature buildup and decay corresponded to the ion energy confinement time in the tokamak plasma. © *2004 MAIK "Nauka/Interperiodica".*

Experiments on the HF heating of plasma at ion cyclotron frequencies in the Globus-M spherical tokamak (R_0 = 0.36 m; a_0 = 0.24 m) have been under preparation for several years [1]. Two experimental scenarios were considered, according to which HF power is introduced into the tokamak plasma (i) at a cyclotron frequency of hydrogen ions present as a small impurity in deuterium plasma or (ii) at a frequency several times higher by mechanism of magnetic pumping with fast magnetoacoustic (FMA) waves. The results of preliminary modeling [2, 3] showed that the efficiency of HF wave absorption in the tokamak plasma in both cases are rather close. However, the efficiency of plasma heating can be different because the HF power is deposited in different components of the plasma. In the first case, a considerable part of the energy is spent for heating ions, while in the second case, only electrons are heated.

This Letter presents the results of the first experiments on HF heating of the tokamak plasma via hydrogen impurity in deuterium plasma for a toroidal magnetic field of 0.4 T. The plasma density at the discharge axis for a current of 250–300 kA could reach up to $4–5 \times 10^{19}$ m^{-3}.

Figure 1 shows the tokamak chamber section and the arrangement of the fundamental and higher cyclotron harmonics for hydrogen and deuterium ions at a frequency of 9 MHz in the cross section of the plasma column. The positions of these harmonics determine the localization of the energy deposition for the excited waves (*1* indicates the main resonance for hydrogen and the second harmonic for deuterium; *2*, the third harmonic for deuterium; *3*, the second harmonic for hydrogen; and *4*, an ion–ion hybrid resonance for equal fractions of deuterium and hydrogen in the plasma). This pattern was calculated assuming that the vacuum magnetic field at the axis is 0.4 T and the paramagnetic field is 0.05 T. Closed curves in Fig. 1 show the positions of the surfaces of equal magnetic flux, illustrating the magnetic field topology in the Globus-M spherical tokamak. As can be seen, some zones of the energy deposition according to this scenario unavoidably occur near the chamber walls, which can reduce the efficiency of plasma heating.

In the first stage of these experiments, HF energy was fed to the antenna at a low level (not exceeding 500 W) at an HF pulse duration up to 80 ms. This regime was used for training the antenna and finding the optimum coupling of the antenna to the plasma. Upon adjustment, the amplitude of the HF wave reflected at a high plasma density significantly decreased and the plasma was not contaminated by impurities. Then, the level of power fed to the antenna was increased to ~200 kW, the pulse duration was reduced to 20 ms, and additional training was effected until the intensity of the spectral lines of impurity ions was stabilized.

Figure 2 shows the time variation of the main plasma parameters (discharge 6736), including the discharge current, amplitudes of the incident and reflected waves, integral of the plasma density over the central vertical chord, and intensity of the D_α and CIII emission lines. In this discharge, the generator frequency was 9.1 MHz, the level of introduced power was 220 kW, and the level of reflected power was 90 kW. Therefore, the coefficient of reflection with respect to power was about 40%. As can be seen, there was a small increase in the plasma density (up to 3×10^{19} m^{-3}) during the HF pulse, but this was not accompanied by any increase in the level of plasma contamination.

1063-7850/04/3008-0690$26.00 © 2004 MAIK "Nauka/Interperiodica"

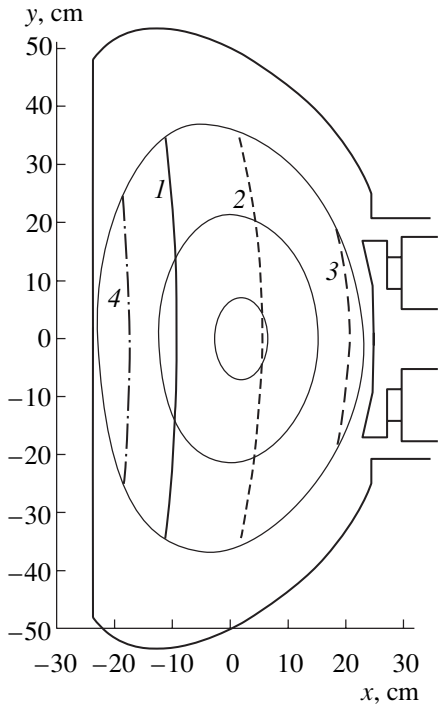

Fig. 1. Schematic diagram showing the tokamak chamber section and the positions of resonance surfaces for the excited waves: (*1*) the main resonance for hydrogen and the second harmonic for deuterium; (*2*) the third harmonic for deuterium; (*3*) the second harmonic for hydrogen; (*4*) an ion–ion hybrid resonance for equal fractions of deuterium and hydrogen in the plasma.

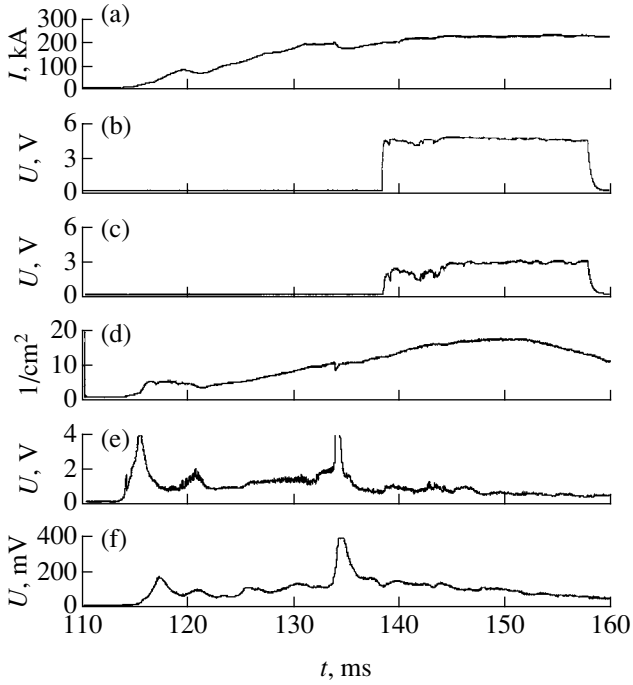

Fig. 2. Time variation of the main plasma parameters (discharge 6736): (a) discharge current; (b, c) amplitudes of the incident and reflected waves, respectively; (d) integral of the plasma density over the central vertical chord (nl/10^{14}); (e, f) intensities of the D_α and CIII emission lines, respectively.

Figure 3 shows the energy spectra of hydrogen and deuterium recharge atoms measured using an AKORD-12 atomic analyzer [4, 5]. The instrument, installed in the middle plane of the tokamak and oriented perpendicularly to the chamber axis, operated in the so-called passive regime and measured the integral spectra of atoms extracted from plasma along the detector axis. Figure 3 shows the spectra of hydrogen (*1*) and deuterium (*2*) measured 16 ms after the HF pulse front (tokamak discharge 6736) in comparison to the spectra of hydrogen (*3*) and deuterium (*4*) measured in the absence of HF heating (discharge 6739). As can be seen, only the hydrogen spectrum exhibits a "tail" of high-energy (1.1–4 keV) particles during the action of the HF pulse. This result shows evidence that deuterium is heated predominantly via hydrogen ions. It should be noted that the proportion of particles in the high-energy tail of the spectrum of hydrogen does not exceed 5% of the total number of particles contributing to the spectrum. In the "thermal" energy range (~0.25–1.1 keV), all spectra are well described by the Maxwell distribution functions with the same temperature for hydrogen and deuterium, amounting to ~300 and ~170 eV for the discharges with and without HF heating, respectively. However, no direct correlation is observed between the numbers of particles contributing to the spectra of discharges with and without HF heating: the former number is about half of the latter. This can be related to the difference in the densities of atoms in the near-wall zones of these discharges.

In order to establish a relationship between the temperature determined from the "passive" spectra of recharge atoms and the real ion temperature of the plasma, we numerically simulated the atomic flows extracted from plasma of the Globus-M tokamak. The results of this simulation performed as described in [6, 7] showed that a high-density plasma ($n_0 \approx 5 \times 10^{19}$ m^{-3}) is characterized by significantly lower atomic fluxes from the central regions. As a result, the temperature determined using the spectra of recharge atoms may be underestimated. In a simple case when the plasma temperature and density can be approximated by the parabolic distributions, the recharge spectra give an ion temperature about 20% lower than the real value in the central region. For a different (e.g., flatter) distribution of parameters observed in spherical tokamaks, the discrepancy may be even greater.

Figure 4 shows the time variation of the ion temperature (without absorption corrections) as determined from the spectra of recharge atoms measured in the tokamak discharges with and without HF heating (notations are the same as in Fig. 3). The characteristic times of buildup and decay of the ion temperature during the

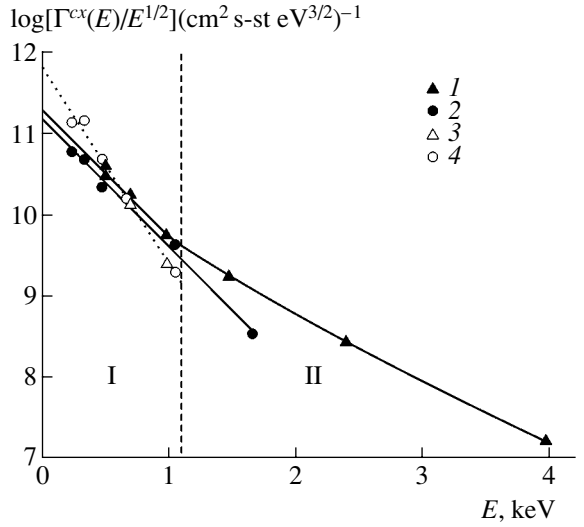

Fig. 3. The energy spectra of (*1*, *3*) hydrogen and (*2*, *4*) deuterium recharge atoms measured using an AKORD-12 atomic analyzer (*1*, *2*) 16 ms after the HF pulse (discharge 6736) and (*3*, *4*) in the absence of HF heating (discharge 6739): (I) thermal part of the spectrum; (II) high-energy tail.

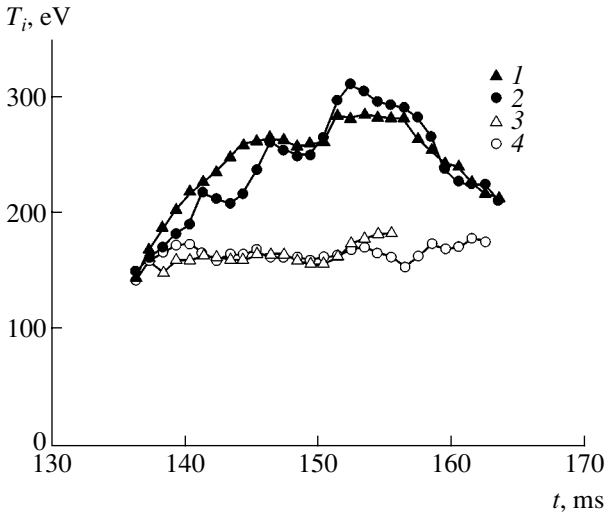

Fig. 4. Time variation of the ion temperature determined from the spectra of (*1*, *3*) hydrogen and (*2*, *4*) deuterium recharge atoms measured (*1*, *2*) with HF heating (discharge 6736) and (*3*, *4*) without HF heating (discharge 6739).

action and upon termination of the HF pulse, respectively, correspond to the ion energy confinement time the tokamak plasma. The ion temperature dynamics is virtually the same for both hydrogen and deuterium, which is indicative of a good energy exchange between the two plasma components.

It should be noted that HF heating of the plasma takes place at a rather high relative density of hydrogen ions (≈50%) measured by the same atomic analyzer. This result cannot be rationalized using the commonly accepted notions about the absorption of ion cyclotron waves in plasma, based on the data for large thermonuclear setups with large aspect ratios. In such systems, the resonance conditions are satisfied in the volume of plasma only for one harmonic. At the same time, the width of the region of nontransparency for the ion cyclotron waves at a high hydrogen density becomes very large due to a weak magnetic field gradient. Another important feature of the regime of HF plasma heating in our experiments is the relatively low limiting energy (~4 keV) of the tail of high-energy particles observed in the hydrogen recharge spectra. This (in the general case positive) effect can be related to the relatively low frequency of the HF waves employed and to the losses of ions from untrapped orbits on spherical tokamaks. We believe that limitation of the HF power contribution to the high-energy part of the ion distribution will eliminate many undesired phenomena (such as instability development, interaction with walls, etc.) related to the appearance of high-energy ion populations in tokamak plasma.

The above experimental results are important from the standpoint of basic knowledge of the physics of plasma–HW wave interaction. The proposed method of plasma heating offers greater possibilities for additional plasma heating in spherical tokamaks.

Acknowledgments. This study was supported by the Russian Foundation for Basic Research, project no. 01-02-17924.

REFERENCES

1. V. K. Gusev, V. E. Golant, E. Z. Gusakov, *et al.*, Zh. Tekh. Fiz. **69** (9), 58 (1999) [Tech. Phys. **44**, 1054 (1999)].
2. M. A. Irzak, E. N. Tregubova, and O. N. Shcherbinin, Fiz. Plazmy **25**, 659 (1999) [Plasma Phys. Rep. **25**, 601 (1999)].
3. V. V. D'yachenko, M. A. Irzak, E. N. Tregubova, and O. N. Shcherbinin, Zh. Tekh. Fiz. **73** (8), 126 (2003) [Tech. Phys. **48**, 1061 (2003)].
4. A. B. Izvozchikov, M. P. Petrov, S. Ya. Petrov, *et al.*, Zh. Tekh. Fiz. **62** (2), 157 (1992) [Sov. Phys. Tech. Phys. **37**, 201 (1992)].
5. http://www.ioffe.rssi.ru/ACPL/npd/npa00.htm.
6. Yu. N. Dnestrovskij, S. E. Lysenko, and A. I. Kislyakov, Nucl. Fusion **19**, 293 (1979).
7. A. B. Izvozchikov, Candidate's Dissertation (Ioffe Physicotechnical Institute, Leningrad, 1980).

Translated by P. Pozdeev

Technical Physics Letters, Vol. 30, No. 8, 2004, pp. 693–696. Translated from Pis'ma v Zhurnal Tekhnicheskoĭ Fiziki, Vol. 30, No. 16, 2004, pp. 65–73.

Fluctuational Electromagnetic Interaction between a Moving Particle and a Flat Surface Covered with a Thin Adsorbed Film

G. V. Dedkov

Kabardino-Balkarian State University, Nal'chik, Kabardino-Balkaria, Russia
e-mail: gv_dedkov@mail.ru

Received January 23, 2004

Abstract—The effect of a thin adsorbed film on the fluctuational electromagnetic tangential force of interaction between a moving nanoparticle and a flat solid surface was theoretically studied for the first time in a nonrelativistic approximation. Particular calculations were performed for a metal film on a dielectric and for a dielectric film on a metal. In both cases, the nanoparticle is assumed to be made of a nonmagnetic metal. It is shown that, at a normal temperature, the presence of an adsorbed film may lead to an increase in the tangential friction force by one or two orders of magnitude for a certain relation between the particle distance from the surface and the film thickness. In the case of a dielectric film on a metal substrate, a decrease in the temperature is accompanied by exponential decrease in the viscous friction. For a metal film on a dielectric substrate, the tangential force exhibits a quadratic dependence on the temperature. © *2004 MAIK "Nauka/Interperiodica".*

In practical applications related to the interpretation of the interaction between the probe of an atomic force microscope (AFM) and the sample surface, an important particular case is the substrate with a permittivity $\varepsilon_s(\omega)$ covered by an adsorbed film of thickness d and permittivity $\varepsilon_a(\omega)$ (Fig. 1). Recent measurements of the viscous dissipative force in "pure" dynamic silicon–mica [1], aluminum–gold [2], and gold–gold [3] contacts were performed at room temperature in vacuum. However, a comparison of these experimental data with the values predicted by the theory of fluctuational electromagnetic interactions revealed discrepancies reaching several orders in magnitude [4–6]. These discrepancies stimulate the search for factors missing in the theory which would provide for a increase in the magnitude of fluctuational electromagnetic interactions. In particular, the role of heating (cooling) of the AFM probe by near fluctuational fields was recently considered in [7]. Another important factor can be the presence of adsorbed layers of foreign molecules. In particular, according to estimates [8], the presence of adsorbed K atoms at a concentration of 10^{18} m^{-2} on a Cu(001) surface leads to an increase in the coefficient of viscous friction between flat copper samples by seven orders of magnitude. It should be noted, however, that the estimation [8] was based on the theory of fluctuational dissipative interaction between semi-infinite media separated by a flat vacuum gap, while scanning probe microscopy (in particular, AFM) features the interaction between a nanoprobe with the curvature radius R and a flat surface. This system is more adequately described by the theory developed in [4–6].

Let us consider, for certainty, a probe moving parallel to a surface at a distance z_0. We assume that the standard conditions of applicability of the nondelayed dipole approximation are satisfied [4–6], so that $R \ll z_0 \ll c/\omega_0$, where c is the speed of light in vacuum and ω_0 is the characteristic absorption frequency of the electromagnetic spectrum. The main difference between this problem and the case of interaction between a particle and a semi-infinite medium with flat boundary consists in the need for modification of the

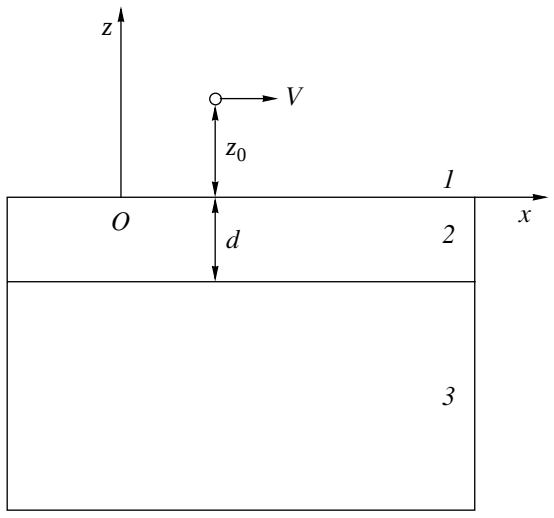

Fig. 1. Schematic diagram illustrating interaction between a particle and a surface covered by a thin adsorbed film: (*1*) vacuum; (*2*) film; and (*3*) substrate (see the text for explanations).

1063-7850/04/3008-0693$26.00 © 2004 MAIK "Nauka/Interperiodica"

solution of the Poisson equation for the Fourier component $\Phi_{\omega\mathbf{k}}(z)$ of the electric potential induced in the medium by the moving fluctuating dipole (ω is the frequency; $\mathbf{k}$ is the two-dimensional wave vector parallel to the surface; the z axis is perpendicular to the surface).

A solution for the function $\Phi_{\omega\mathbf{k}}(z)$ in this system (Fig. 1) constructed in the regions of vacuum (*1*), film (*2*), and substrate (*3*) must satisfy the conditions of continuity of the potential and the electric displacement at the boundaries $z = 0$ and $z = -d$. An analysis shows that all the general formulas [4–6] for the tangential force (F_x) and the rate of heating (dQ/dt) caused by the fluctuational electromagnetic field remain valid, provided that the dielectric response of the semi-infinite medium $\Delta(\omega) = (\varepsilon(\omega) - 1)/(\varepsilon(\omega) + 1)$ is replaced by the function

$$D(\omega, \mathbf{k}) = \frac{\Delta_1(\omega) - \Delta_2(\omega)\exp(-2kd)}{1 - \Delta_1(\omega)\Delta_2(\omega)\exp(-2kd)}, \quad (1)$$

$$\Delta_1(\omega) = \frac{\varepsilon_a(\omega) - 1}{\varepsilon_a(\omega) + 1}, \quad (2)$$

$$\Delta_2(\omega) = \frac{\varepsilon_a(\omega) - \varepsilon_s(\omega)}{\varepsilon_a(\omega) + \varepsilon_s(\omega)}. \quad (3)$$

As can be seen, formula (1) satisfies obvious limiting relations $D(\omega, \mathbf{k}) \longrightarrow \Delta_1(\omega)$ for $\varepsilon_a(\omega) \longrightarrow \varepsilon_s(\omega)$; $D(\omega, \mathbf{k}) \longrightarrow \Delta_1(\omega)$ for $d \longrightarrow \infty$; and $D(\omega, \mathbf{k}) \longrightarrow \Delta_2(\omega)$ for $d \longrightarrow 0$.

In terms of function (1), the viscous tangential force acting upon the article can be written as (negative sign corresponds to retardation)

$$F_x = -\frac{3\hbar V}{2\pi}\int\limits_{0,\infty}\int d\omega dk k^4 \exp(-2kz_0) f(\omega, k), \quad (4)$$

$$f(\omega, k) = \coth\frac{\hbar\omega}{2k_B T_1}\alpha''(\omega)\frac{dD''(\omega, k)}{d\omega} + \coth\frac{\hbar\omega}{2k_B T_2}D''(\omega, k)\frac{d\alpha''(\omega)}{d\omega}, \quad (5)$$

where $\hbar$ and k_B are the Planck and Boltzmann constants, respectively; $\alpha(\omega)$ is the dipole polarizability of the particle; T_1 and T_2 are the temperatures of the particle and the surface (in the general case, different); and primed and double-primed quantities denote the real and imaginary components. In particular, the complex polarizability of a spherical particle of radius R and permittivity $\varepsilon(\omega)$ is

$$\alpha''(\omega) = R^3 \mathrm{Im}\frac{\varepsilon(\omega) - 1}{\varepsilon(\omega) + 2}. \quad (6)$$

Using relations (1)–(3), the complex displacement can be written as

$$D''(\omega, k) = \frac{\Delta_1''(1 - a^2|\Delta_2|^2) - a\Delta_2''(1 - |\Delta_1|^2)}{1 + a^2|\Delta_1|^2|\Delta_2|^2 - 2a(\Delta_1'\Delta_2' - \Delta_1''\Delta_2'')}, \quad (7)$$

where $a = \exp(-2kd)$ and the argument ω is omitted.

In the case of a particle moving perpendicularly to the surface [9], the numerical coefficient on the right-hand side of Eq. (4) is doubled. The corresponding formula, describing the dissipative part of the normal force of interaction between a particle and the surface, contains a conservative contribution related to the standard van der Waals interaction (with dynamic corrections). The corresponding expressions can be written by analogy with formula (4).

The basic difference between formula (4) and those for the tangential interaction of a particle with a semi-infinite medium (see, e.g., [5, Eq. (4.31)] is the dependence of $D''(\omega, k)$ on the wave vector k (even without taking into account the possible nonlocal character of $\varepsilon_s(\omega)$ and $\varepsilon_a(\omega)$). In the general case, this circumstance leads to a more complicated dependence of F_x on the distance z_0, differing from the law $F_x \sim z_0^{-5}$ obtained in [4, 5].

Let us apply the above results to some particular cases.

1. Metal film on a dielectric substrate. In the microwave spectral range ($\omega \approx k_B T/\hbar$) far from the phonon resonances, we obtain $\varepsilon_a(\omega) \approx 1 + 4\pi\sigma_0 i/\omega$, where σ_0 is the static conductivity (obviously, $4\pi\sigma_0/\omega \gg 1$). Taking into account Eqs. (2) and (3), we obtain $\Delta_2'(\omega) \approx 1$, $\Delta_2''(\omega) \approx 0$, and $\Delta_1(\omega) \approx 1 + \frac{\omega}{2\pi\sigma_0} i$. Then, Eq. (7) yields

$$D''(\omega, k) \approx \frac{\omega}{2\pi\sigma_0}\frac{1 + \exp(-2kd)}{1 - \exp(-2kd)}. \quad (8)$$

When $z_0/d \gg 1$, substitution of formula (8) into Eq. (5) shows that the force F_x increases by a factor of z_0/d in comparison to the case of a "pure" surface. On the contrary, the dependence of F_x on z_0 becomes weaker ($F_x \sim z_0^{-4}$ instead of $F_x \sim z_0^{-5}$). Under the conditions of AFM experiments, the inequality $z_0/d \gg 1$ can be satisfied only for a sufficiently large distance of the point of close contact from the sample surface. At a distance on the order of 1 nm or lower, the amplification effect ceases and, hence, the presence of adsorbed layers does not (on the average) significantly influence the interaction for a probe moving perpendicularly to the surface. Note also the quadratic dependence of F_x on the temperature and a weak (if any) dependence of this force on the properties of the substrate.

2. Dielectric film on a metal substrate. In this case, $\Delta_2'(\omega) \approx -1$, $\Delta_2''(\omega) \approx 0$, and $\Delta_1(\omega) = \Delta_1'(\omega) + i\Delta_1''(\omega)$. Then, Eq. (7) yields

$$D''(\omega, k) \approx \frac{\Delta_1''(\omega)(1-a^2)}{(1+a\Delta_1'(\omega))^2 + a^2\Delta_1''(\omega)^2}. \quad (9)$$

This formula shows the possibility of a resonance for $1 + a\Delta_1'(\omega) = 0$ and $\Delta_1'(\omega) < 0$. Let $\varepsilon_a(\omega)$ have the standard form

$$\varepsilon_a(\omega) = \varepsilon_\infty\left(1 + \frac{\omega_L^2 - \omega_T^2}{\omega_T^2 - \omega^2 - i\gamma\omega}\right) = \varepsilon_\infty + \frac{\omega_T^2(\varepsilon_0 - \varepsilon_\infty)}{\omega_T^2 - \omega^2 - i\gamma\omega}, \quad (10)$$

where ε_0 and ε_∞ are the static and optical permittivities, respectively; ω_L and ω_T are the longitudinal and transverse phonon frequencies, respectively; and γ is the damping factor. Using Eqs. (2) and (10), one can readily show that the resonance condition is satisfied for two surface modes of the phonon-polariton type. The dispersion equations of these modes (with omitted terms of higher orders in small parameter $\tilde{\gamma}$) have the following form:

$$\left(\frac{\omega}{\omega_T}\right)^{(1)} = \left(p\left(1 + \frac{\tilde{\gamma}^2}{q-p}(1 + \exp(2kd)/r)\right)\right)^{1/2}, \quad 0 \le k \le k_{\max},$$

$$\left(\frac{\omega}{\omega_T}\right)^{(2)} = \left(\frac{p + qr\exp(-2kd)}{1 + r\exp(-2kd)} - \frac{\tilde{\gamma}^2}{q-p}(q + p\exp(2kd)/r)\right)^{1/2}, \quad 0 \le k \le k_{\max}, \quad (11), (12)$$

$$k_{\max}d = \frac{1}{2}\ln\left(\frac{r(q-p)^2}{\tilde{\gamma}(2\sqrt{p}(q-p) + \tilde{\gamma}(3p+q))}\right), \quad (13)$$

$$p = \frac{\varepsilon_0 + 1}{\varepsilon_\infty + 1}, \quad q = \frac{\varepsilon_0 - 1}{\varepsilon_\infty - 1}, \quad r = \frac{\varepsilon_\infty - 1}{\varepsilon_\infty + 1}, \quad \tilde{\gamma} = \frac{\gamma}{\omega_T}. \quad (14)$$

Figure 2 shows an example of dispersion relations (11) and (12) for a silicon carbide film on a metal substrate, calculated for the following parameters [10]: $\omega_T = 1.49 \times 10^{14}$ s^{-1}; $\omega_L = 1.8 \times 10^{14}$ s^{-1}; $\gamma = 8.9 \times 10^{11}$ s^{-1}; and $\varepsilon_\infty = 6.7$. In this case, formula (13) yields $k_{\max} = 1.16/d$. In the presence of a resonance at a frequency of $\omega = \omega_T x(kd)$, where $x(kd)$ is the function determined by

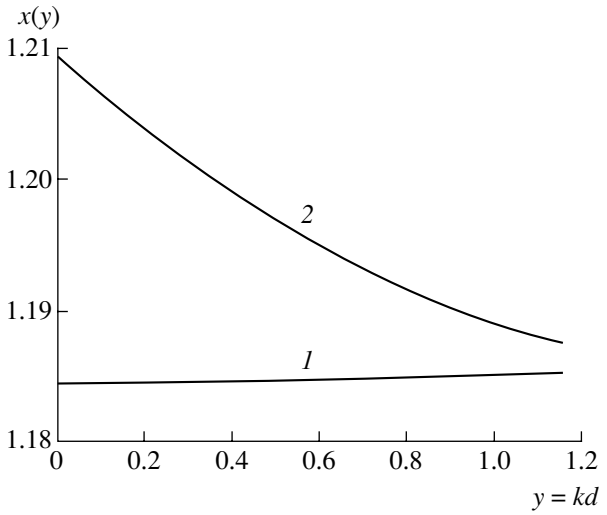

Fig. 2. Dispersion relations of the surface electromagnetic modes for a dielectric film (SiC) on metal (Au) substrate. Curves *1* and *2* correspond to formulas (11) and (12), respectively.

the right-hand sides of Eqs. (11) and (12), formula (9) can be reduced to the following form:

$$D''(\omega, k) = 2\pi sh(2kd)\frac{\delta(\omega - \omega_T x(dx))}{\left|d\Delta_1'(\omega)/d\omega\right|_{\omega = \omega_T x(kd)}}, \quad (15)$$

$$\left|\frac{d\Delta_1'(\omega)}{d\omega}\right|_{\omega = \omega_T x(kd)} = \frac{1}{\omega_T}\frac{(p - x^2)^2 + \tilde{\gamma}^2 x^2}{\left|x^2(3ar + 4) - 2ar(p + q - \tilde{\gamma}^2) - 4p + 3\tilde{\gamma}^2\right|}, \quad (16)$$

where the argument of the function $x(kd)$ is omitted. Upon substitution of formulas (6) and (15) into Eq. (4), integration with respect to the frequency is simple, and the integral with respect to the wave vector can be calculated by numerical methods. It was interesting to compare the results of calculations of the forces of interaction between a metal particle and a metal surface with and without a dielectric film. Restricting the consideration to the case of equal temperatures ($T_1 = T_2$) and equal conductivities of the particle and substrate, we obtain from Eq. (4) for the pure surface

$$F_x = -\frac{9}{32\pi}\frac{\hbar V R^3}{z_0^5}\left(\frac{k_B T}{\hbar\sigma_0}\right)^2. \quad (17)$$

Using Eqs. (4)–(6) and (15)–(17), the ratio of forces F_x for surfaces with and without an adsorbed film can be written as

$$H(\alpha, \beta) = \frac{\sigma_0}{\omega_W}Y(\alpha, \beta), \quad \alpha = \frac{z_0}{d}, \quad \beta = \frac{\omega_T}{\omega_W}, \quad (18)$$

where $\omega_W = k_B T/\hbar$ is the Wien frequency and $Y(\alpha, \beta)$ is a function determined by numerical methods (the dis-

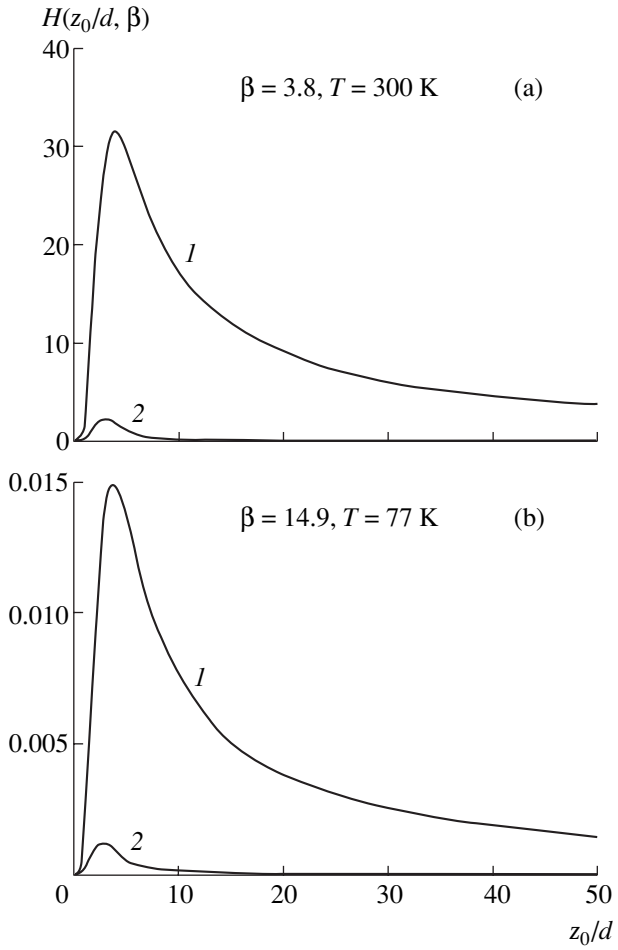

Fig. 3. The ratio of tangential forces for the interaction of a gold nanoparticle with a gold substrate with and without a silicon carbide film of thickness d at T = 300 (a) and 77 K (b). Curves *1* and *2* correspond to dispersion relations determined by formulas (11) and (12), respectively.

tance z_0 from the pure and coated surface is assumed to be the same).

Figure 3 shows the results of calculation of the ratio $H(\alpha, \beta)$ for a silicon carbide film on gold. Curves *1* and *2* correspond to the surface modes of two types determined by formulas (11) and (12). The calculation was performed for two temperatures: $T_1 = T_2 = T = 300$ K (Fig. 3a) and $T_1 = T_2 = T = 77$ K (Fig. 3b). As can be seen, the presence of a dielectric film on the metal substrate can increase the dissipative force at room temperature by one or two orders of magnitude, the maximum effect being observed for a certain relation between the distance from the particle to the surface and the film thickness (in our case, for $z_0/d \approx 3$–4). A decrease in the temperature reduces the tangential force three or four orders of magnitude (Fig. 3b). Thus, in the general case, the presence of an adsorbed film decreases the friction. This effect is related to the exponential temperature factor in Eq. (4) and the large value of parameter $\beta = \omega_T/\omega_W$ ($\beta = 14.9$ at $T = 77$ K). For dielectric films with lower values of the transverse phonon frequency ω_T (e.g., for ZnS), the temperature-induced decrease in the interaction force is less pronounced.

REFERENCES

1. B. Gotsmann, C. Seidel, B. Anczykowski, and H. Fuchs, Phys. Rev. B **60**, 11051 (1999).
2. B. Gotsmann and H. Fuchs, Phys. Rev. Lett. **85**, 375 (2001).
3. B. C. Stipe, H. J. Mamin, T. D. Stowe, *et al.*, Phys. Rev. Lett. **87**, 096801 (2001).
4. G. V. Dedkov and A. A. Kyasov, Fiz. Tverd. Tela (St. Petersburg) **44**, 1729 (2002) [Phys. Solid State **44**, 1809 (2002)].
5. G. V. Dedkov and A. A. Kyasov, Phys. Low-Dimens. Semicond. Struct. **1**–**2**, 1 (2003).
6. G. V. Dedkov and A. A. Kyasov, Fiz. Tverd. Tela (St. Petersburg) **45**, 1729 (2003) [Phys. Solid State **45**, 1815 (2003)].
7. G. V. Dedkov and E. G. Dedkova, Pis'ma Zh. Tekh. Fiz. **30** (6), 52 (2003) [Tech. Phys. Lett. **30**, 240 (2003)].
8. A. I. Volokitin and B. N. J. Persson, Phys. Rev. Lett. **91**, 106101 (2003).
9. G. V. Dedkov and A. A. Kyasov, Pis'ma Zh. Tekh. Fiz. **30** (13), 65 (2004) [Tech. Phys. Lett. **30**, 560 (2004)].
10. *Handbook of Optical Constants of Solids*, Ed. by E. D. Palik (Academic, New York, 1985).

Translated by P. Pozdeev

Technical Physics Letters, Vol. 30, No. 8, 2004, pp. 697–700. Translated from Pis'ma v Zhurnal Tekhnicheskoĭ Fiziki, Vol. 30, No. 16, 2004, pp. 74–81.

Absorption of Electromagnetic Radiation by an Inhomogeneous Cylindrical Particle

É. V. Zavitaev and A. A. Yushkanov*

Moscow State Institute of Forestry, Mytishchi-5, Moscow oblast, Russia

** e-mail: yushkanov@mtu-net.ru*

Received March 5, 2004

Abstract—The cross section for the electromagnetic radiation absorption by an inhomogeneous cylindrical particle has been calculated for an arbitrary ratio of the dielectric core radius to the particle radius. The boundary conditions correspond to the diffuse reflection of electrons from the internal and external surfaces of the metal layer. Limiting cases are considered, and the results of analysis are discussed. © *2004 MAIK "Nauka/Interperiodica".*

Introduction. The electromagnetic properties of small metal particles may significantly differ from the properties of massive samples of the same metal [1]. If the linear size R of a particle is on the order of or smaller than the electron mean free path Λ, interaction of electrons with the boundaries of the particle significantly modifies their response to an external electromagnetic field. This is manifested by special optical properties of such samples (metal particles). In particular, when the condition $R < \Lambda$ is fulfilled, one of the basic optical characteristics—the absorption cross section—exhibits an unusual dependence on the ratio R/Λ. At room temperature, the value of Λ in pure metals with good conductivity (aluminum, copper, silver, etc.) ranges from 10 to 100 nm. The dimensions of experimentally investigated particles can be as small as several nanometers; therefore, the condition $R < \Lambda$ can be readily realized.

The response of electrons to an external electromagnetic field, with allowance of their interaction with the sample boundaries, can be described within the framework of the standard kinetic theory of the electron conductivity of metals [2]. This theory poses no restrictions are imposed on the relation between the mean free path of electrons and the particle size.

The equations of macroscopic electrodynamics are applicable only to large samples, for which $R \gg \Lambda$. Therefore, the well-known Mie theory describing the interaction between electromagnetic waves and metal bodies within the framework of macroscopic electrodynamics cannot be used to describe the aforementioned size effects. Lesskis *et al.* [3, 4] developed a theory of the interaction between electromagnetic radiation and a spherical particle based on the solution of the Boltzmann equation for conduction electrons in metals.

In recent years, much attention has been devoted to the interaction of electromagnetic radiation with nonspherical particles [5]. In particular, a number of papers [6–9] reported on such interactions involving cylindrical particles. However, all the works cited above considered only homogeneous particles, in other words, ignored the internal structure of absorbing particles.

Quite recently, the results of experimental investigations involving particles with a complicated internal structure were reported in [10, 11]. The objects studied comprised a dielectric (or metal) core surrounded by a metal shell. This structure obviously influences the optical properties of particles.

We have used the aforementioned kinetic method and calculated the distribution function describing the linear response of conduction electrons in inhomogeneous cylindrical particles (comprising a dielectric core and a metal shell) to an alternating magnetic field of a plane electromagnetic wave. Using the obtained distribution function, we have calculated the absorption cross section of a particle as a function of its radius, the radiation frequency, and the ratio of the dielectric core radius to the particle radius.

Mathematical model and calculation procedure. Consider a cylindrical particle of length L, comprising a dielectric core of radius R_1 surrounded by a nonmagnetic metal shell of radius R_2 (we assume that $L \gg R_2$). The particle is exposed to the field of a plane electromagnetic wave of frequency ω bounded from above by the near-infrared range ($\omega < 2 \times 10^{15}$ s^{-1}). We assume that the direction of the magnetic field in the electromagnetic wave coincides with the cylinder axis and that the particle is small, so that $R_2 \ll 2\pi c/\omega$, where c is the speed of light in vacuum. The inhomogeneity of the external field and the skin effect are ignored ($R_2 < \delta$, where δ is the skin depth). In the frequency range under consideration, the contribution of the current of dipole electric polarization to the absorption cross section is small compared to the contribution of eddy currents induced by the external magnetic field of the wave [3].

Therefore, we do not take into account the effect of the external electric field of the wave.

The absorption of electromagnetic energy by the cylindrical inhomogeneous particle can be described as follows: a uniform periodic magnetic field $\mathbf{H} = \mathbf{H}_0\exp(-i\omega t)$ of the wave induces an eddy electric field $\mathbf{E}$ in the particle. The induced eddy electric field acts on the conduction electrons and causes deviation f_1 of their distribution function f from the equilibrium Fermi distribution f_0 (assumed to have a spherical shape). This gives rise to the eddy electric current in the particle

$$\mathbf{j} = e\int \mathbf{v} f \frac{2d^3(m\mathbf{v})}{h^3} = 2e\left(\frac{m}{h}\right)^3 \int \mathbf{v} f_1 d^3v, \qquad (1)$$

where h is the Planck constant and e, $\mathbf{v}$, and m are the electron charge, velocity, and effective mass, respectively. The energy $\overline{Q}$ dissipated per unit time is given by [12]

$$\overline{Q} = \int \overline{(\mathrm{Re}\mathbf{E})(\mathrm{Re}\mathbf{j})} d^3r = \frac{1}{2}\mathrm{Re}\int \mathbf{j}\mathbf{E}^* d^3r, \qquad (2)$$

where the upper bar denotes averaging with respect to time and the asterisk denotes complex conjugation.

The problem is reduced to finding the eddy-field-induced deviation f_1 of the electron distribution function from the equilibrium distribution f_0. In the linear approximation with respect to the external field, f_1 satisfies the kinetic equation [2, 13]

$$-i\omega f_1 + \mathbf{v}\frac{\partial f_1}{\partial \mathbf{r}} + e(\mathbf{v}\mathbf{E})\frac{\partial f_0}{\partial \varepsilon} = -\frac{f_1}{\tau}, \qquad (3)$$

where $\mathbf{r}$ is the radius vector (the coordinate origin is selected on the particle axis), τ is the electron relaxation time, and ε is the kinetic energy of electron.

Solving Eq. (3) by the method of characteristics [14], we obtain an expression for calculating the deviation f_1 of the electron distribution function from equilibrium. The boundary conditions corresponded to the diffuse reflection of electrons from the internal and external surfaces of the metal layer.

For calculating the integrals in Eqs. (1) and (2), it is convenient to pass to cylindrical variables both in the coordinate space ($r_\perp$, φ, r_z; polar axis Z is parallel to the magnetic field vector $\mathbf{H}_0$) and in the velocity space ($v_\perp$, α, v_z; polar axis is the v_z axis). The cylinder axis coincides with the Z axis.

The cross section for the absorption of electromagnetic radiation is calculated by dividing the mean dissipated power $\overline{Q}$ (see formula (2)) by the average power flux $cH_0^2/8\pi$ in the wave:

$$\sigma = \frac{1}{2}\frac{8\pi}{cH_0^2}\mathrm{Re}\{\int j_\varphi E_\varphi^* d^3r\}. \qquad (4)$$

Accomplishing the calculation, according to Eq. (4), we obtain the absorption cross section of the elongated cylindrical inhomogeneous particle, which can be presented in the following form:

$$\sigma = \sigma_0(F_1 + F_2), \qquad (5)$$

where

$$\sigma_0 = \frac{3\pi n e^2 v_f R_2^3 L}{mc^3}, \qquad (6)$$

$$F_1 = \mathrm{Re}\left\{2y^2\int_K^1 \xi^3 d\xi \times \int_0^1\int_{\alpha_0}^{\pi} \frac{\rho^3}{\sqrt{1-\rho^2}}\frac{(1-\exp(-z\eta/\rho))}{z}\sin^2\alpha d\rho d\alpha\right\}, \qquad (7)$$

$$F_2 = \mathrm{Re}\left\{2y^2\int_K^1 \xi^3 d\xi \times \int_0^1\int_0^{\alpha_0} \frac{\rho^3}{\sqrt{1-\rho^2}}\frac{(1-\exp(-z\psi/\rho))}{z}\sin^2\alpha d\rho d\alpha\right\}, \qquad (8)$$

n is the density of conduction electrons, and v_f is the Fermi velocity. Relations (7) and (8) are written in terms of the variables

$$\xi = \frac{r_\perp}{R_2},\ \rho = \frac{v_\perp}{v_f},\ K = \frac{R_1}{R_2},\ z = \left(\frac{1}{\tau} - i\omega\right)\frac{R_2}{v_f} = x - iy,$$

$$\alpha_0 = \arccos\left(\sqrt{1-\frac{K^2}{\xi^2}}\right),\ \psi = (\xi\cos\alpha - \sqrt{K^2 - \xi^2\sin^2\alpha}),$$

$$\eta = (\xi\cos\alpha + \sqrt{1-\xi^2\sin^2\alpha}).$$

For $K \longrightarrow 0$ (or $\alpha_0 \longrightarrow 0$), Eq. (5) yields

$$\sigma = \sigma_0 F(x,y) = \sigma_0\mathrm{Re}\left\{2y^2\int_0^1 \xi^3 d\xi \times \int_0^1\int_0^{\pi} \frac{\rho^3}{\sqrt{1-\rho^2}}\frac{(1-\exp(-z\eta/\rho))}{z}\sin^2\alpha d\rho d\alpha\right\}. \qquad (9)$$

This expression coincides with the result obtained previously [7] for a cylindrical elongated homogeneous metal particle.

Figures 1 and 2 show the results of numerical calculation of the dimensionless absorption cross section

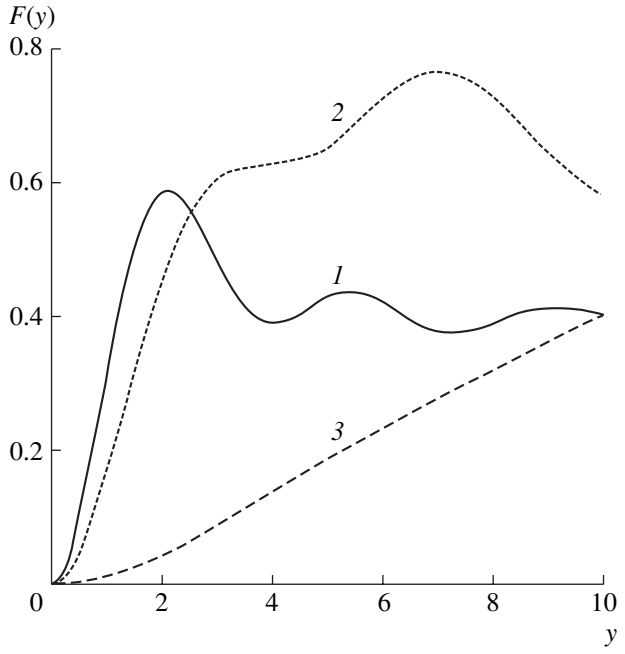

Fig. 1. Dimensionless absorption cross section F versus the dimensionless frequency y for $x = 0$ and $K = 0.3$ (*1*), 0.71 (*2*), and 0.95 (*3*).

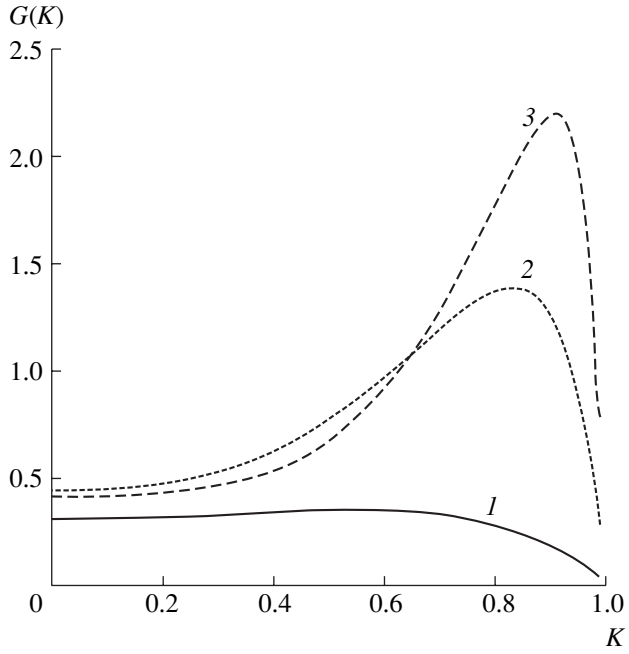

Fig. 2. Specific dimensionless absorption cross section G versus the ratio K of the core radius to the particle radius for $x = 0$ and $y = 0.3$ (*1*), 0.71 (*2*), and 0.95 (*3*).

$F(x, y, K)$ for an elongated cylindrical inhomogeneous particle.

Discussion of results. The dimensionless absorption cross section F depicted in Fig. 1 as a function of the dimensionless frequency y refers to the free electron case, whereby the inverse mean free path x of electrons in the metal shell is very small ($x = 0$). The calculations were performed for various ratios K of the core radius to the particle radius. An analysis of these curves shows that a special feature in the behavior of the dimensionless absorption cross section is a phase shift observed for the curves corresponding to different K and smoothening of the oscillations of the frequency dependence with increasing K (and the resulting decrease in the metal volume fraction). At high frequencies of the external field ($y \gg 1$), the main contribution to the absorption is due to electrons occurring in the narrow (with a thickness of $1 \sim v_f/\omega$) metal regions near the reflecting cylindrical surfaces inside the particle. For this reason, the absorption cross section at high frequencies increases with the K value despite the decrease in the metal volume fraction. This is explained by a more rapid increase in the area from which electrons are scattered and, hence, in the effective volume of absorbing layer. The maximum of the dimensionless absorption cross section at small x ($x \ll 1$) corresponds to the case when the time of flight for electrons between the two reflecting surfaces is close to the period of the external electromagnetic field.

For analysis of the dependence of the dimensionless absorption cross section on the ratio K of the core radius to the particles radius, it is convenient to use Fig. 2, showing variation of the G value representing the cross section per unit metal volume in a particle:

$$G(K) = \frac{F(K)}{1 - K^2}.$$

As can be seen, this specific absorption cross section exhibits unusual behavior in the case of cylindrical particles with a pure metal shell (were electrons possess a large mean free path) and in the case of very small cylindrical particles obeying the condition $x \ll 1$. In such particles, the specific absorption cross section in a broad range of K can increase even for decreasing field frequency. As the x value grows, the specific absorption cross section becomes a monotonically increasing function of the field frequency (the strength of the induced eddy electric field is proportional to the frequency of the external electromagnetic field). For $K \sim 1$, the specific absorption cross section is small in the entire frequency range because the cylindrical metal shell is very thin and electrons (moving between the two boundaries of this shell) cannot be significantly accelerated by the external field (and the current density in the shell tends to zero).

REFERENCES

1. Yu. I. Petrov, *Physics of Small Particles* (Nauka, Moscow, 1984), Chap. 7 [in Russian].

2. J. M. Ziman, *Electrons and Phonons* (Clarendon Press, Oxford, 1960; Inostrannaya Literatura, Moscow, 1962), Chap. 11.
3. A. G. Lesskis, V. E. Pasternak, and A. A. Yushkanov, Zh. Éksp. Teor. Fiz. **83**, 310 (1982) [Sov. Phys. JETP **56**, 170 (1982)].
4. A. G. Lesskis, A. A. Yushkanov, and Yu. I. Yalamov, Poverkhnost, No. 11, 115 (1987).
5. P. M. Tomchuk and B. P. Tomchuk, Zh. Éksp. Teor. Fiz. **112**, 661 (1997) [JETP **85**, 360 (1997)].
6. É. V. Zavitaev, A. A. Yushkanov, and Yu. I. Yalamov, Zh. Tekh. Fiz. **71** (11), 114 (2001) [Tech. Phys. **46**, 1460 (2001)].
7. É. V. Zavitaev, A. A. Yushkanov, and Yu. I. Yalamov, Opt. Spektrosk. **92**, 851 (2002) [Opt. Spectrosc. **92**, 784 (2002)].
8. É. V. Zavitaev, A. A. Yushkanov, and Yu. I. Yalamov, Zh. Tekh. Fiz. **73** (3), 16 (2003) [Tech. Phys. **48**, 290 (2003)].
9. É. V. Zavitaev, A. A. Yushkanov, and Yu. I. Yalamov, Zh. Éksp. Teor. Fiz. **124**, 1112 (2003) [JETP **97**, 996 (2003)].
10. R. D. Averitt, S. L. Westcott, and N. J. J. Halas, J. Opt. Soc. Am. B **16**, 1824 (1999).
11. A. Henglein, J. Phys. Chem. B **104**, 2201 (2000).
12. L. D. Landau and E. M. Lifshitz, *Course of Theoretical Physics*, Vol. 8: *Electrodynamics of Continuous Media* (Nauka, Moscow, 1992; Pergamon Press, New York, 1984).
13. W. A. Harrison, *Solid State Theory* (McGraw-Hill, New York, 1970; Mir, Moscow, 1972).
14. R. Courant and D. Hilbert, *Methods of Mathematical Physics*, Vol. 2: *Partial Differential Equations* (Interscience, New York, 1962; Mir, Moscow, 1964), Part 2.

Translated by P. Pozdeev

Technical Physics Letters, Vol. 30, No. 8, 2004, pp. 701–704. Translated from Pis'ma v Zhurnal Tekhnicheskoĭ Fiziki, Vol. 30, No. 16, 2004, pp. 82–89.

Fine Structure of "White" Optical Vortices in Crystals

A. V. Volyar, Yu. A. Egorov, A. F. Rubass, and T. A. Fadeeva

Taurida National University, Simferopol, Ukraine

Received December 25, 2004

Abstract—Representation of a perturbed optical vortex past a uniaxial crystal and a polarization filter on the complex plane and the orbital Poincaré sphere was experimentally and theoretically studied. It is shown that the main properties of a polychromatic optical vortex are adequately described using eight experimentally measured quantities, including four orbital and four spin Stokes parameters of a singular beam. © *2004 MAIK "Nauka/Interperiodica".*

The possibility of generating optical vortices in a polychromatic light ("white" vortices) was originally suggested by Berry and Klein [1], who succeeded in reproducing the fine structure of a wave caustic by means of white light scattering in a corrugated glass. The fine structure was obtained by a regular "package" of individual vortices, which eventually form an analogue of the crystal lattice [2]. The vicinity of each vortex at the sites of this lattice exhibited specific coloration significantly different from the rainbow pattern. Nevertheless, this method principally did not allow the formation of individual white vortices. Leach and Padgett [3] suggested a new method of obtaining white vortices using conventional computer synthesized holograms. According to this approach, the beam dispersion past the hologram is corrected using a special prism compensating for the angular dispersion of the hologram.

Recently [4], we analyzed the main properties of single white vortices arising in a beam passed through a uniaxial crystal and a polarization filter. Our method is simple, convenient, and allows the position of a vortex in the beam to be controlled. However, white vortices generated by this method exhibit a characteristic fine structure different from the structure of monochromatic vortices. This is related to the fact that a degenerate vortex, appearing at the crystal axis in the absence of external polarization perturbation, splits into two single vortices under the action of an external perturbation. The contours of such vortices smear with increasing distance from the axis and eventually the vortices disappear. It was shown [4] that this process is caused by depolarization of the beam. At the same time, perturbed white vortices acquire new properties. Experiments show that the vicinity of a perturbed vortex exhibits a surprisingly weak coloration sharply different from that in the minima of diffraction patterns. However, prior to studying the distribution of colors at the vortex core, it is necessary to outline the set of parameters which allow the state of polychromatic vortices to be consistently described.

This study was aimed at finding and characterizing the main parameters responsible for the state of white vortices in the beam past a uniaxial crystal.

Let a circularly polarized polychromatic light beam pass sequentially through a uniaxial crystal and a quarter-wave plate (phase corrector) with a deviation of μ from the standard phase difference ($\pi/2$), so that $\Delta = \pi/2 + \mu$. (It was noted previously [4] that the effect of a $\lambda/4$ plate on a polychromatic light beam is accompanied by transformation of the polarization state for the spectral components near the spectral maximum, and the other components introduce a depolarized background. In addition, it is possible to use the achromatic Fresnel rhomb as an analog of the $\lambda/4$ plate.) The electric field components can be determined using the formulas [5, Eq. (2)]

$$\begin{aligned} E_x &= \{-\sin\mu/2\cos\delta/2 + i\cos\mu/2\sin\delta/2\exp(i2\varphi)\}G_0, \\ E_y &= i\{\cos\mu/2\cos\delta/2 + i\sin\mu/2\sin\delta/2\exp(i2\varphi)\}G_0, \end{aligned} \quad (1)$$

where $\delta = ar^2$, a is the crystal lattice constant, Δ is the phase difference introduced by the polarization perturbation of the $\lambda/4$ plate, $G_0 = \exp\{-ikr^2/2Z\}/Z$ is the wave function of the fundamental Gaussian beam, and $Z = z + iz_0$, $z_0 = k\rho^2/2$, ρ is the beam waist radius at $z = 0$. The initial beam is assumed to be left-polarized. In the vicinity of the vortex core, the beam field components E_x can be represented in the following form:

$$E_x' = (Ax' + iBy')G_0(x', y'), \quad (2)$$

where $A = \sqrt{a\mu}$ and $B = \sqrt{a}\sin\mu/\sqrt{\mu}$. Consider the column vector

$$\mathcal{J} = \begin{pmatrix} \mathcal{J}_x \\ \mathcal{J}_y \end{pmatrix} = \begin{pmatrix} A \\ iB \end{pmatrix}, \quad (3)$$

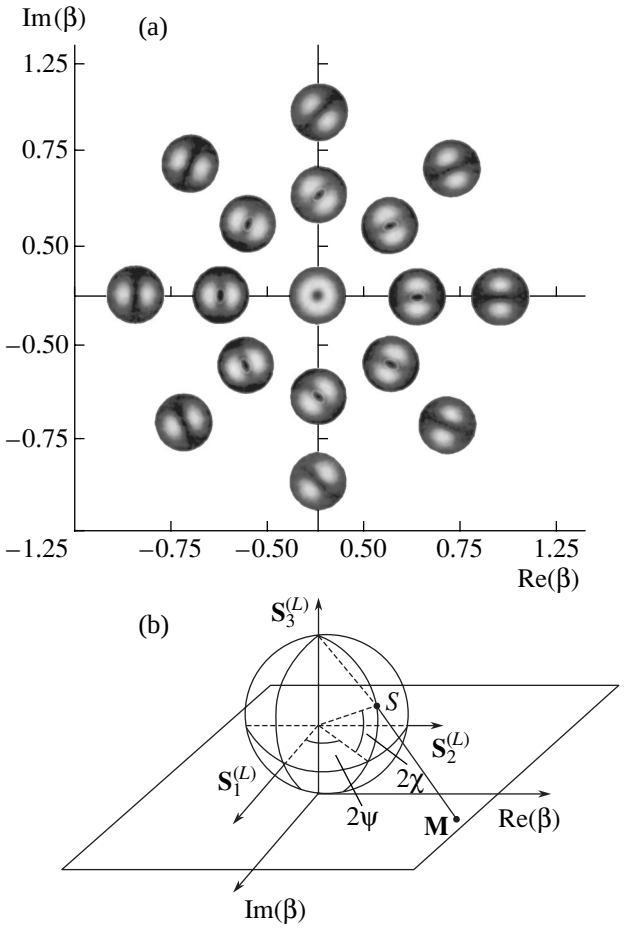

Fig. 1. Representation of the state of an optical vortex on (a) the complex plane and (b) the orbital Poincaré sphere.

which resembles the Jones vector, well known in polarization optics [6]. Let us select a new basis set for components of the $\mathcal{J}$ vector using the transformations

$$\mathcal{J}^+ = \mathcal{J}_x + i\mathcal{J}_y = A - B, \quad \mathcal{J}^- = \mathcal{J}_x - i\mathcal{J}_y = A + B. \quad (4)$$

In the general case, the parameters A and B are complex quantities (as, e.g., in the case of a Gaussian beam diffraction on a wedge [7]). For this reason, it is convenient to form a united complex parameter β,

$$\beta = \mathcal{J}^+/\mathcal{J}^- = |\beta|\exp(i\Omega), \quad (5)$$

where $\Omega = \arg(\beta)$. Now, the state of the field in the vicinity of the core of a monochromatic vortex can be represented by a point on the complex plane with the real (Re(β)) and imaginary (Im(β)) axes. Note that lines of equal intensity at the vortex core have an elliptical shape (see formula (2)). A change in the vortex parameters modifies the shape of this ellipse. Evolution of the shape of a perturbed vortex is represented by a trajectory of the point on the complex plane (Fig. 1a). Moving along the straight rays outgoing from the origin of coordinates on the complex plane, we can trace the change in the vortex ellipticity for a constant slope of the major semiaxis. The motion along the circle centered at the origin corresponds to a constant ellipticity. The slope of the semimajor axis changes by π upon complete tracing of the contour.

In order to provide for a general description of the state of the vortex core, we use the properties of stereographic projection and map the points of the complex plane $\beta^{(+,-)}$ on a sphere tangent to the plane at the origin (Fig. 1b). In polarization optics, this sphere is called the Poincaré sphere and the Cartesian coordinates on the sphere are called the Stokes parameters. These parameters will be referred to as the orbital vortex parameters $\{S_0^L, S_1^L, S_2^L, \text{and } S_3^L\}$ (the term will be explained below) to be distinguished from the polarization (or spin) Stokes parameters. In terms of column vector (3), the orbital vortex parameters can be written as

$$S_0^L = |\mathcal{J}_x|^2 + |\mathcal{J}_y|^2 = A^2 + B^2 = \frac{a}{\mu}(\mu^2 + \sin^2\mu),$$

$$S_1^L = |\mathcal{J}_x|^2 - |\mathcal{J}_y|^2 = A^2 - B^2 = \frac{a}{\mu}(\mu^2 - \sin^2\mu), \quad (6)$$

$$S_2^L = 2\mathrm{Re}(\mathcal{J}_x\mathcal{J}_y^*) = 0, \quad S_3^L = 2\mathrm{Im}(\mathcal{J}_x^*\mathcal{J}_y) = 2a\sin\mu.$$

Thus, the poles of the sphere correspond to ideal optical vortices with different signs of the ellipticity, while the equator corresponds to completely distorted vortices—the states of degenerate edge dislocations (superpositions of two vortices with opposite topological charges). In our case, the perturbation μ shifts the vortex states along the meridian crossing the S_1^L axis. The vortex ellipticity Q and the angle of the major semiaxis ψ are determined from the formulas

$$L = \frac{S_3^L}{S_0^L} = \sin 2\chi, \quad Q = \tan\chi, \quad \frac{S_2^L}{S_1^L} = \tan 2\psi. \quad (7)$$

Let a polychromatic beam propagate through the crystal. For the sake of simplicity, the spectral function of the beam is assumed to be as follows [4]:

$$U = \exp(-(k - \tilde{k})^2/\Delta k^2). \quad (8)$$

The orbital parameters of this polychromatic beam are

$$\tilde{S}_0 = \int_{-\infty}^{\infty} S_0(k)U(k,\Delta k)dk = \alpha\{\gamma^2(\tilde{k}^2 + \Delta k^2/2) + [1 - \exp(-\gamma^2\Delta k^2)\cos(2\tilde{k}\gamma)]/2\}/\gamma,$$

$$\tilde{S}_1 = \int_{-\infty}^{\infty} S_1(k)U(k,\Delta k)dk = \alpha\{\gamma^2(\tilde{k}^2 + \Delta k^2/2) - [1 - \exp(-\gamma^2\Delta k^2)\cos(2\tilde{k}\gamma)]/2\}/\gamma, \quad (9)$$

$$\tilde{S}_3 = \int_{-\infty}^{\infty} S_3(k)U(k,\Delta k)dk = 2\alpha\{\tilde{k}\sin(\tilde{k}\gamma) + \Delta k^2\gamma\cos(\tilde{k}\gamma)/2\},$$

where $\gamma = \Delta n_2 d$; $\alpha = \Delta n_1/h$ [4]; $\tilde{k}$ is the wave number at the spectral maximum; Δn_1 and Δn_2 are the birefringences of the uniaxial crystal and the λ/4 plate, respectively; and h is the crystal thickness. Using expression (7), the ellipticity of the vortex core is set as

$$L = \sin 2\chi = \tilde{S}_3^L,$$

$$\tilde{Q} = \frac{\tilde{b}}{\tilde{a}} = \tan\chi = \tan\{\arcsin(L)/2\} = L/(1 + \sqrt{1 - L^2}),$$

$$-\frac{\pi}{2} \le \chi \le \frac{\pi}{2},$$

where $\tilde{b}$ and $\tilde{a}$ are the axes of the ellipse formed by the line of the equal intensity level. These values can be determined experimentally.

In order to elucidate the physical meaning of the orbital vortex parameters, let us determine the average value of the operator of orbital momentum $\hat{L} = -i\partial/\partial\varphi$ [8]:

$$\langle L\rangle = \frac{\langle E_x|\hat{L}|E_x\rangle}{\langle E_x|E_x\rangle} = \frac{2AB}{A^2 + B^2} = \frac{S_3^L}{S_0^L}. \quad (10)$$

As can be seen, the third parameter determines the orbital angular momentum L of a perturbed vortex, by analogy with the third Stokes parameter S_3 determining the spin angular moment of the field. This result indicates that the northern hemisphere of the orbital Poincaré sphere (Fig. 1) corresponds to the vortices with positive orbital angular momenta, while the southern hemisphere represents the states with negative momenta.

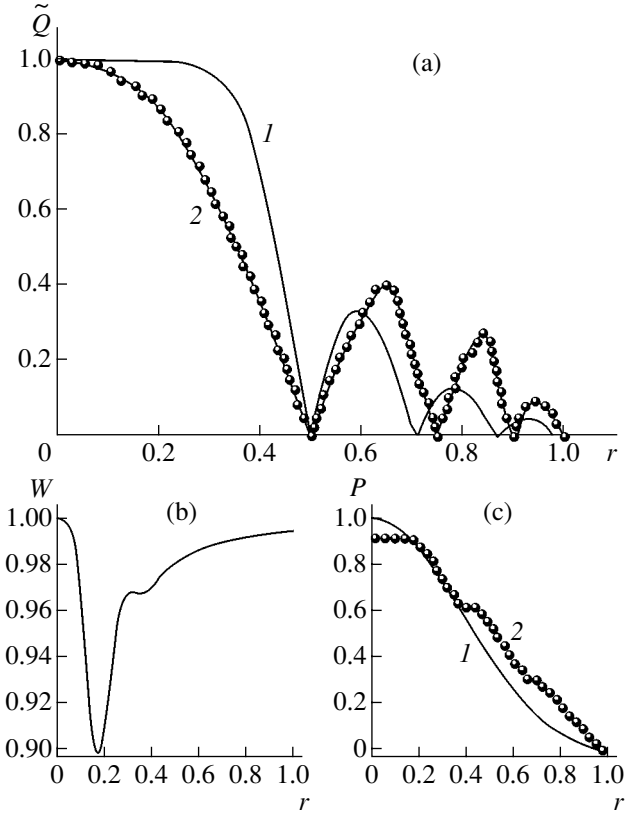

Fig. 2. Plots of the (a) ellipticity Q of the perturbed vortex core, (b) probability W of encountering a vortex in the state with the ellipticity Q, and (c) the degree of polarization P versus radial displacement r (rel. units): (*1*) theory; (*2*) experiment.

For the experimental investigation, a coherent light beam from an incandescent lamp was passed through a $LiNbO_3$ crystal, λ/4 plate, and a polarization filter [4]. The slope of the λ/4 plate was varied, thus introducing a polarization perturbation and splitting the degenerate vortex at the axis. The beam image was monitored by a CCD camera and processed on a computer. Using these data, lines of equal intensity in the vicinity of the vortex were constructed and the ellipse semiaxes $\tilde{a}$ and $\tilde{b}$ were determined. The results of these measurements presented in Fig. 2a show a good agreement between theoretical and experimental curves of the ellipticity Q versus radial displacement r. It should be noted that complete description of the state of a polychromatic vortex can be provided in terms of the quantity $W = (S_1^{L^2} + S_2^{L^2} + S_3^{L^2})^{1/2}/S_0^L$ characterizing the probability to encountering an optical vortex in the state with ellipticity Q. Figure 2b shows a theoretical plot of the probability W versus r. As the distance from the beam axis increases, the degree of polarization in the beam past the crystal exponentially decays to zero. In the experiment, this is manifested by iridescence of the singularities. Since the results of theoretical calculations of the

polarization P (corresponding to the measurement of four spin Stokes parameters) were reported elsewhere [4], we only present here the experimental plot of $P(r)$ (Fig. 2c).

In conclusion, the results of our investigation showed that exhaustive description of the state of a polychromatic singular beam requires using eight experimentally measured quantities, including four orbital and four spin Stokes parameters. Evolution of a singular beam is conveniently represented by a trajectory constructed either on the complex plane or on the orbital Poincaré sphere.

REFERENCES

1. M. Berry and S. Klein, Proc. Natl. Acad. Sci. USA, Phys. **93**, 2614 (1996).
2. M. Berry, J. Nye, and F. Whright, Philos. Trans. R. Soc. London, Ser. A **291**, 453 (1979).
3. J. Leach and M. J. Padgett, New J. Phys. **5**, 154.1 (2003).
4. A. V. Volyar and T. A. Fadeeva, Opt. Spektrosk. **94**, 260 (2003) [Opt. Spectrosc. **94**, 235 (2003)].
5. A. V. Volyar and T. A. Fadeeva, Opt. Spektrosk. **95**, 846 (2003) [Opt. Spectrosc. **95**, 792 (2003)].
6. R. M. Azzam and N. M. Bashara, *Ellipsometry and Polarized Light* (North-Holland, Amsterdam, 1977; Mir, Moscow, 1981).
7. A. V. Volyar, T. A. Fadeeva, and V. G. Shvedov, Opt. Spektrosk. **93**, 286 (2002) [Opt. Spectrosc. **93**, 267 (2002)].
8. L. Allen, M. J. Padjett, and M. Babiker, Prog. Opt. **39**, 291 (1999).

Translated by P. Pozdeev

Technical Physics Letters, Vol. 30, No. 8, 2004, pp. 705–707. Translated from Pis'ma v Zhurnal Tekhnicheskoĭ Fiziki, Vol. 30, No. 16, 2004, pp. 90–94.

Scattering of Acoustic Waves from Inhomogeneities of the Velocity Field of a Moving Medium

N. N. Rozanov* and G. B. Sochilin

Institute of Laser Physics, St. Petersburg, Russia

** e-mail: rosanov@ilph.spb.su*

Received February 5, 2004

Abstract—It is demonstrated that acoustic waves propagating in a moving liquid can be scattered on inhomogeneities of the velocity field of the medium, and a theory of such scattering is developed. The obtained estimates show the possibility of acoustic diagnostics of the velocity field inhomogeneities in moving media. *© 2004 MAIK "Nauka/Interperiodica".*

The velocity of propagation of waves of different types in a moving medium depends not only on the characteristics of the medium as such (e.g., on the index of refraction) but also on the velocity of motion of this medium. In the case of electromagnetic waves, this is manifested by partial light entrainment according to the relativistic Fresnel–Fizeau effect [1]. Acoustic waves, which propagate at velocities significantly lower than the speed of light, also exhibit a similar effect with complete entrainment [2]. Previously, this phenomenon was studied predominantly in the case of a homogeneous velocity field of a moving medium. However, inhomogeneities in the velocity field may give rise to new interesting effects. Recently, we demonstrated for optical [3] and acoustic [4] waves (see also [5]) that optical and acoustic nonreciprocal waveguides and lenses (with different signs of focal distances for the counterpropagating acoustic waves) can be formed in moving media featuring a transverse (with respect to the main wave propagation direction) variations of the velocity of motion, for example, in tubes with flowing water.

Recently [6], we reported on another related optical effect: the relativistic diffraction (scattering) of electromagnetic radiation on inhomogeneities of the velocity of a dielectric medium. This paper is aimed at an analysis of the acoustic analogue of this phenomenon. We propose a theory describing the scattering of acoustic waves on spatial inhomogeneities of the hydrodynamic velocity field of a medium. We believe that, based on this analysis, the possibility of acoustic monitoring of the velocity of a medium "in a pure form" (i.e., when the motion of a medium is not accompanied by significant changes in its temperature, density, or other acoustic characteristics) can be of interest in various practical applications.

The initial set of equations describing the motion of a medium represents the equations of continuity and the Euler equations [2, 7]

$$\frac{\partial \rho}{\partial t} + \mathrm{div}\rho\mathbf{v} = 0, \quad \frac{\partial \mathbf{v}}{\partial t} + (\mathbf{v}\nabla)\mathbf{v} = -\frac{\nabla p}{p}, \qquad (1)$$

where ρ, $\mathbf{v}$, and p are the liquid density, velocity, and pressure, respectively. Let us separate the motion of the medium into a "hydrodynamic" component (in the absence of acoustic waves, indicated by subscript "0") and acoustic component (primed values) and assume the sound amplitude to be small: $\rho = \rho_0 + \rho'$; $p = p_0 + p'$; $\mathbf{v} = \mathbf{v}_0 + \mathbf{v}'$, and $\mathbf{v}_0 \ll c_s$, where $c_s = \sqrt{(\partial\rho/\partial\rho_0)_s}$ is the sound velocity in the immobile medium; ρ_0 and p_0 are constants depending neither on the time t nor on the spatial coordinates $\mathbf{r}$. Linearizing of Eqs. (1) with respect to the primed quantities, we obtain $p' = c_s^2\rho'$ and

$$\begin{aligned} \frac{\partial \mathbf{v}'}{\partial t} + \frac{\Delta p'}{\rho_0} &= -(\mathbf{v}_0\nabla)\mathbf{v}' - (\mathbf{v}'\nabla)\mathbf{v}_0, \\ \frac{\partial p'}{\partial t} + \rho_0 c_s^2 \mathrm{div}\mathbf{v}' &= -\mathrm{div}p'\mathbf{v}_0. \end{aligned} \qquad (2)$$

This closed problem can be solved using perturbation theory for a small hydrodynamic velocity $\mathbf{v}_0$ by setting $p' = p_0' + p_1'$; $\mathbf{v}' = \mathbf{v}_0' + \mathbf{v}_1'$. Here, the zero order corresponds to $\mathbf{v}_0 = 0$ and the usual acoustic equations [2, 7]. In the first-order approximation, we have

$$\begin{aligned} \Delta p_1' - \frac{1}{c_s^2}\frac{\partial^2 p_1'}{\partial t^2} &= -f, \\ f &= \rho_0 \mathrm{div}\{(\mathbf{v}_0'\cdot\nabla)\mathbf{v}_0' + (\mathbf{v}_0'\cdot\nabla)\mathbf{v}_0 + \mathbf{v}_0\mathrm{div}\mathbf{v}_0'\}. \end{aligned} \qquad (3)$$

The solution can be obtained in the form of a retarded potential [8]. Assuming that the inhomogeneity of the

velocity field is localized in a certain spatial region, we obtain for the far wave zone

$$p_1'(\mathbf{R}_0, t) = \frac{1}{c_s R_0}\iiint d\mathbf{r} f\left(t - \frac{R_0 - \left(\frac{\mathbf{R}_0 \cdot \mathbf{r}}{R_0}\right)}{c_s}\right). \quad (4)$$

According to this solution, the scattered acoustic wave in the general case is nonmonochromatic (even for a monochromatic incident wave). The monochromaticity can be retained if the velocity $\mathbf{v}_0$ of the hydrodynamic motion is stationary at all points ($\partial\mathbf{v}_0/\partial t = 0$).

Let a stationary hydrodynamic motion occur in a finite region of liquid with the volume V representing a body of revolution with a symmetry axis coinciding with the axis of rotation. Consider a plane monochromatic longitudinal acoustic wave representing a solution of Eq. (3) incident on this region with the velocity distribution $\mathbf{v}_0' = \mathbf{m}A\exp(ik(\mathbf{m} \cdot \mathbf{r}) - i\omega t)$, where $\mathbf{m}$ is the unit vector of the wave propagation direction, A is the amplitude, $k = 2\pi/\Lambda$ is the wave number, and Λ is the wavelength. Let us calculate the scattering of this wave on the velocity field inhomogeneity $\mathbf{v}_0(\mathbf{r})$ of the type

$$\mathbf{v}_0(\mathbf{r}) = \mathbf{u}(\mathbf{r})\Phi(\mathbf{r}), \quad \Phi(\mathbf{r}) = \begin{cases} 1 & \mathbf{r} \in V, \\ 0 & \mathbf{r} \notin V, \end{cases} \quad (5)$$

where $\mathbf{u} = [\mathbf{\Omega} \cdot \mathbf{r}]$, and $\mathbf{\Omega}$ is the angular rotation velocity. Substituting relations (5) into expression (4), we obtain

$$p_1' = \frac{\rho_0 \Omega A \exp(-i\omega t + ikR_0)}{4\pi R_0}\iiint d\mathbf{r} e^{-ik(\mathbf{r} \cdot (\mathbf{n} - \mathbf{m}))}$$

$$\times\left\{(m_1 x_2 - m_2 x_1)(2\Phi(\mathbf{r})k^2 - 2ik(\mathbf{m}, \mathrm{grad}\Phi))\right.$$

$$+\left(m_1\frac{\partial\Phi}{\partial x_2} - m_2\frac{\partial\Phi}{\partial x_1}\right) + ik\left(x_1\frac{\partial\Phi}{\partial x_2} - x_2\frac{\partial\Phi}{\partial x_1}\right) \quad (6)$$

$$\left.-\left(x_1(\mathbf{m} \cdot \nabla)\frac{\partial\Phi}{\partial x_2} - x_2(\mathbf{m} \cdot \nabla)\frac{\partial\Phi}{\partial x_1}\right)\right\},$$

where $\mathbf{n}$ is the unit vector of the direction to the point of detection. Selecting a cylindrical coordinate system such that $\mathbf{\Omega} = (0, 0, \Omega)$, $\mathbf{r} = (x_1, x_2, x_\Omega)$, $\varsigma = \sqrt{x_1^2 + x_2^2}$, and $\varphi = \arctan\frac{x_1}{x_2}$. Taking into account that $\Phi(\mathbf{r})$ is independent of the angle φ, so that $\Phi(\mathbf{r}) = \Phi(\varsigma, x_\Omega)$, we obtain

$$p_1' = \frac{\rho_0 \Omega A \exp(-i\omega t + ikR_0)}{2\pi R_0} m_{\perp\Omega}$$

$$\times\iiint d\mathbf{r} e^{-ik(\mathbf{r} \cdot (\mathbf{n} - \mathbf{m}))}\varsigma\sin(\varphi - \varphi_m) \quad (7)$$

$$\times\left(\Phi k^2 - ik\left(m_{\perp\Omega}\cos(\varphi - \varphi_m)\frac{\partial\Phi}{\partial\varsigma} + m_\Omega\frac{\partial\Phi}{\partial x_\Omega}\right)\right),$$

where

$$(\mathbf{r} \cdot (\mathbf{n} - \mathbf{m}))$$

$$= \varsigma[n_{\perp\Omega}\cos(\varphi - \varphi_n) - m_{\perp\Omega}\cos(\varphi - \varphi_m)] + x_\Omega(n_\Omega - m_\Omega),$$

and $n_{\perp\Omega}$ and $m_{\perp\Omega}$ are the projections of the corresponding vectors onto the plane (x_1, x_2). The integration is performed over the region of hydrodynamic velocity inhomogeneity characterized by the longitudinal size l and the longitudinal cross section profile $a(x_\Omega)$.

For the region of inhomogeneity having the shape of a round cylinder, the integrals can be expressed through cylindrical functions [6]. For the region of an arbitrary shape, the calculation simplifies if its dimensions are shorter than the wavelength Λ. Assuming also that $ka(x_\Omega)$, $kl \ll 1$, we obtain

$$p_1' = -ik^3\frac{\rho_0 \Omega A \exp(-i\omega t + ikR_0)}{2R_0} m_{\perp\Omega} n_{\perp\Omega}\sin(\varphi_n - \varphi_m)$$
$$\times(m_\Omega n_\Omega + m_{\perp\Omega} n_{\perp\Omega}\cos(\varphi_n - \varphi_m))F_m, \quad (8)$$

where $F_m = \int_{-l}^{l} dx_\Omega (a(x_\Omega))^4$ is the form factor determined by the dimensions of the region of the hydrodynamic velocity inhomogeneity. For a cylindrical region, we have $F_m = 2la^4$; for a spherical region of radius l, $F_m = \frac{16}{15}l^5$. Formula (8) shows that the scattering is absent in the direction of wave incidence and in the opposite direction. If the directions of wave incidence and the axis of rotation are mutually perpendicular, we obtain (assuming that the wave propagation direction coincides with x_1 and $\varphi_m = 0$)

$$p_1' = ik^3\frac{\rho_0 \Omega A \exp(-i\omega t + ikR_0)}{4R_0}\Psi(\theta_n, \phi_n)F_m, \quad (9)$$

$$\Psi(\theta_n, \phi_n) = \sin^2\theta_n \sin 2\varphi_n.$$

The extrema $\Psi_{\max, \min} = \pm 1$ of the scattering amplitude $\Psi(\theta_n, \phi_n)$ are attained for $\theta_{\max, \min} = \pi/2$, $\phi_{\max} = \pi/4$ and $5\pi/4$, and $\phi_{\min} = 3\pi/4$ and $7\pi/4$ (two maxima and two minima).

The maximum pressure amplitude in the scattered wave is $|p'_{1\max}| = \frac{1}{4R_0}\rho_0\Omega k^3 F_m A$. For a plane acoustic wave, we have $p'_0 = Ac_s\rho_0$ [2]. For a spherical region, this yields

$$\eta = \frac{p'_1}{p'_0} = \frac{4}{15}k^3 l^3 \frac{l}{R_0}\frac{\Omega l}{c_s}. \quad (10)$$

For $\Omega = 2$ rev. s^{-1}, $\Lambda = 2$ m, $c_s = 1450$ m/s, $l = 0.5$ m, and $R_0 = 100$ m, we obtain $\eta = 3.6 \times 10^{-6}$. This result is evidence of the possibility of acoustic diagnostics of the hydrodynamic velocity inhomogeneities. The possibility of observing the scattering wave is also limited by the absorption and scattering of acoustic waves in the liquid, which significantly depend on the sound frequency.

REFERENCES

1. R. W. Wood, *Physical Optics* (Macmillan, New York, 1934; ONTI, Moscow, 1936).
2. L. D. Landau and E. M. Lifshitz, *Course of Theoretical Physics*, Vol. 6: *Fluid Mechanics* (Nauka, Moscow, 1986; Pergamon, New York, 1987).
3. N. N. Rozanov, G. B. Sochilin, and O. B. Danilov, Opt. Spektrosk. **95**, 908 (2003) [Opt. Spectrosc. **95**, 849 (2003)].
4. N. N. Rozanov and G. B. Sochilin, Pis'ma Zh. Tekh. Fiz. **30** (11), 85 (2004) [Tech. Phys. Lett. **30**, 483 (2004)].
5. A. Ya. Al'pin, in *Proceedings of the Jubilee Scientific–Engineering Conference of North-Western Division of Russian Academy of Engineering Sciences* (S-Peterb. Gos. Tekh. Univ., St. Petersburg, 2001), pp. 159–170.
6. N. N. Rozanov and G. B. Sochilin, Opt. Spektrosk. **94**, 624 (2003) [Opt. Spectrosc. **94**, 569 (2003)].
7. M. B. Vinogradova, O. V. Rudenko, and A. P. Sukhorukov, *The Theory of Waves* (Nauka, Moscow, 1979) [in Russian].
8. L. D. Landau and E. M. Lifshits, *The Classical Theory of Fields* (Nauka, Moscow, 1988; Pergamon Press, Oxford, 1975).

Translated by P. Pozdeev